Chair of Subsurface Engineering

Master's Thesis

Pore pressure influence on ultrasonic measurements simulated with Nitrogen in sandstones

Dominik Baumgartinger, BSc

February 2023

MONTANUNIVERSITÄT LEOBEN

www.unileoben.ac.at

AFFIDAVIT

I declare on oath that I wrote this thesis independently, did not use other than the specified sources and aids, and did not otherwise use any unauthorized aids.

I declare that I have read, understood, and complied with the guidelines of the senate of the Montanuniversität Leoben for “Good Scientific Practice”.

Furthermore, I declare that the electronic and printing version of the submitted thesis are identical, both, formally and with regard content.

Date 15 February 2023

Abstract

Gas storage in former oil or natural gas reservoirs is becoming more and more important, especially due to gas consumption fluctuations between summer and winter. In this context, injection and extraction processes occur. This raises the question of whether and to what extent these loadings or processes damage the reservoir rock.

In the present thesis, different sandstones were loaded with gas trying to induce damage and detect this damage with ultrasonic measurements. Under specific pressure conditions of 30 MPa vertical loading and 10 MPa circumferential loading, two experiments were performed. The test setup was built in a rock testing machine, where a piping system assures the gas flow as well as the regulation of the gas pressure which should simulate the pore pressure. For the first experiment, the gas pressure is increased by 10 bar every test. The second experiment should simulate the injection and extraction processes by cyclical loading with 10 and 90 bar (5 repetitions). Ultrasonic measurements are done before and after every test. The used samples are sandstones from the Trattnach oil field (1R,2R), Ruhr sandstone of the Imberg company (DBA1, DBA2), Buntsandstein (DBA5, DBA6) and sandstone from Groß Lessen of the Exxon Mobile company (4.1, 4.2).

Porosity measurements were performed before and after loading. These measurements show a clear decreasing trend. The Trattnach sandstone is an exception because it shows an increasing porosity, which can be explained by residual organic matter and severe mechanical damage to the sample. Through the ultrasonic measurements, travel times were measured and out of those p-wave velocities were calculated. These velocities decrease after loading in every sample, which clearly indicates that damage was done to the samples. By a Fourier transformation of the ultrasonic data, conclusions about damage or cracks can be made. The indicator here is the presence or absence of frequency components.

In conclusion, damage can be induced through loading the sample with certain gas pressures. Some loading stages show more difference than others. Ultrasonic measurements detect p-wave velocities, which provide information about the damage to the sample. Higher velocities indicate greater damage to the specimen. Porosity behaviour supports these observations and Fourier analysis provides a good complement. With this procedure it was not possible to quantify the damage in the sample.

Kurzfassung

Gasspeicherung in ehemaligen Öl- oder Erdgaslagerstätten gewinnt, vor allem aufgrund Gasverbrauchsschwankungen zwischen Sommer und Winter immer mehr an Bedeutung. Dabei treten Injektions- und Extraktionsvorgänge auf. Daraus ergibt sich die Frage, ob und inwiefern diese Belastungen beziehungsweise Vorgänge das Speichergestein beschädigen.

In der vorliegenden Arbeit wurde an unterschiedlichen Sandsteinproben versucht, Schaden zu induzieren und diesen mit Hilfe von Ultraschallmessungen zu detektieren. Zwei unterschiedliche Experimente wurden unter bestimmten Druckbedingungen durchgeführt. Die vertikale Belastung von 30 MPa wurde durch eine Gesteinspresse aufgebracht, während die Umfangsbelastung von 10 MPa durch eine Hoek Zelle erfolgte. Über ein Leitungssystem wird der Gasfluss sowie auch die Regelbarkeit des Gasdruckes, welcher den Porendruck darstellen soll, sichergestellt. Für Experiment 1 wird ein stufenweiser Anstieg des Gasdrucks um jeweils 10 bar beginnend bei 0 und endend bei 90 bar durchgeführt. Experiment 2 soll die Injektions- und Extraktionsvorgänge mittels zyklischer Belastung von 10 bar und 90 bar (5 Wiederholungen) simulieren. Vor und nach jeder Messung wird eine Ultraschallmessung absolviert. Bei den verwendeten Proben handelt es sich um Sandstein aus dem Trattnach Ölfeld (1R, 2R), Ruhrsandstein der Firma Imberg (DBA1, DBA2), Buntsandstein (DBA5, DBA6) und Sandstein aus Groß Lessen der Firma Exxon Mobile (4.1, 4.2).

Vor und nach der Belastung sind Porositätsmessungen durchgeführt worden, welche einen deutlichen Trend zur Abnahme zeigen. Ausnahme hierbei ist der Trattnach Sandstein, welcher eine Porositätszunahme aufweist. Dies wird auf organische Restsubstanz und sehr starke mechanische Beschädigung der Probe zurückgeführt. Die anhand der Laufzeit berechneten P-Wellen Geschwindigkeiten nehmen nach der Belastung in allen Proben ab, wodurch eindeutig auf eine Beschädigung der Proben geschlossen werden kann. Durch eine Fourier Transformation der gemessenen Ultraschalldaten können Aussagen über Schäden bzw. Risse in der Gesteinsprobe getätigt werden. Das Vorhandensein bzw. Fehlen von Frequenzkomponenten ist hierbei der Indikator.

Daraus kann geschlossen werden, dass die Induktion von Schaden durch Gasdruck mit Hilfe von Ultraschallmessungen detektierbar ist. Einige Druckstufen zeigen mehr Unterschied zur vorherigen als andere. Durch Ultraschallmessungen werden P-Wellen Geschwindigkeiten erfasst, welche Informationen über die Beschädigung der Probe liefern. Dabei deuten höhere Geschwindigkeiten auf größeren Schaden in der Probe hin. Das Verhalten der Porosität unterstützt diese Beobachtungen und die Fourier Analyse bietet eine gute Ergänzung dazu. Eine Quantifikation der Ergebnisse war mit diesem Versuchsaufbau beziehungsweise Ablauf nicht möglich.

CONTENTS

1 Introduction

A variety of geomechanical issues as well as the understanding of some tectonic processes in the Earth's crust are based on one of the most important physical properties of rocks, cracks. The penetrability of the rock is increased and space is created for the passage of fluids and gases, resulting in a decrease in rock strength as well as rock quality in general (Borm *et al.*, 1997; Kilburn & Voight, 1998; Legarth *et al.*, 2005; Tsang *et al.*, 2008). The influence of induced microcrack damage on P- and S-waves as a function of confining pressure has been analysed in several studies (Birch, 1960; Kern, 1990). In Blake *et al.* (2013), a sharp decrease in S-wave velocity and an almost constant decrease in P-wave velocity was found based on the propagation of microcracks.

Many geological materials are elastically anisotropic due to foliations and/or lineations. Several elastic constants, such as stiffness, dynamic bulk modulus, dynamic Young's modulus and dynamic Poisson's ratios, are necessary to determine elastic waves (Podio-Lucioni, 1968). Velocity measurements in different directions at a certain confining pressure reveal this elastic anisotropy, which is due to the effects of pores and cracks and the grain orientation of the minerals. By increasing the confining pressure, the effect of pores and cracks should decrease (Lo *et al.*, 1986).

Nowadays, gas storage is becoming more and more important and former oil or natural gas reservoirs are and should be used for it. Natural gas, hydrogen and also CO_2 are stored in such oil and gas reservoirs. The storage of natural gas and hydrogen is intended to support the weather-dependent renewable energies in the energy transition and provide sufficient energy (Speight, 2019; Muhammed *et al.*, 2023). CO_2 storage is intended to reduce the release of CO_2 into the atmosphere (Godec *et al.*, 2011).

In gas storage, microcracks in the reservoir rock are an essential feature, as the storage properties are directly affected. Injection and extraction processes occur during the storage of gas. These can have an influence on the surrounding rock by forming just such microcracks.

The questions that follow are whether damage is induced by the injection of gas into a reservoir rock and, if so, whether it is measurable with ultrasonic measurements. The present thesis is concerned precisely with answering these two questions.

The scope of the study can be divided in three main tasks.

- First, it is necessary to develop an experimental setup that allows the gas to flow through the rock sample. An essential part of this system is a Hoek cell, ensuring the gas flow through the sample. This is achieved by applying a certain pressure which presses the membrane of the Hoek cell against the surface of the sample, thus preventing the gas from escaping.
- The next task is to determine an experimental procedure to achieve valuable data. Therefore, it is important to acquire a feeling for the test system and the behaviour of the rock specimens during pore pressure loading. To provide more parameters of the rock samples, some non-destructive experiments were performed before applying pore pressure. These tests provide density, porosity, and ultrasonic velocity data.
- The final task is to examine all the data received for correlations and identify possible trends.

After the completion of all the above-mentioned tasks, the experimental results can act as a foundation for further experiments.

2 Theoretical Background

2.1 Gas storage

Gas storage in depleted oil and gas reservoirs is becoming increasingly important, mainly because of existing reservoirs. These reservoirs are an important way of storing surplus natural gas during production periods and retrieving it in times of need. One problem here is the risk of natural leakage, which is why the reservoir requires regular maintenance (Speight, 2019).

Injecting CO_2 into depleted oil reservoirs that no longer support economic production allows the gas to be stored in the rock and transports the remaining oil to the surface. This technology is called CO_2 Enhanced Oil Recovery and can increase oil production and reduce CO_2 release to the atmosphere (Alvarado & Manrique, 2010). Challenges include uncertainty about long-term storage of CO_2 in rock, limited availability of CO_2 sources, and the high cost of CO_2 capture and injection (Godec *et al.*, 2011).

The transition from fossil fuels to renewable energies is already taking place. In this context, hydrogen is becoming the focus of attention, as it is available in abundance. The only problem at present is storage, which is necessary to compensate for fluctuations in supply and demand. Underground storage of hydrogen presents some challenges, such as H_2 embrittlement, sulfidation, or gas purity during mixing. A very important challenge is also the caprock integrity failure (Muhammed *et al.*, 2023).

The sealing rock can be any lithology that has a greater capillary inflow pressure than uplift pressure of the gas in the accumulation (Evans, 2007). However, if this pressure is exceeded only once, it results in gas leakage because the gas permeability is increased (Reitenbach *et al.*, 2015; Luboń & Tarkowski, 2020). Important parameters affecting gas permeability are porosity, permeability, interfacial tension, and capillary pressure.

To ensure the integrity of a rock layer, although a decrease in porosity and permeability occur, it is necessary for mineral precipitation to proceed faster than dissolution, However, the injection and extraction of the gas will be affected if the precipitation rate is low, as this will lead to an increase in porosity and permeability (Zivar *et al.*, 2021; Ugarte & Salehi, 2022). Because of the porosity change, the seal strength can either be compromised or improved (Reitenbach *et al.*, 2015).

Due to the very low density of H_2 and its high diffusivity (Aftab *et al.*, 2022; Keshavarz *et al.*, 2022), laboratory measurements regarding gas permeability with hydrogen are difficult, which is why nitrogen is very often used as an alternative. That is why in the present thesis nitrogen was used.

2.2 Pore pressure

Pore fluid pressure is important for rocks because variations contribute to a variation in elastic wave velocities with depth (Gretener, 1969). One example is dehydration reactions, which release water. This results in a decrease in effective pressure, which promotes the formation of cracks in the rock (Kern & Richter, 1979).The injection and extraction processes have an influence on the pore pressure. The changes in pore pressure during injection are higher than during extraction, indicating induced damage from injection (Kim & Hosseini, 2017). Figure 2-1 shows the connection between the change in P-wave velocity and volumetric strain in relation to pressure. A close relationship between crack closure and velocity increase can be justified by the good correlation of the two curves (Kern, 1990). Opening a crack changes the path the wave takes through the specimen, causing it to travel longer distances when the p-wave velocity is reduced and shorter distances when it is increased (O'Dowd, 2002). The generation of new cracks usually leads to a decrease in the p-wave velocity (Lockner *et al.*, 1977).

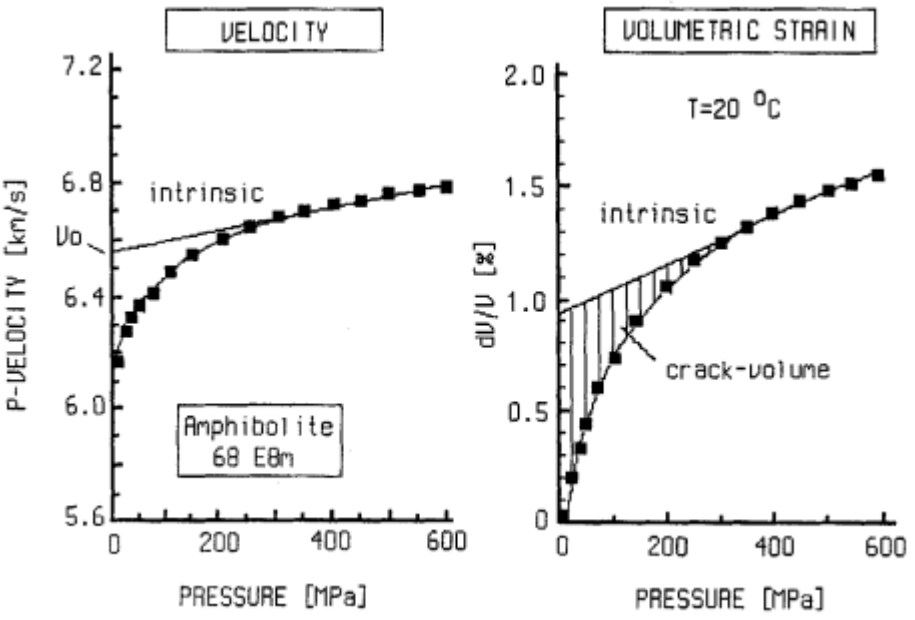

Figure 2-1: Relationship between pressure, elastic wave velocity, and the state of microfracturing depicted by velocity versus pressure and volumetric strain versus pressure curves (Kern, 1978; Kern & Schmidt, 1990).

2.3 Ultrasonic measurements

Ultrasonic measurements are a proven method for the determination of the elastic properties of a sample in the laboratory. Various problems can be tackled by determining the velocities of compressional (P) and shear (S) waves in rocks (Yurikov *et al.*, 2019). In some cases, many variants of ultrasonic sensors are used in an experiment to meet the requirements for measuring the elastic properties of rocks (Dewhurst & Siggins, 2006). To keep the number of sensors low, technical specialities of ultrasonic transducers are used. For example, by emitting S-waves, shear transducers trigger parasitic P-waves, which have much less energy than the S-waves (Wong *et al.*, 2008). The lower energy is due to the higher speed of the P-waves and an associated faster arrival at the receiving transducer. Because of this, it is possible to detect P- and S-wave velocities with one S-wave transducer pair (Lebedev *et al.*, 2013). The accuracy of the results obtained with the S-wave transducer pair is relatively close to the results obtained with conventional P-transducers (Yurikov *et al.*, 2019).

2.4 Fast Fourier-Transformation

The Fourier transform is a widely used and versatile tool in science, which is intended to modify a problem so that it can be solved more easily. It is used, for example, for modelling random processes, for boundary value problems, in quantum physics or in signal processing (Hoffman, 1997). A fast Fourier transform (FFT) is used to significantly reduce the complexity of discrete Fourier transforms (Lighthill, 1958).

The FFT is a fast implementation of the discrete Fourier transform (DFT) and can be used to compute the DFT in a time complexity rather than directly, making processing easier, especially for large data sets or real-time applications. In simple terms, the FFT performs a division of the input sequence into smaller and smaller subsequences, reducing the computations at each step (Cooley & Tukey, 1965).

An FFT is often represented as a spectrum of frequency components as shown in Figure 2-2. The frequency in Hertz is plotted on the x-axis and the amplitude of the respective frequency component is plotted on the y-axis. The amplitude indicates how strong the frequency component is present in the original data.

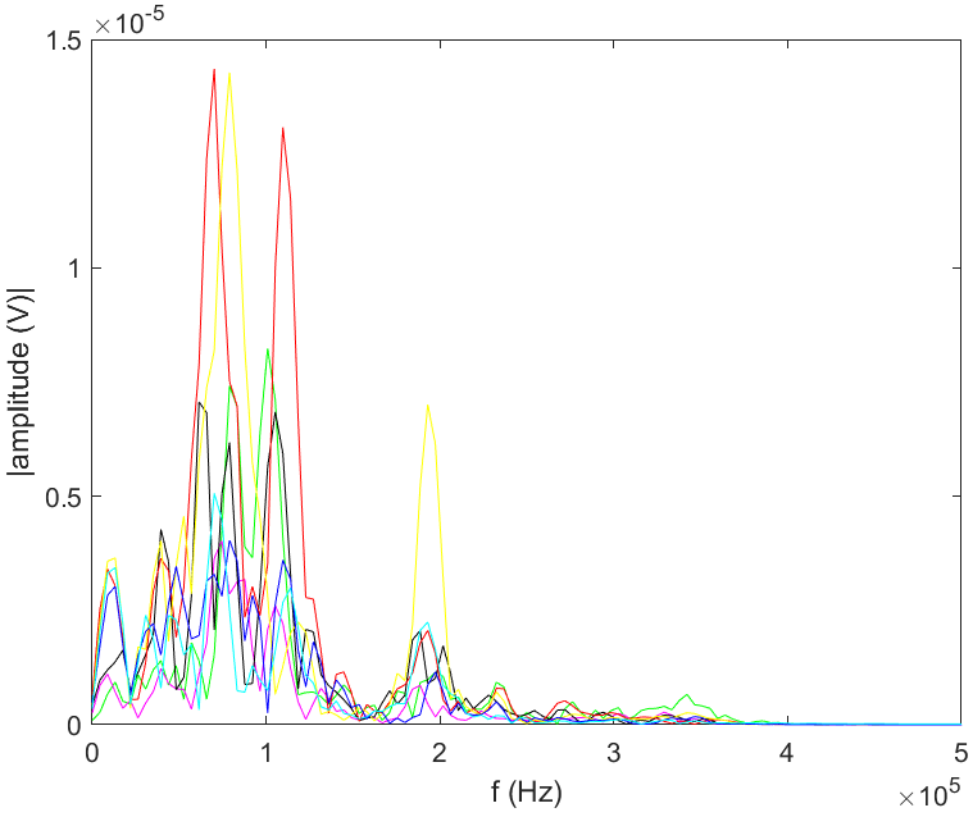

Figure 2-2: Example of the output of an FFT as a frequency spectrum. The frequency in Hertz is plotted on the x-axis and the amplitude in volts is plotted on the y-axis.

Detection of cracks or damage using Fourier Transform is done by analysing the frequency components of an ultrasonic signal sent through the material. The occurrence of damage changes the structure of the material and affects the sound waves sent through the substance (Singh *et al.*, 2017). This causes changes in the frequency components, which are detected by FFT. Shifts, the appearance of new or the disappearance of frequency components indicate damage (Melhem & Kim, 2003).

3 Geology

3.1 Sandstones as reservoir rocks

Sandstone is formed by consolidation of sand grains, which are transported by wind, rivers or waves and then deposited. The solidification of these grains takes places under pressure and by means of chemical processes, the sand grains are bonded together over time. Different colours or textures can be achieved by incorporating other minerals such as clay, lime, or iron oxides. Furthermore, the sandstone can be porous or rather dense, depending on the history of its formation.

According to Pettijohn *et al.* (1973), the classification of sandstones is into three main types: terrigenous, carbonate, and pyroclastic. Terrigenous sandstones, which are the most common, are formed by deposition of sediments, which consist largely of eroded rocks. Carbonate sandstones are formed mainly from the deposition of limestone or dolomite particles, which originate from dead organisms or chemical deposits. Pyroclastic sandstones are formed from volcanic material ejected by volcanic activity (Mcbride, 1963).

Sandstones serve as reservoirs for oil and gas, as well as for groundwater, as they have very good reservoir properties. Diagenetic processes near the surface and during burial determine the characteristics of sandstone reservoirs, as well as the textural and mineralogical composition and the depositional environment (Bjørlykke & Jahren, 2010). The essential properties affecting well productivity for a petroleum reservoir are porosity, rock permeability, total compressibility, lithology, and the thickness of the production zone (Guo, 2019).

Terrigenous sandstones tend to show the most promising characteristics for good reservoir quality, as they generally have higher porosity and permeability than carbonate and pyroclastic sandstones (Pettijohn *et al.*, 1973). In carbonate sandstones, these parameters can vary from low to moderate depending on whether dolomitic or calcareous sandstone is present (R. H. Dott, JR., 1964). Due to the high temperatures involved in the formation of pyroclastics, pores and voids in the rock are often closed, resulting in lower porosity and permeability (Mcbride, 1963).

3.2 Sample description

3.2.1 Trattnach sandstone

The Trattnach oil field is located in Upper Austria and Salzburg, where several oil and gas deposits are distributed. RAG Austria AG operates the oil production and the fossil fuels extracted are mainly used to generate electricity and heat (Gross *et al.*, 2015).

The Trattnach oil field is part of the Molasse Basin, which was formed during the Alpine orogeny in the Tertiary. The oil field itself consists of several layers of oil and gas bearing sandstones, mostly separated by layers of mudstone (Schmid, 2018). These sandstones were formed from fine sand that was transported to the sea during the deposition of rivers and streams in the Tertiary. Consolidation occurred due to gravity and the weight of the overlying rocks and porosity is the result of weathering, erosion, and sorting (Gross *et al.*, 2015).

Figure 3-1 shows the Trattnach samples used. A striking feature is the green colour, which indicates the presence of glauconite. In general, these samples are comparatively very soft and show a high porosity. The grain size can be described as fine-grained. Table 11-1 shows the dimensions of the specimens, while Table 5-1 shows the calculated porosities.

Figure 3-1: Trattnach sandstone samples 1R (left) and 2R (right).

3.2.2 Ruhr sandstone

The Ruhr sandstone is a geological formation that occurs mainly in the Ruhr area in North Rhine-Westphalia, Germany, and was formed in the Upper Carboniferous. It consists of sandstone formed by deposits of sand and mud in shallow marine basins and may also contain layers of clay and coal (Simper, 1991). Due to its hardness and resistance to weathering, Ruhr sandstone is well suited for use as an outdoor building stone. Geologically, the Ruhr sandstone is attributed to the Westphalian Cretaceous basin, which extends from Belgium to Poland, and form layers up to 300 meters thick (Dillmann, 2008). It is also known for fossils from the Carboniferous, such as plant remnants or remnants of marine life (Simper, 1991).

Figure 3-2 shows the Ruhr sandstone specimens used. The grain size can be described as medium to coarse grained. Due to the sedimentation stratification bands are clearly visible. The samples show a grey to grey-brown colour impression. Also, a slightly reddish coloration can be observed, indicating the presence of iron oxide. The dimensions and the calculated porosities are shown in Table 11-1 and Table 5-1.

Figure 3-2: Ruhr sandstone samples DBA1 (left) and DBA2 (right).

3.2.3 Buntsandstein

A permo-triassic sedimentary sequence of sandstones, but also claystones and siltstones, is called Buntsandstein, which occurs in large parts of Europe and is particularly widespread in Central Europe. In the upper Rhine Graben, the facies of the Buntsandstein shows a sequence of fluvial sandstones, siltstones, and mudstones. The formation of the sandstones and siltstones occurred by river deposition and flooding events, while the mudstones were deposited by calmer waters (Heap *et al.*, 2019). Pore distribution is an important petrophysical property of Buntsandstein, as it strongly controls the permeability of the rock. In general, Buntsandstein has a heterogeneous pore distribution, which means that areas with high and low pore density occur (Heap *et al.*, 2017).

The grain size of the samples shown in Figure 3-3 can be judged as medium to coarse-grained. The distinct reddish colour impression results from the presence of iron oxides, which are sedimentary bound in the sandstone. It can be clearly seen that the soft Buntsandstein specimens are very porous. In Table 11-1, the dimensions of the samples are shown, while Table 5-1 shows the calculated porosity data.

Figure 3-3: Buntsandstein samples DBA5 (left) and DBA6 (right).

3.2.4 Exxon sandstone

The ExxonMobil company operates an oil field near the town of Groß Lessen in the German state of Lower Saxony. The Groß Lessen oil field is part of the so-called “Rotliegend-Basin”, which is a deeply deepened sedimentary basin formed by thick rock layers of Buntsandstein and mudstone during Permian (Gebhardt, 1994). The very porous Rotliegend sandstones serve as the main source of petroleum. The Rotliegend sandstone is often referred to as Buntsandstein, due to the different colours of rock (Heunisch *et al.*, 2017).

In Figure 3-4, the used Rotliegend sandstone specimens are shown. A greyish colouring of the coarse-grained sandstone can be seen. Likewise, stratification and, on a small scale, fractures and folds can be observed. The dimensions and calculated porosity data can be found in Table 11-1and Table 5-1.

Figure 3-4: Exxon mobile sandstone samples 4.1 (left) and 4.2 (right).

4 Methodology

All measurements were made on oven-dry (at 110°C before experimentation), intact sandstone samples under ambient laboratory conditions, with temperatures approximately 20°C.

4.1 Sample preparation

Figure 4-1A pictures a drill core of the Trattnach oil field which was drilled by the RAG Austria AG in a depth of 1600m. The company cut the core in the middle, so the preparation of a sample with cylindrical shape and an approximately 2:1 length to width ratio was quite a challenge. This ratio is necessary for the specimen to be sealed in the Hoek Cell. The drilling procedure was done as shown in Figure 4-1B.

Figure 4-1: A: Drill core of the Trattnach oil field by RAG Austria AG depth 1600m. B: Drilling procedure to obtain a cylindrical shaped sample with an approximate 2:1 length to width ratio.

After drilling, the cylindrical specimens had to be cut to a length of about 100 mm. As a next step, the samples were milled on the faces to produce a planar surface. This is essential to prevent leaks in the test and to ensure a smooth contact surface for the ultrasonic sensors. The exact lengths and diameters of the rock specimens are shown in Table 11-1.

4.2 Methods of quantification

4.2.1 Density

For the calculation of porosity and density according to the formula of Ulusay (2015), the dimensions and weight of the sample are required. Several readings were taken for each dimension using a caliper gauge and then averaged. For cylindrical samples, the bulk volume is expressed as follows:

$$V_{bulk} = r^2 * h * \pi$$

Where,

V_{bulk} = bulk volume [cm³]

r = radius [cm]

h = height [cm]

The buoyancy method, which is based on Archimedes' principle, can also be used. There, the bulk volume is measured from the difference of the saturated and the submerged mass in relation to the water density. The sample is completely immersed in a bucket full of water in a hanging basket (Figure 4-2). This basket is connected to the scale with a wire and thus the mass can be weighed under buoyancy. Afterwards, the sample is taken out of the bucket, dried on the surface by wiping and then the saturated mass is measured.

$$V_{bulk} = \frac{M_{sat} - M_{sub}}{\rho_W}$$

Where,

M_{sat} = saturated mass [g]

M_{sub} = mass under buoyancy [g]

ρ_W = water density [1 g/cm³]

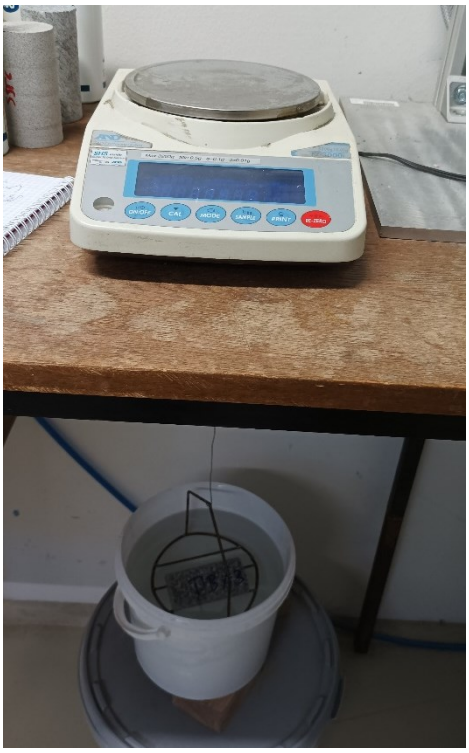

Figure 4-2: Setup of the buoyancy method according to Archimedes' principle. Connection of scale and hanging basket by wire.

The dry masses are measured to an accuracy of 0,01g. Before mass measurement, the samples are oven dried at 110°C for at least 24 hours. The dry bulk density is expressed as:

$$\rho = \frac{M_S}{V_{bulk}}$$

Where,

ρ = dry bulk density [g/cm³]

M_S = dry mass [g]

4.2.2 Porosity

Porosity is the space that is not filled by a solid matrix. The term open porosity is used when there are pores and cracks that are interconnected. Closed porosity occurs when the pores and cracks are isolated. A determination of the total porosity is possible by the addition of open and closed porosity. Open porosity is determined by the water saturation method or by the determination of the true density via gas pycnometry.

Porosity is expressed either as a percentage between 0 and 100% or as a fraction between 0 and 1. Porosity is calculated with the following relationship:

$$\Phi = \frac{V_{pore}}{V_{bulk}}$$

Where,

Φ = porosity [1]

V_{pore} = pore volume [cm³]

V_{bulk} = bulk volume [cm³]

4.2.2.1 Porosity determination using water saturation

The saturation method is used to determine the effective (open) porosity. First, the sample is dried in the oven at 110°C and then weighed (M_s). As shown in Figure 4-3A, the samples are placed in a desiccator. To create a vacuum, the connected vacuum pump is turned on for about 5 minutes before distilled water is added to the desiccator. It should be noted that the stopcock for admitting the water must be operated with care in order to maintain the vacuum. The water filling quantity must be selected to ensure that all samples are completely soaked in water (Figure 4-3B).

Figure 4-3: A: Creation of vacuum before adding distilled water. 1 = stopcock. B: Desiccator filles with distilled water and rock samples.

After the desiccator is filled, the vacuum pump is turned on again, saturating the samples with water. 24 hours later, the samples are removed and weighed again (M_{sat}). The pore volume is calculated as:

$$V_{pore} = \frac{M_{sat} - M_s}{\rho_w}$$

Where,

V_{pore} = pore volume [cm³]

M_{sat} = saturated mass [g]

M_s = dry mass [g]

ρ_w = water density [1 g/cm³]

4.2.2.2 Gas pycnometry

Based on the expansion of helium gas, a gas pycnometer (Figure 4-4A) is also used to determine the effective porosity. In fact, the true density is measured, and the effective porosity is calculated from this. Helium is used because it behaves like an ideal gas and can penetrate into the very small pores and cracks due to its small atomic size. Due to this property of helium, this method provides slightly higher porosity values than, for example, the water saturation method mentioned above.

Figure 4-4: A: Top view of the gas pycnometer Ultrapyc 5000 from Anton Paar. B: Sample chamber filled with the Trattnach sandstone. C: Sample chamber filled with the Ruhrsandstone.

A sample of known mass is placed in a sample chamber of known volume (Figure 4-4B & C). This chamber is then sealed and filled with an inert gas at a predefined pressure. After pressure stabilization in the sample chamber, a valve is opened which establishes a connection with a reference chamber of known volume. The gas spreads into the new volume and pressure readings are used to calculate the volume of the sample. The Ultrapyc 5000 gas pycnometer from Anton Paar was used. The sample volume is calculated with the following working equation:

$$V_S = V_C - \frac{V_R}{\frac{p_i}{p_f} - 1}$$

Where,

V_s = sample volume [cm³]

V_C = volume of the empty sample chamber [cm³]

V_R = volume of the reference chamber [cm³]

P_i = initial pressure [bar]

P_f = final pressure after expansion [bar]

To calculate the porosity from the true density, the following formula is used:

$$\Phi = 1 - \frac{\rho}{\rho_0}$$

Where,

ρ = bulk density [g/cm³]

ρ_0 = true density [g/cm³]

4.2.3 Ultrasonic measurements

Ultrasonic measurements in this study are performed using a two-transducer pulse transmission technology (Birch, 1960). An ultrasonic wave is emitted from the source transducer at one end of the sample and is picked up by the receiver transducer at the other end of the sample (Figure 4-5). Usually, specimens which are subjected to loads are used in cylindrical shape. In this work, ultrasonic measurements are performed on different sandstone samples. A pair of P-transducers was used for the measurement. Due to the electrical pulse, the piezoelectric element in the source transducer experiences mechanical deformation and generates an elastic wave in the specimen. These waves cause the deformation of the receiver transducer, which in turn generate an electric charge on the electrodes of the transducer (Yurikov *et al.*, 2019). A potential difference results between the electrodes, which can be recorded digitally.

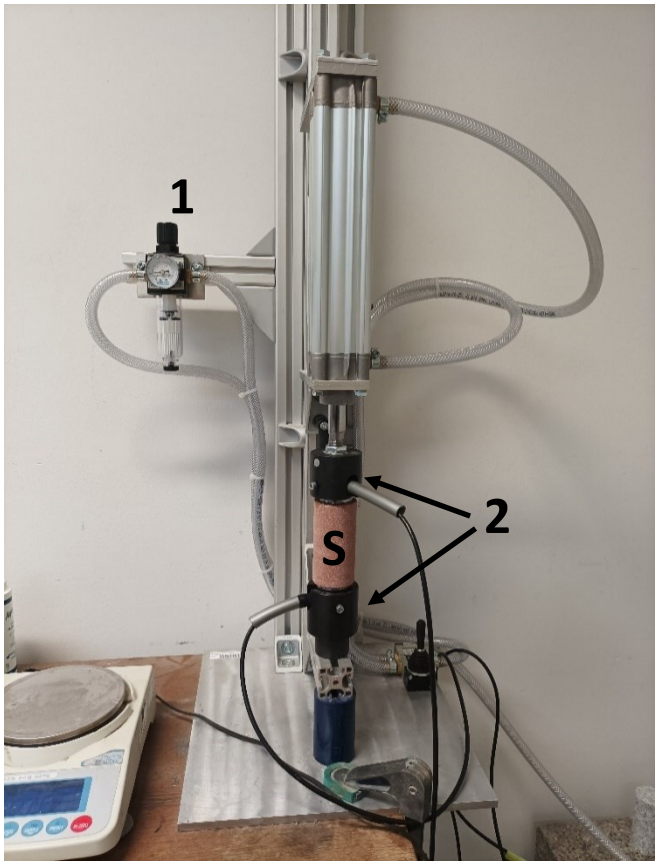

Figure 4-5: Setup of the ultrasonic measurement. 1 = Manometer for compressed air indication; 2 = S-transducer; S = Sample.

The P-wave velocity is calculated using a MatLab code. Input parameters are the sample height as well as the diameter and the traveltime spectrum generated by the ultrasonic measurement. The code calculates the AIC vector, which is used to determine the optimal statistical model for the data. After that, it searches for the local minimum of the AIC vector, which is required to calculate the first arrival of the p-wave. The ultrasonic velocity is then calculated by dividing the length of the sample by the time it takes for the ultrasonic waves to travel through the specimen.

Figure 4-6A shows a typical waveform recorded by the P-transducer pair during the experiments. The x-axis shows the travel time of the wave in microseconds. On the y-axis the amplitude is shown, which is given in volts. The first occurrence of energy denotes the travel time of a P-wave. The velocity of such a wave is calculated as $v_P = L/t_P$, where L represents the sample length. In these experiments, the UP-250 ultrasonic transducers from Geotron-Elektronik were used. Due to the wide frequency spectrum, which reaches up to 250 kHz, they are particularly well suited for short and medium measuring distances. Through the small wavelength in the material, a high measurement accuracy is guaranteed.

Figure 4-6B shows the installation of the P-transducers in pressure plates. These plates can be installed in the rock testing press and a measurement could be made during pore pressure loading. The problem with this test is the metal stamps. However, an ultrasonic measurement to check the signal transmission through the stamps showed that they do not conduct the signal (Figure 4-6C). Thus, the possibility of direct measurement in the system is not given.

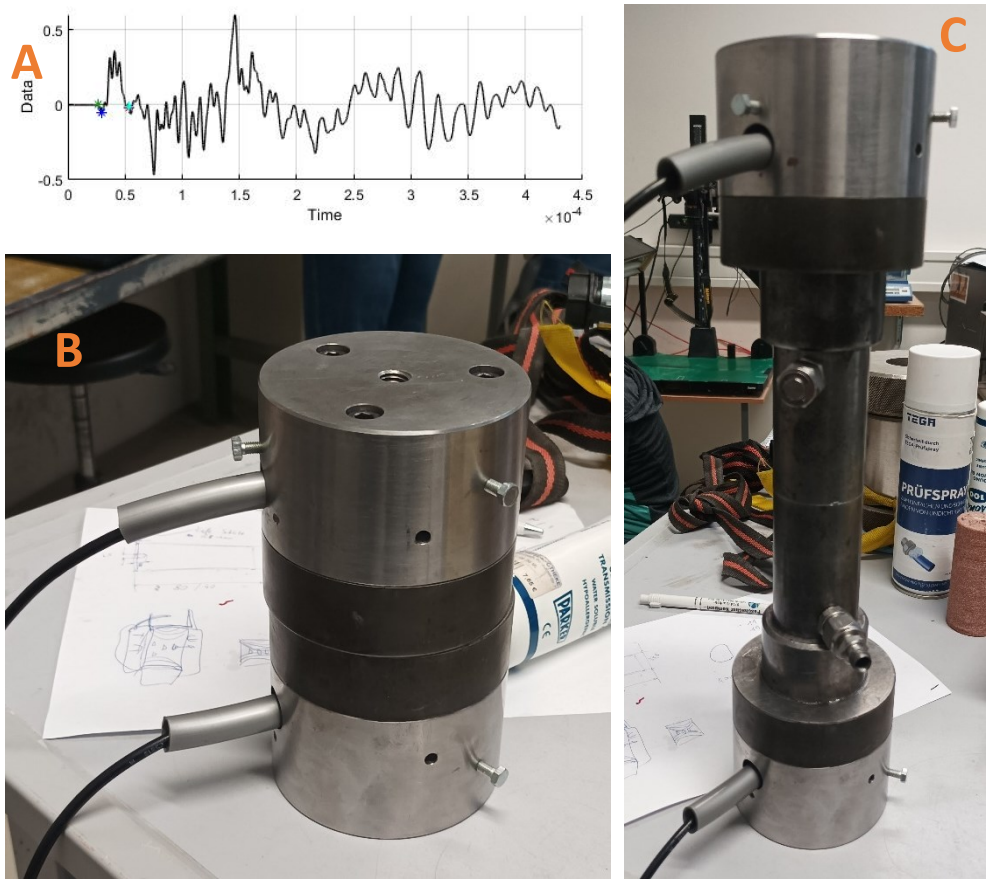

Figure 4-6: A: Typical waveform recorded by the S-transducers. B: S-transducer installed in pressure plates, which can be mounted in the rock testing press. C: Ultrasonic measurement to check signal transmission through the metal stamps.

4.3 Experimental setup

The experimental setup was developed by myself for this thesis and is based on a steady state permeameter setup (Hill, 2019). In Figure 4-7 the schematic test setup is pictured. The filling pressure of the nitrogen gas bottle is 200 bar. Consequently, all components as well as the stainless-steel line are designed for this pressure to ensure the tightness of the system.

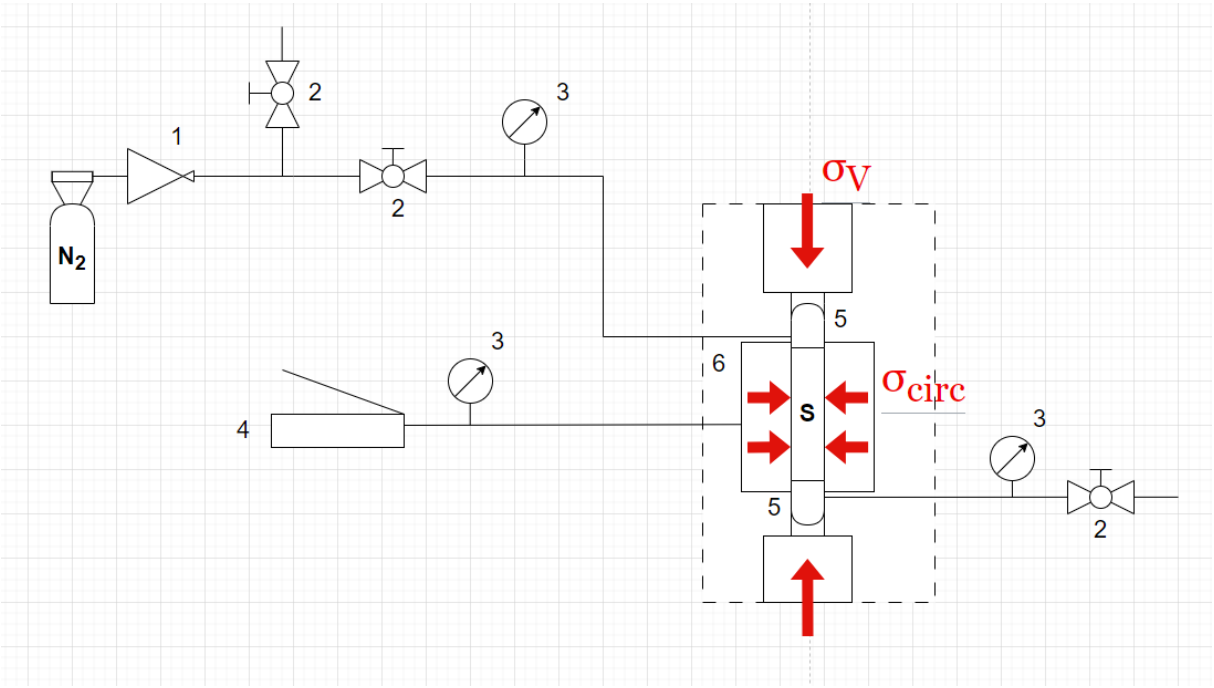

Figure 4-7: Schematic test setup. 1 = pressure regulator; 2 = shut-off valve; 3 = manometer; 4 = hydraulic hand pump; 5 = in- & outlet stamp; 6 = Hoek cell; σ_V = vertical stress; σ_{circ} = circumferential stress; S = sample. The dashed line simulates the rock testing machine.

To precisely control the gas pressure, a pressure regulator is mounted directly on the gas cylinder. On the one hand, this shows the pressure of the cylinder contents, and, on the other hand, the desired working pressure can be set. The shut-off valves are important to control the pressure changes and to interrupt the gas flow to take the sample out of the system. Furthermore, analogue manometers are installed before and after the Hoek cell.

The in- and outlet stamps ensure the gas flow through the rock sample (Figure 4-8A). For this purpose, the specimen length is of great importance, since the stamps must reach into the membrane of the Hoek cell to guarantee the tightness of the system under circumferential stress. To not damage the connection of the stainless-steel line with the weight of the pressure vessel of the Hoek cell, some wood has to be underlaid. These connections (Figure 4-8B) must be handled carefully, as they must be disconnected from the stainless-steel line each time a specimen is removed or installed. Blind caps are placed opposite the connection to prevent leakage of the system.

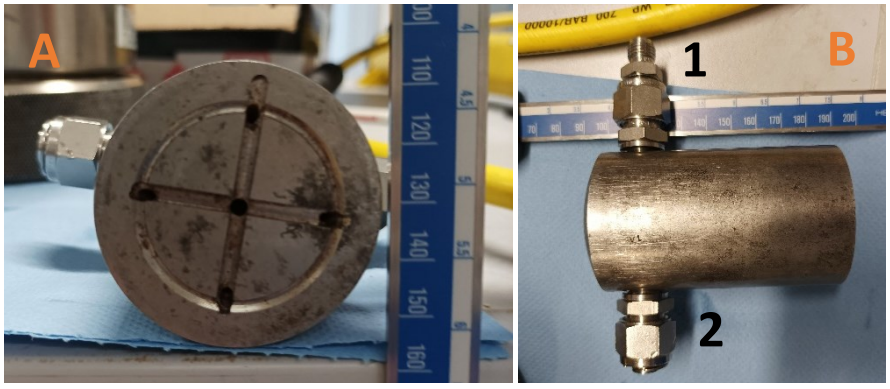

Figure 4-8: A: Contact surface of the in- & outlet stamp. B: Height of the in- & outlet stamp. 1 = Connection for stainless-steel line; 2 = Blind cap to ensure tightness.

The Hoek cell system is a manual pressure system which maintains constant lateral pressure in the Hoek cell. To ensure this pressure, the Hoek Cell is connected with a hydraulic handpump with oil reservoir via a flexible hose (Figure 4-9A). This handpump is the P392 model from Enerpac. Due to the increase of oil pressure, the rubber sealing sleeve presses against the surface of the rock sample and seals the gas system. The Built-in Hoek cell in the gas system is shown in Figure 4-9B. To measure the fluid pressure in the Hoek cell, an analogue manometer is installed in the Hoek cell system.

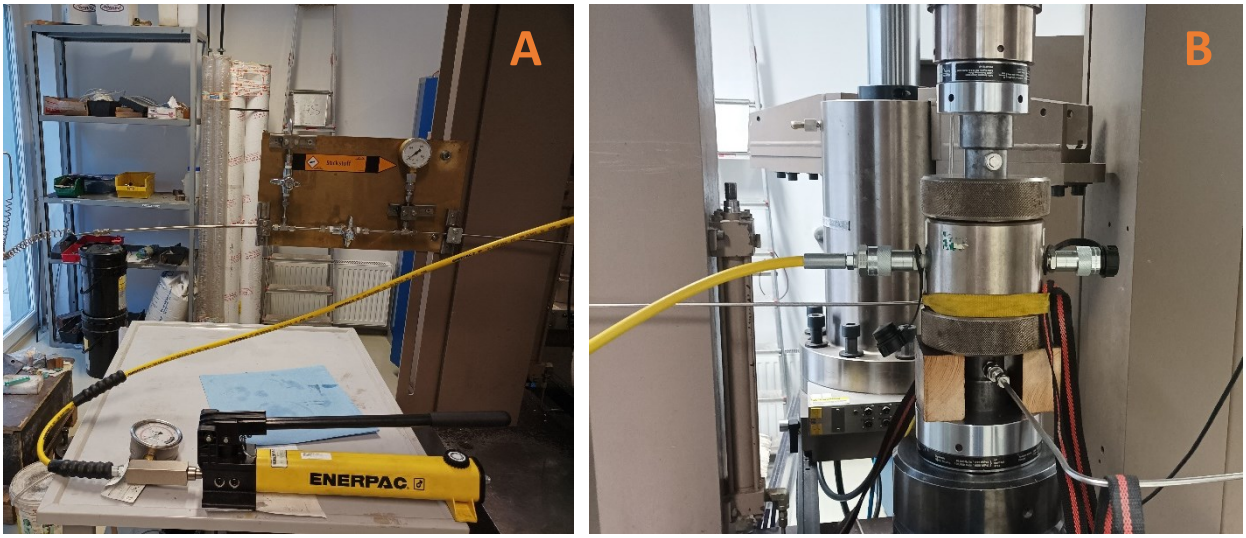

Figure 4-9: A: Hydraulic Handpump with oil reservoir and analogue manometer. B: Built-in Hoek cell in the experimental system with flexible connection to the handpump.

An overview of the installation of the Hoek cell in the rock testing machine is shown in Figure 4-10A. This machine is a servo-hydraulic rock testing press type MTS 815. The press is used as standard for uniaxial or triaxial compression tests. In the test sequences described later, a vertical stress is applied using the rock testing press. Using the hydraulic hand pump connected to the Hoek cell, the specimen is subjected to a circumferential stress. These two stresses simulate the conditions of the rock at a certain depth. Figure 4-10B shows a side view of the components in front of the Hoek cell. The shut-off valve, which is directed upwards via a T-piece, is used to release pressure from the system. This must be kept closed during an ongoing test. The components after the Hoek cell are shown in Figure 4-10C. The manometer after the sample should display the same pressure as the manometer before the sample. If this is the case, the system is considered tight, and the specimen is considered saturated with gas. The shut-off valve at the end of the system must also be kept closed during an ongoing test.

Figure 4-10: A: Overview of the actual test setup from the front. B: Side view from the left. C: Side view from the right. 1 = pressure regulator; 2 = shut-off valve; 3 = manometer; 4 = hydraulic hand pump; 5 = in- & outlet stamp; 6 = Hoek cell.

4.3.1 Experiment 1: Gradual increase of gas pressure

Before the samples were installed in the Hoek cell, the P-wave velocity was measured. After installation, the surrounding conditions are established based on a certain depth. The sample is loaded vertically with a stress of 30 MPa and circumferentially with a stress of 10 MPa. The loading by the rock testing press and the hydraulic hand pump must be simultaneous and gradual. When the required conditions are achieved, gas at a pressure of 1 MPa is injected into the system. The specimen is loaded with this pressure for 10 minutes. Then the sample is depressurized, unloaded, and carefully removed, and the P-wave velocity is measured again. After the measurement, the sample is reinstalled and the experiment starts again, but with the difference that the injected gas pressure is increased by 1 MPa. This is repeated again and again until a gas pressure of 9 MPa is reached. Thus, for each sample, this experiment has to be performed 9 times. Since the circumferential pressure is set to 10 MPa, this value is also the limit for the gas pressure. If the gas pressure is higher than the circumferential pressure, the tightness of the system can no longer be guaranteed. As there are many removals and installations during this experiment, it is important to check the connections for tightness using a sealing spray. This check must be performed each time the system is reinstalled.

The purpose of this experiment is to load the sample with gas in certain environmental conditions with gas simulating the pore pressure and to check if this causes damage to the sample. This damage should be detected by using the ultrasonic measurements.

4.3.2 Experiment 2: Cyclical pore pressure loading of the sample

The second experiment should simulate a process where gas is injected into and extracted from a sandstone. As in experiment 1, the vertical stress is set at 30 MPa and the circumferential stress at 10 MPa. For the simulation of the injection and extraction process, a cyclic pore pressure loading and unloading of the sample is necessary. Therefore, the sample is installed as in test 1, checked for tightness and then loaded with 1 MPa for 10 minutes. After this time, the gas pressure is increased to 9 MPa and the specimen is again loaded for 10 minutes. As the next step, the pressure on the pressure regulator is reduced again to 1 MPa and the procedure starts once more. This is done by carefully opening and closing the shut-off valves. This pore pressure loading and unloading are carried out 5 times directly in a row, without removal and installation.

Like in experiment 1, an ultrasonic measurement is performed before and after the experiment to detect possible damage caused.

4.4 Fast Fourier-Transformation

For the Fast Fourier Transformation (FFT), the text files obtained from the ultrasonic measurements are read into MatLab and a Fourier spectrum is created based on a code. As input parameters, as in the calculation of the p-wave velocity, the length and the diameter of the sample are necessary. The code calculates the discrete Fourier spectrum of a signal.

First there is a calculation of the sampling time, from which the sampling frequency is calculated. With this the Nyquist frequency is determined, which indicates the highest frequency that is represented in the signal. The signal is limited to a specific length and a cosine window applied to reduce edge effects and improve the FFT. The calculation of the discrete Fourier spectrum is performed by the FFT. The spectrum is then plotted against frequency and mean, and median frequencies are calculated.

5 Results

5.1 Density and Porosity

The calculation of pore volume as well as bulk volume and porosity are depicted in Table 5-1 and show slightly different trends for the individual samples. A small porosity decrease of about 0,8-1,2% is observed in samples DBA1, 2, 5 and 6 between before applying pore pressure and after applying pore pressure. For the Trattnach specimens (4.1 and 4.2), the decrease is much more significant, and the porosity shrinks to about half. Samples 1R and 2R show an increasing porosity trend, making them stand out from the other samples. The bulk volume is calculated according to the water saturation (see formula in 4.2.2.1).

Table 5-1: Porosity calculation before and after applying pore pressure. The data shaded in light grey are those after the gas loading, while the data shaded in dark grey are those of the unaffected samples.

Status	Before	After	Before	After	Before	After
Sample	V_{pore} [cm³]	V_{pore} [cm³]	V_{bulk} [cm³]	V_{bulk} [cm³]	Porosity [%]	Porosity [%]
DBA1	8.73	7.21	197.21	197.08	4.43%	3.66%
DBA2	9.29	6.97	197.45	197.04	4.70%	3.54%
DBA5	40.02	38.06	194.57	193.79	20.57%	19.64%
DBA6	35.31	33.24	188.74	187.52	18.71%	17.73%
1R	30.58	33.69	136.71	138.26	22.37%	24.37%
2R	29.9	36.41	147.82	152.28	20.23%	23.91%
4.1	29.12	11.53	157.51	156.89	18.49%	7.35%
4.2	31.14	15.42	156.36	155.69	19.92%	9.90%

The results of the gas pycnometry are shown in Table 5-2. The dark grey shaded data show the calculation before applying pore pressure and the light shaded show the data after applying pore pressure. The porosity calculated from the bulk density and the grain density are higher than those calculated by water saturation.

Table 5-2: Difference between calculated density and measured grain density. Porosity calculation based on grain density.

Status	Before	After	Unloaded	Before	After
Sample	Density [g/cm³]	Density [g/cm³]	Grain density [g/cm³]	Porosity [%]	Porosity [%]
DBA1	2.54	2.54	2.69	5.70%	5.58%
DBA2	2.51	2.52	2.69	6.56%	6.32%
DBA5	2.07	2.08	2.76	24.98%	24.69%
DBA6	2.11	2.13	2.76	23.32%	22.84%
1R	2.05	2.01	2.67	22.97%	24.73%
2R	2.12	2.04	2.67	20.58%	23.61%
4.1	2.17	2.18	2.64	17.74%	17.57%
4.2	2.07	2.07	2.64	21.80%	21.63%

5.2 Experiment 1

Figure 5-1 shows the results of the first experiment of sample 1R at different pore pressures. The travel time is plotted on the x-axis, while the amplitude is shown on the y-axis. Before applying any pore pressure (0 bar) the sample, a travel time of 59,88 µs was measured. Due to the applied confining pressure the time already slows down to 64,50 µs at 10 bar. The slowest time was measured with 69,75 µs at 40 bar. The travel times then become a bit faster again.

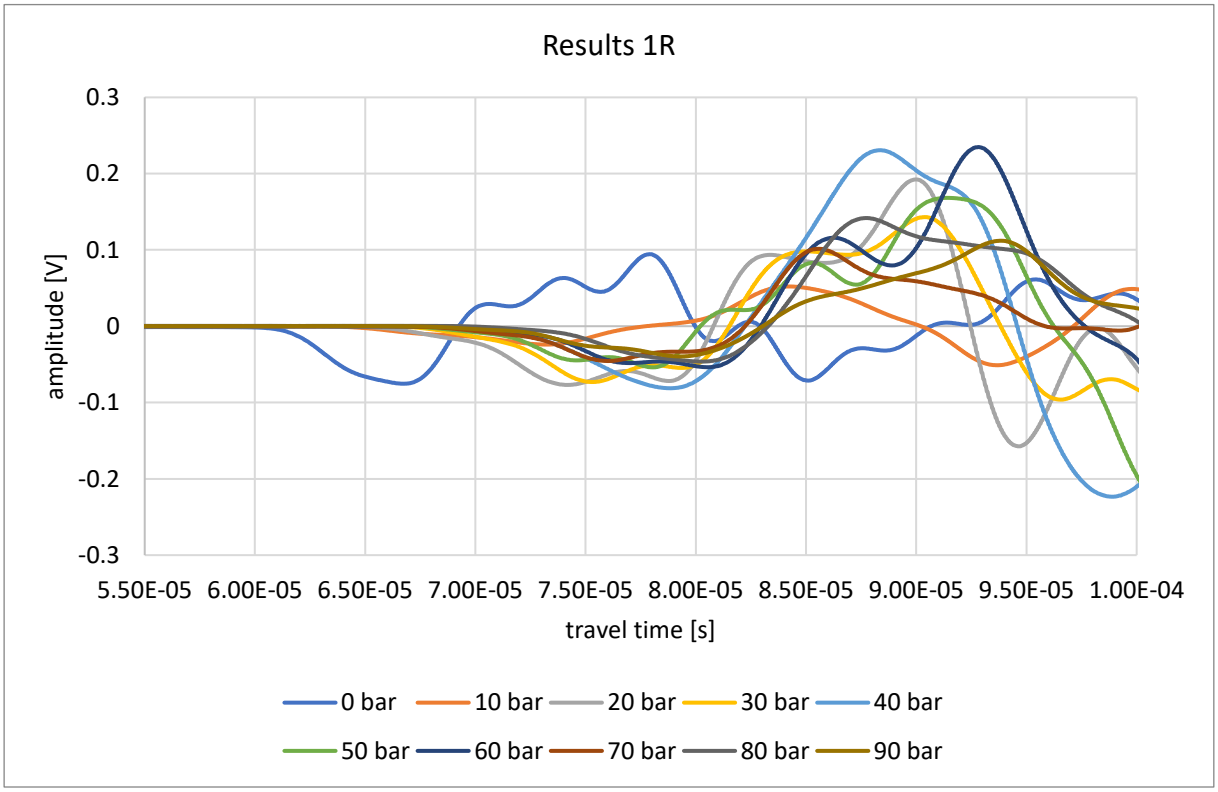

Figure 5-1: Diagram of the ultrasonic measurements after different pore pressures of the sample 1R.

The increase in the travel time of sample 2R from 64,18 µs before applying pore pressure (0 bar) to 65,25 µs (10 bar) can be seen in Figure 5-2. The slowest time was measured with 73,35 µs at 40 bar.

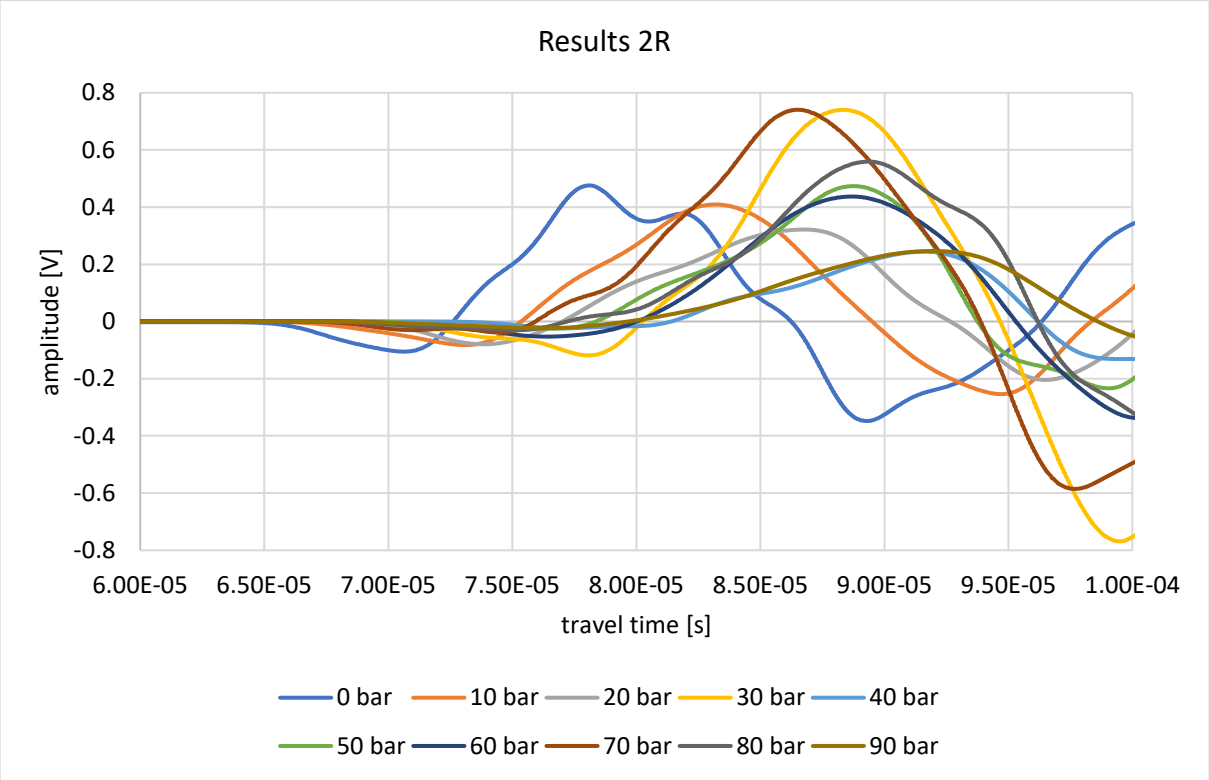

Figure 5-2: Diagram of the ultrasonic measurements after different pore pressures of the sample 2R.

In Figure 5-3 the results of sample DBA1 show an increase from 25,25 µs at 0 bar to a value of 27,07 µs at 90 bar. A small but constant rise in travel time can be observed. It was also found that the gas flow through the specimen occurred only from 70 bar.

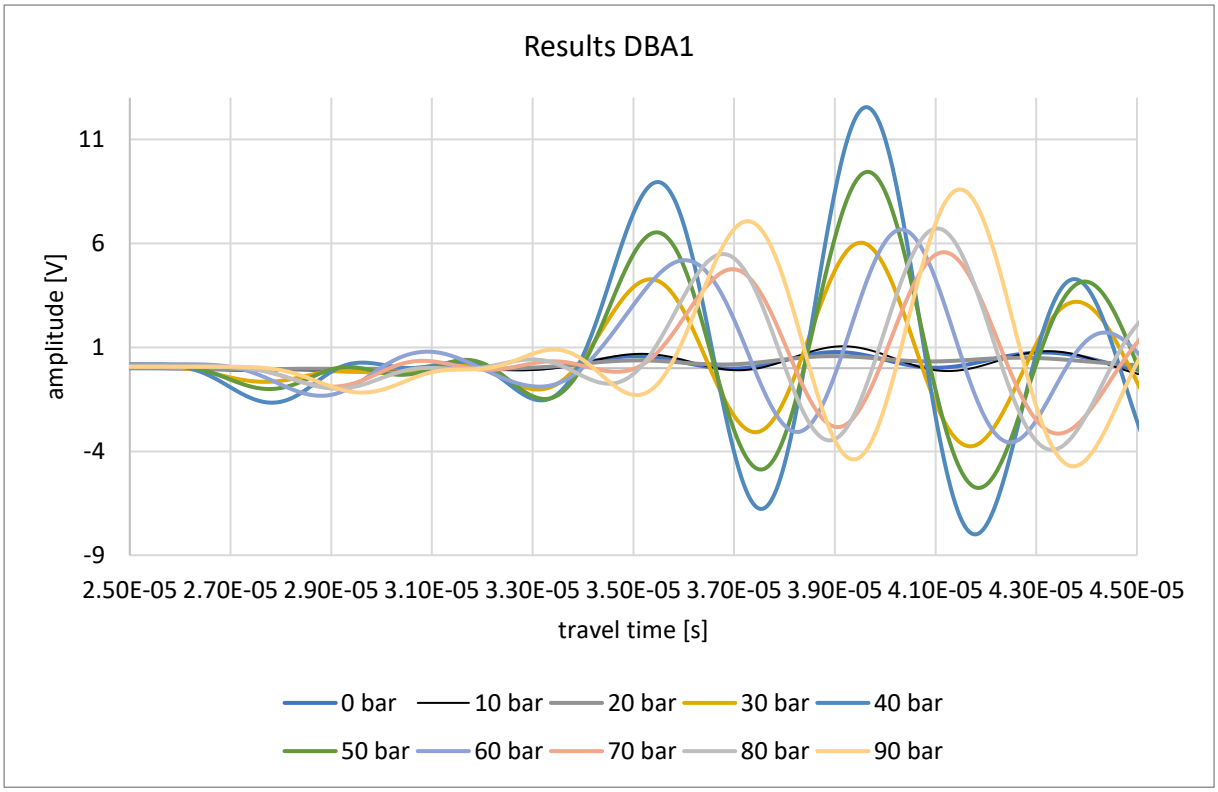

Figure 5-3: Diagram of the ultrasonic measurements after different pore pressures of the sample DBA1.

In Figure 5-4 the results of sample DBA2 are depicted. Before applying pore pressure (0 bar), a travel time of 24,98 µs was measured. Due to the pressure increase, the time slightly and constantly slows down to a maximum from 26,07 µs at 70 bar. As in sample DBA1, the gas flow also only occurs from 70 bar.

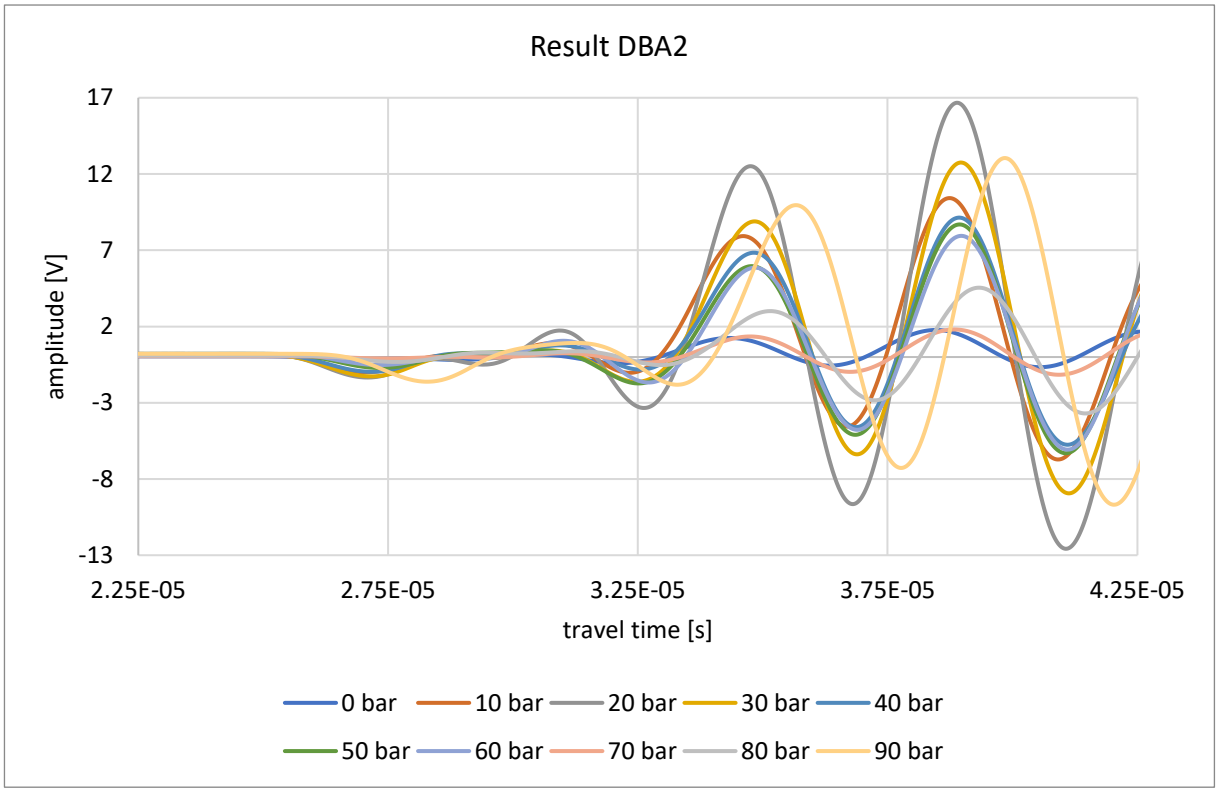

Figure 5-4: Diagram of the ultrasonic measurements after different pore pressures of the sample DBA2.

With the ultrasonic measurements the data were obtained, which are visible in Figure 5-5. The increase in the travel time value from 35,01 µs before applying pore pressure to a maximum of 37,20 µs at 90 bar was measured. A small but constant rise in time can be observed through the different gas pressures.

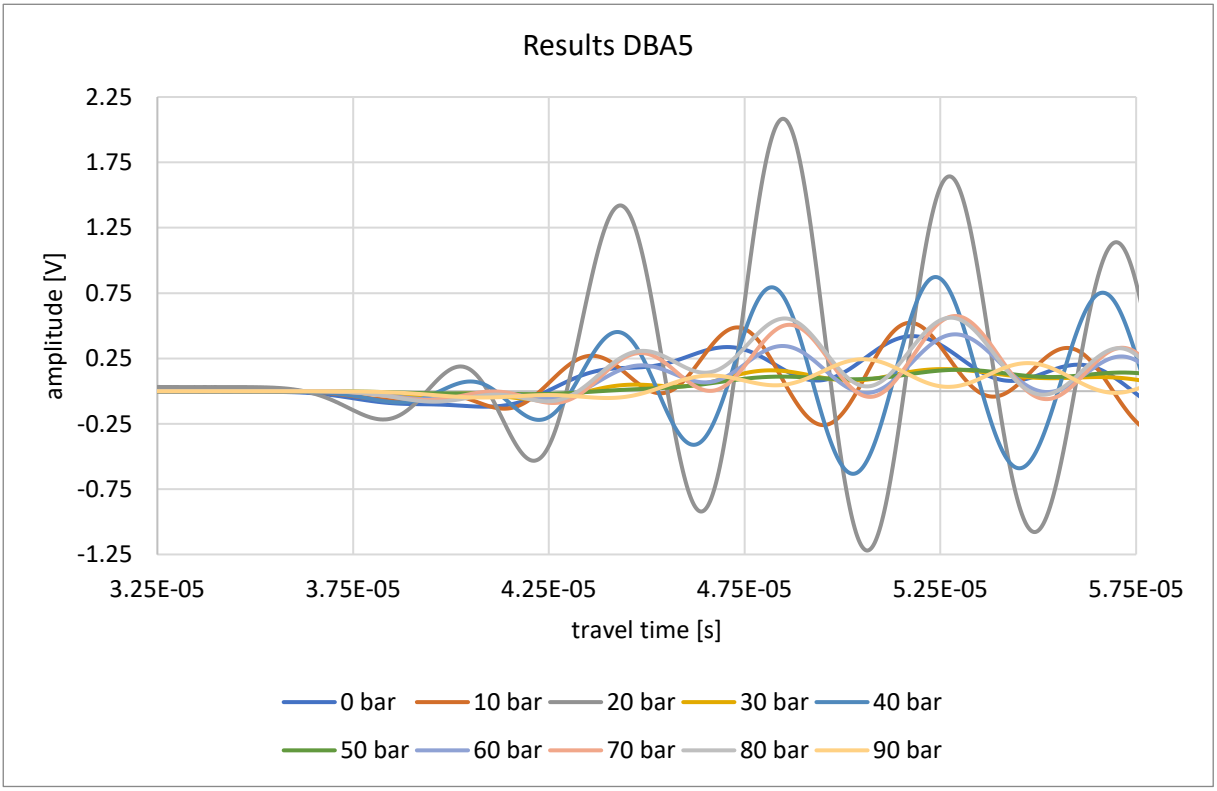

Figure 5-5: Diagram of the ultrasonic measurements after different pore pressures of the sample DBA5.

The results of sample DBA6 are visible in Figure 5-6. The travel time before applying pore pressure was 35,07 µs, which increased slowly and constantly to a maximum of 37,81 µs at 70 bar. The travel times then become a bit faster again.

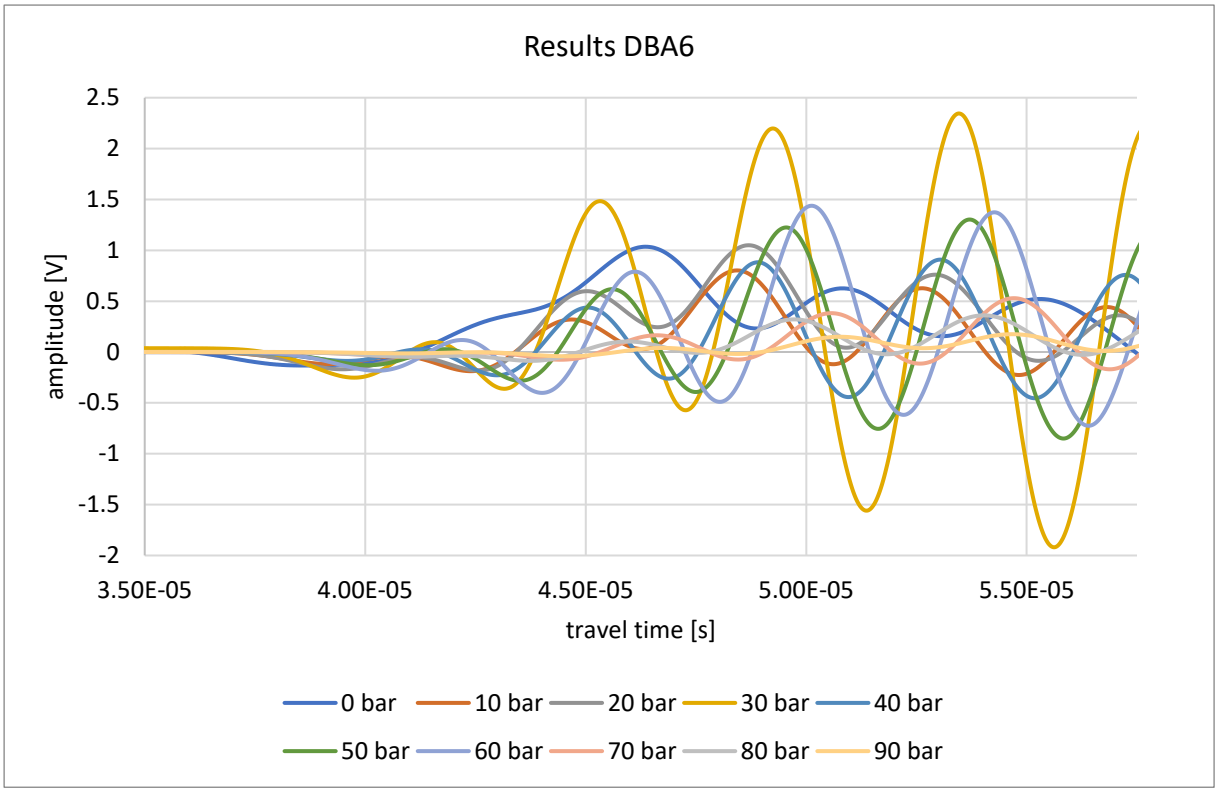

Figure 5-6: Diagram of the ultrasonic measurements after different pore pressures of the sample DBA6.

In Figure 5-7 the gained data of sample 4.1 is depicted. At 0 bar the travel time shows a value of 23,71 µs, which is rising to 25,17 µs at 10 bar. Thereafter, the time varies a little bit until it reaches a maximum of 25,25 µs at 80 bar.

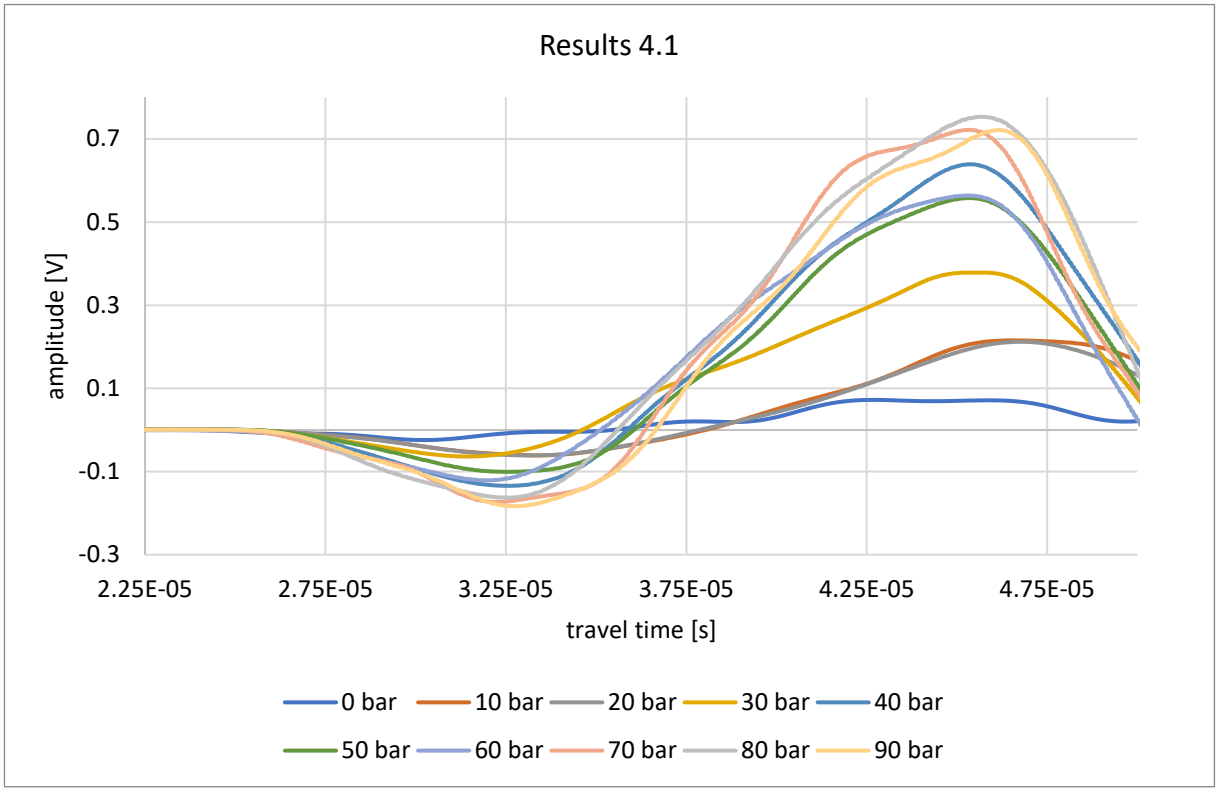

Figure 5-7: Diagram of the ultrasonic measurements after different pore pressures of the sample 4.1.

The increase in travel time of sample 4.2 from 25,36 µs before applying pore pressure to 25,60 µs at 10 bar is shown in Figure 5-8. The slowest time was measured at 26,52 µs at 80 bar. In between, slight fluctuations in travel time can be seen.

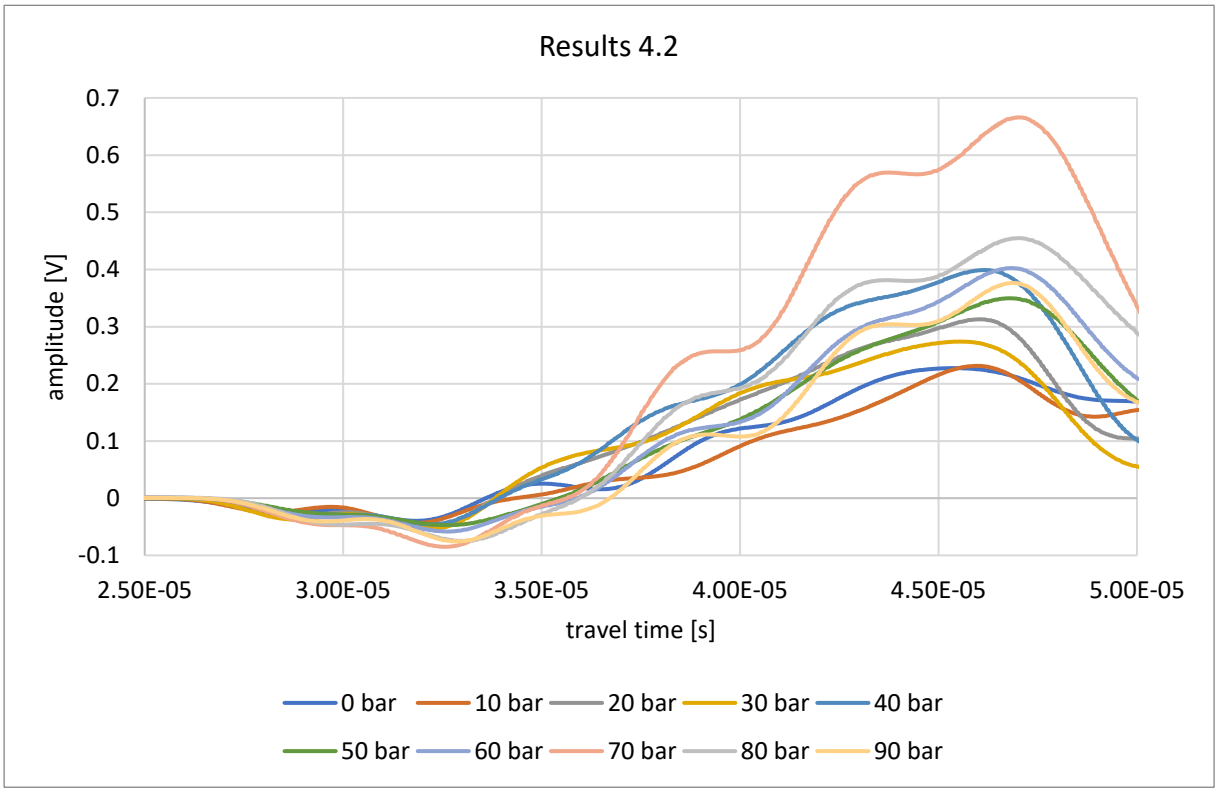

Figure 5-8: Diagram of the ultrasonic measurements after different pore pressures of the sample 4.2.

5.3 Experiment 2

In Figure 5-9 the results of sample 1R before and after cyclical pore pressure loading are depicted. A travel time decrease from 68,75 µs to 67,00 µs was measured.

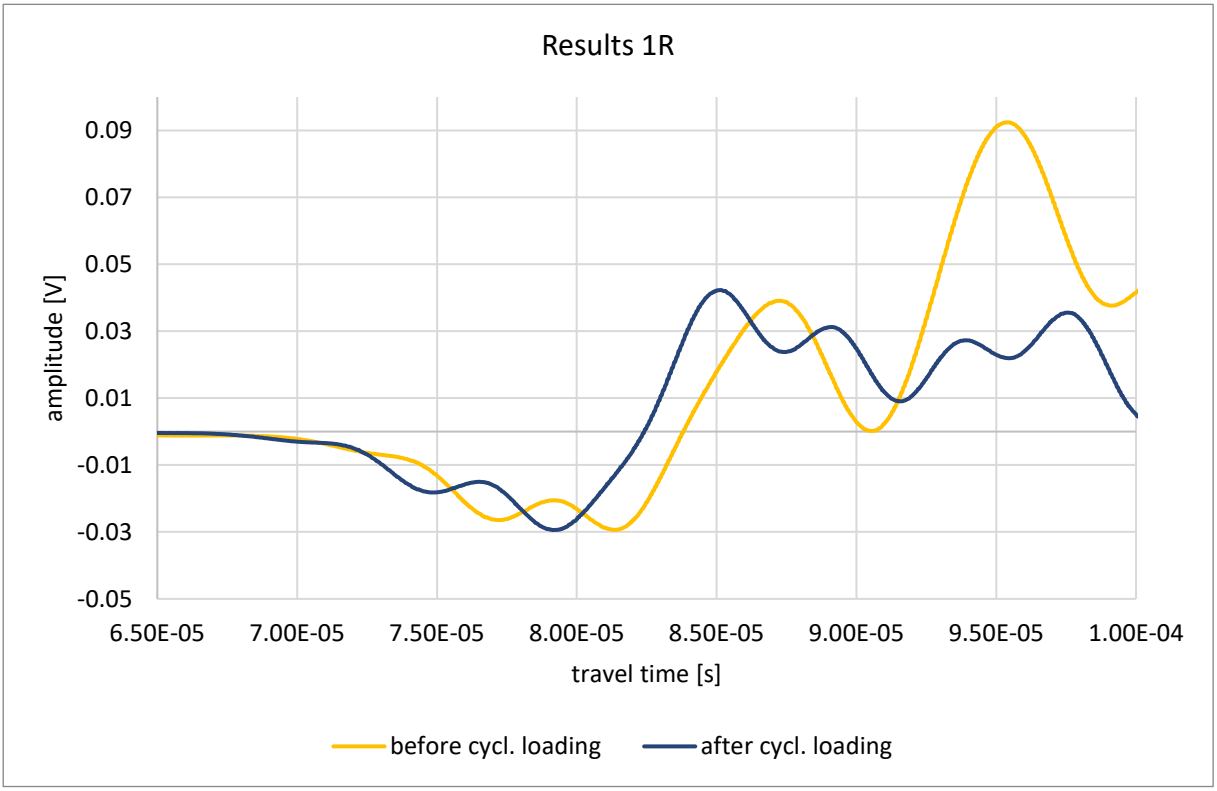

Figure 5-9: Diagram of the ultrasonic measurements before and after cyclical pore pressure loading of the sample 1R.

The travel time increase from sample 2R from before applying pore pressure at 69,09 µs to 69,27 µs after applying pore pressure is shown in Figure 5-10.

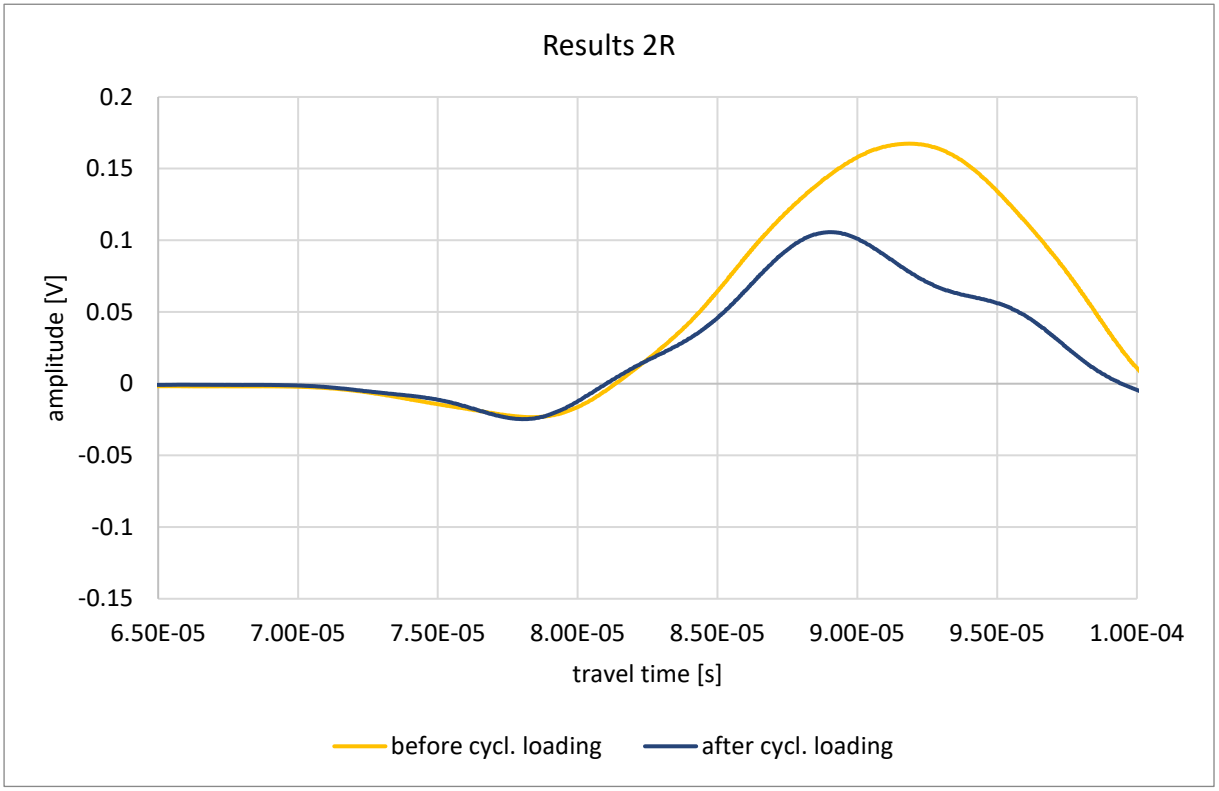

Figure 5-10: Diagram of the ultrasonic measurements before and after cyclical pore pressure loading of the sample 2R.

In Figure 5-11 the gained data of sample DBA1 is depicted. The travel time before applying pore pressure shows a value of 26,94 µs, while after the cyclical pore pressure loading a value of 26,68 µs was measured.

Figure 5-11: Diagram of the ultrasonic measurements before and after cyclical pore pressure loading of the sample DBA1.

In Figure 5-12 the travel times of sample DBA2 are shown. Before applying pore pressure, a value of 25,70 µs was measured, while the value increases after applying pore pressure to 26,58 µs.

Figure 5-12: Diagram of the ultrasonic measurements before and after cyclical pore pressure loading of the sample DBA2.

In Figure 5-13 the results of sample DBA5 are illustrated. The travel time shows an increase from 36,37 µs before applying pore pressure to 37,52 µs after applying pore pressure.

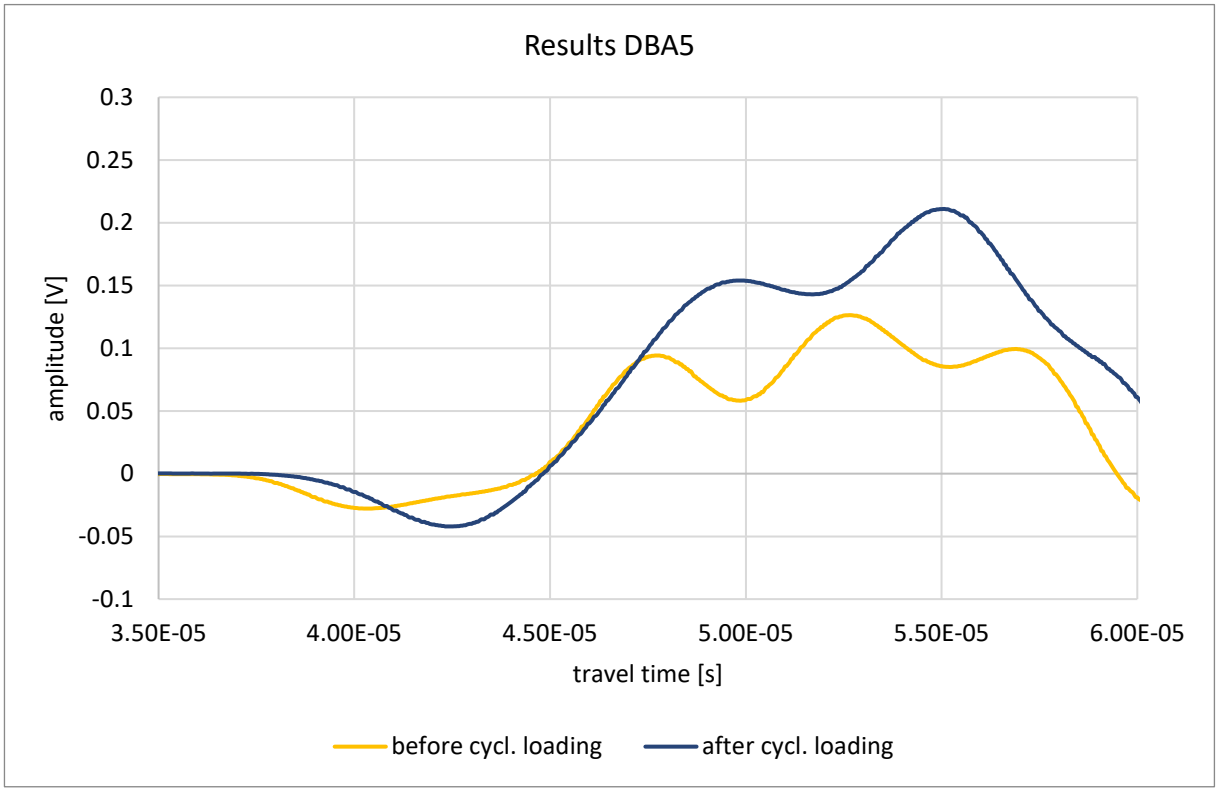

Figure 5-13: Diagram of the ultrasonic measurements before and after cyclical pore pressure loading of the sample DBA5.

The results of sample DBA6 are shown in Figure 5-14. A rise in travel time from 38,09 µs before applying pore pressure to 38,50 µs after applying pore pressure was determined.

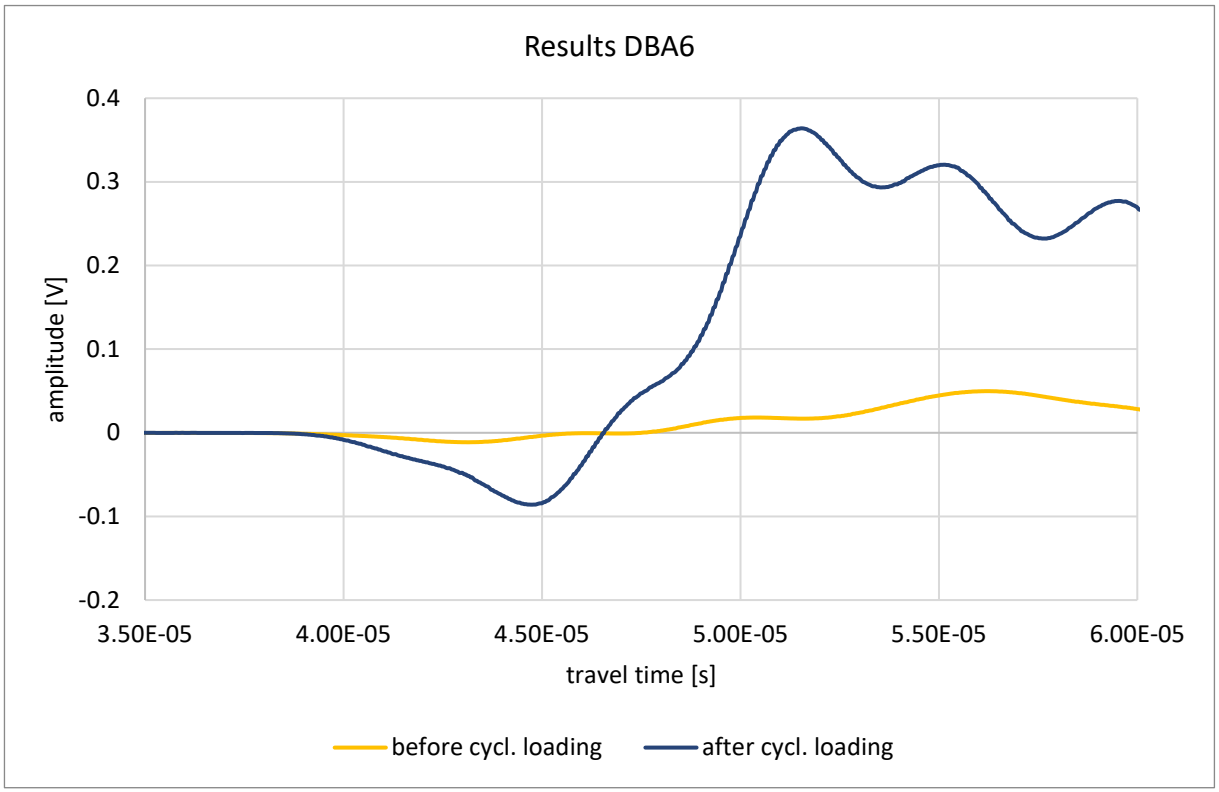

Figure 5-14: Diagram of the ultrasonic measurements before and after cyclical pore pressure loading of the sample DBA6.

Figure 5-15 depicts the results of sample 4.1. Before applying pore pressure, the travel time shows a value of 25,15 µs, while it increases to 26,80 µs after applying pore pressure.

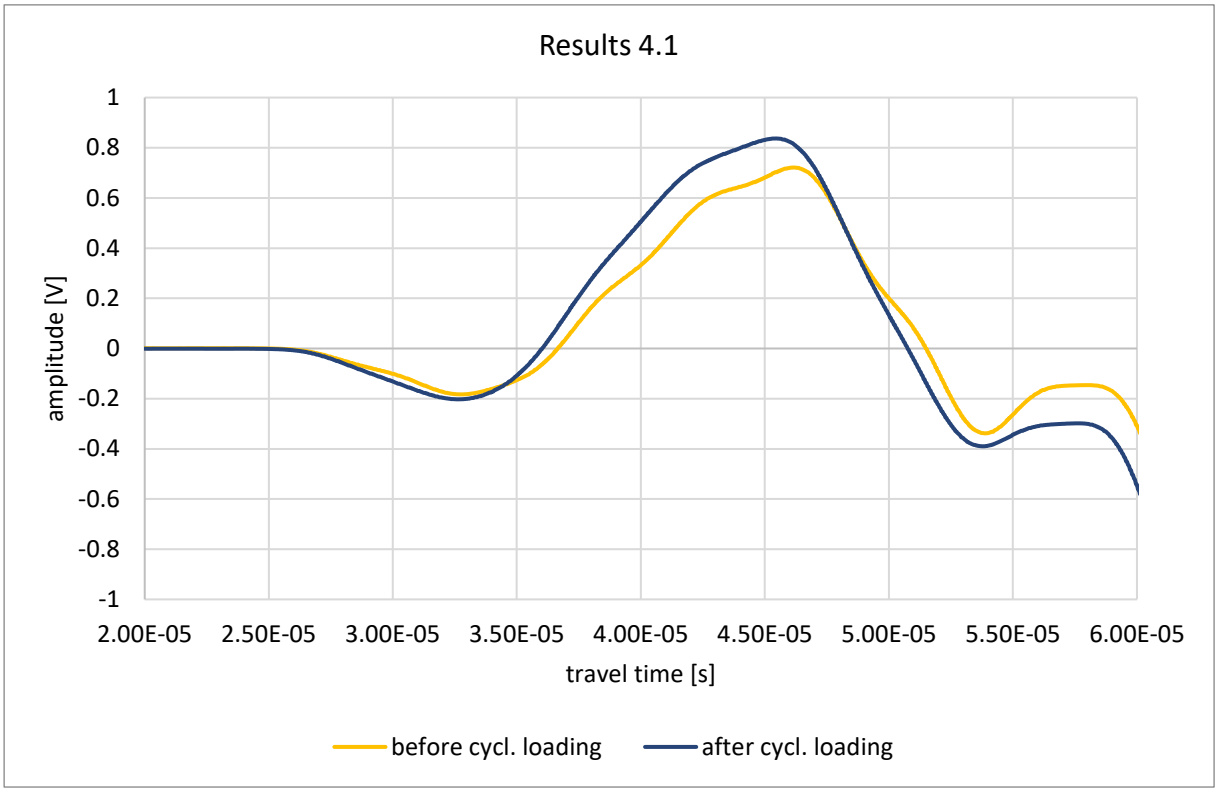

Figure 5-15: Diagram of the ultrasonic measurements before and after cyclical pore pressure loading of the sample 4.1.

In Figure 5-16 the results of sample 4.2 are visible. The travel time before applying pore pressure shows a value of 26,41 µs which decreases to 25,67 µs after applying pore pressure.

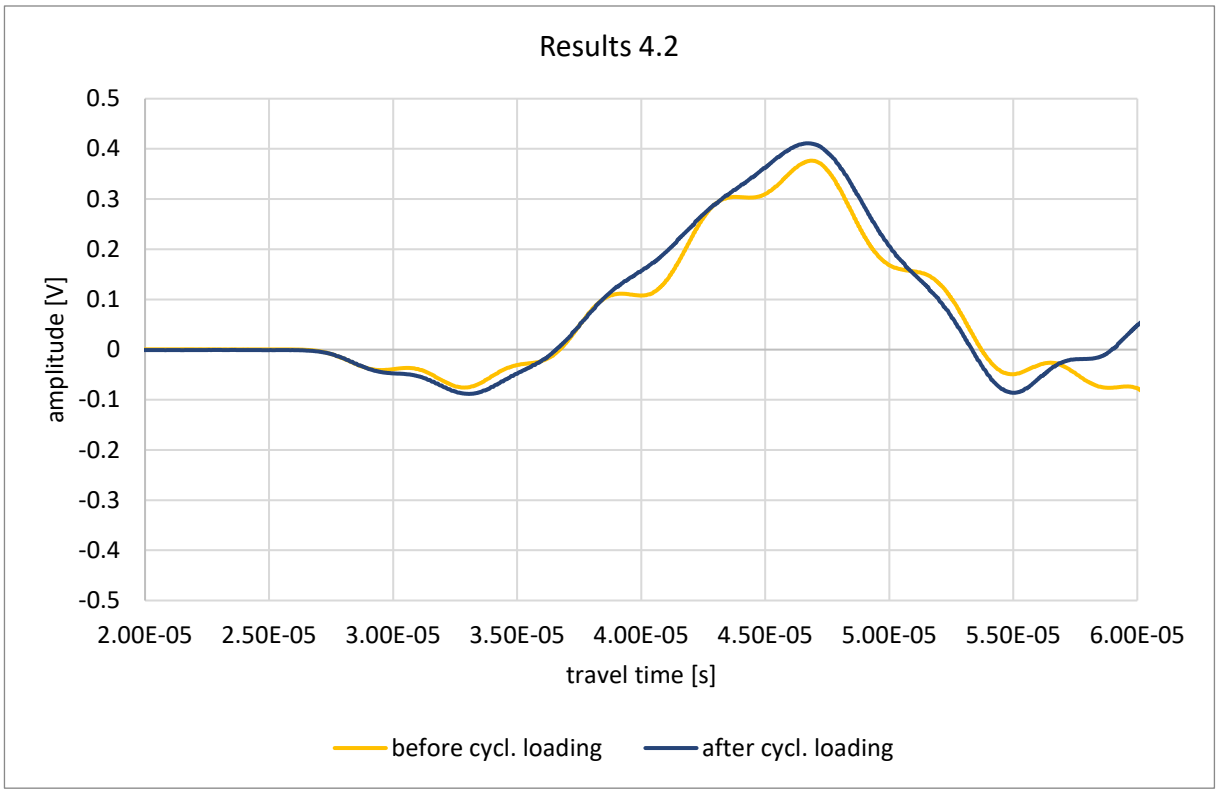

Figure 5-16: Diagram of the ultrasonic measurements before and after cyclical pore pressure loading of the sample 4.2.

5.4 Fourier-Transformation

As well as for the travel time curves, the amplitude is very sensitive. The value of the amplitude is not very representative, so the main focus lies on the occurring frequency components and whether or not they change, disappear or new ones are added. The calculated median and mean frequency can be seen in Table 11-3 and Table 11-4.

5.4.1 Experiment 1

In Figure 5-17 the Fourier spectrum of sample 1R is depicted. The main spectrum regarding the frequency components looks nearly the same for all pressures. There are just some small displacements visible.

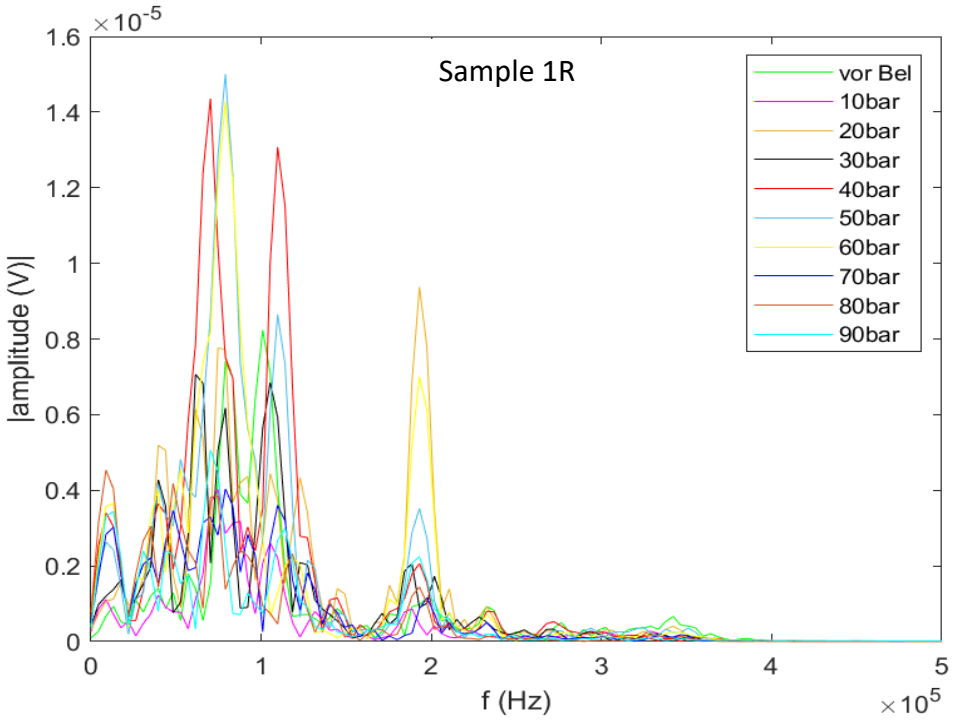

Figure 5-17: Fourier spectrum of sample 1R at all pore pressure stages. The green curve shows the data before applying pore pressure.

Figure 5-19 illustrates the Fourier spectrum of the second Trattnach sample (2R), where the main frequencies show amplitude deflections and little to no frequency shifts can be seen.

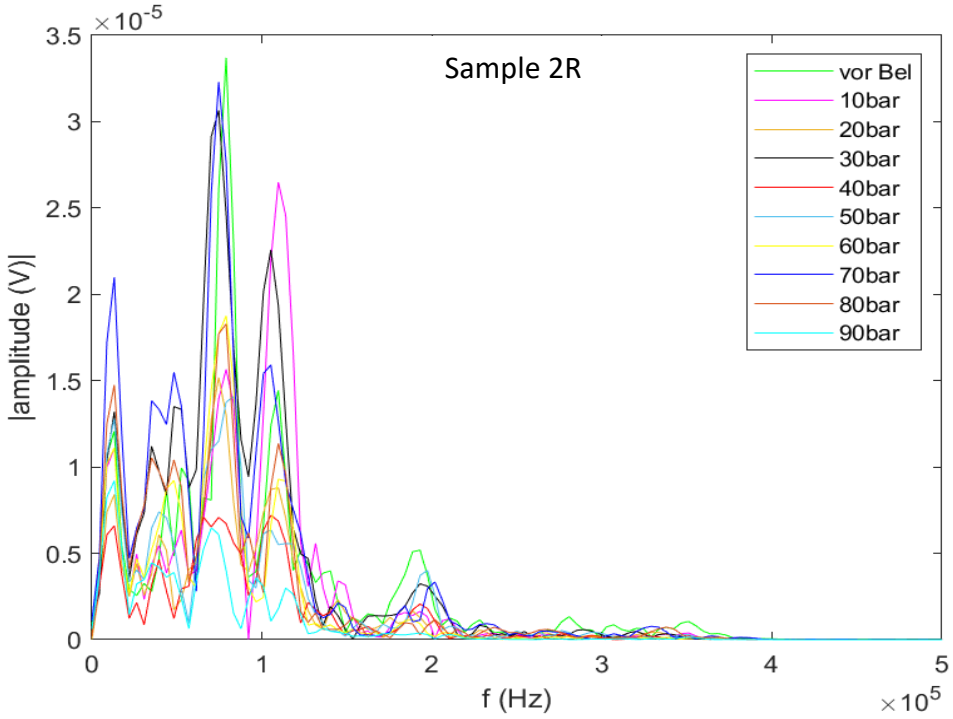

Figure 5-18: Fourier spectrum of sample 2R at all pore pressure stages. The green curve shows the data before applying pore pressure.

In Figure 5-19 the Fourier spectrum of sample DBA1 can be seen. The curves do not show any big changes through the different pore pressure loadings, except for amplitude deflections.

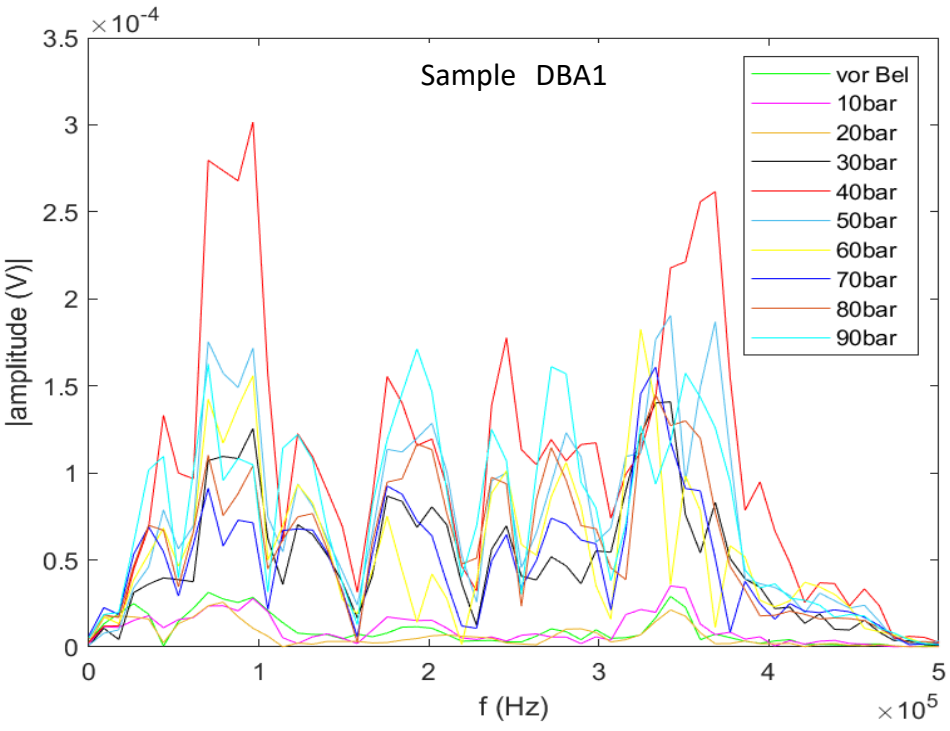

Figure 5-19: Fourier spectrum of sample DBA1 at all pore pressure stages. The green curve shows the data before applying pore pressure.

The Fourier spectrum of specimen DBA2 is depicted in Figure 5-20. In general, no big differences in frequency components between the pressure levels are visible, except for the 20 bar curve at about 300 000 Hertz.

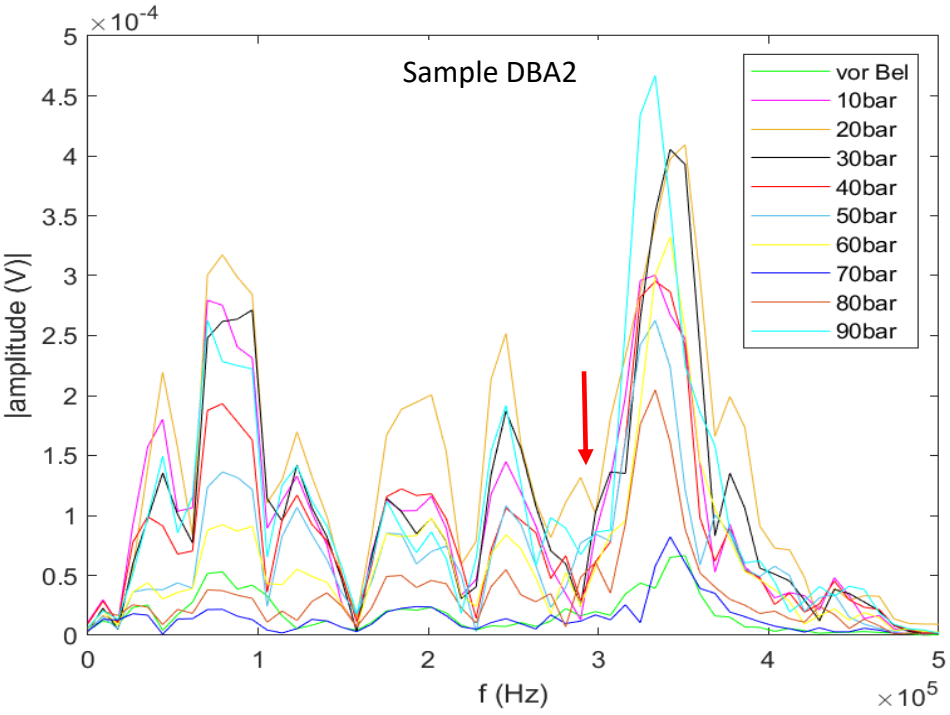

Figure 5-20: Fourier spectrum of sample DBA2 at all pore pressure stages. The green curve shows the data before applying pore pressure. The red arrow highlights some shifting.

In Figure 5-21 the Fourier spectra of sample DBA5 show an outlier at 20 bar, the rest of the curves are very similar, except a little difference at about 250 000 Hertz.

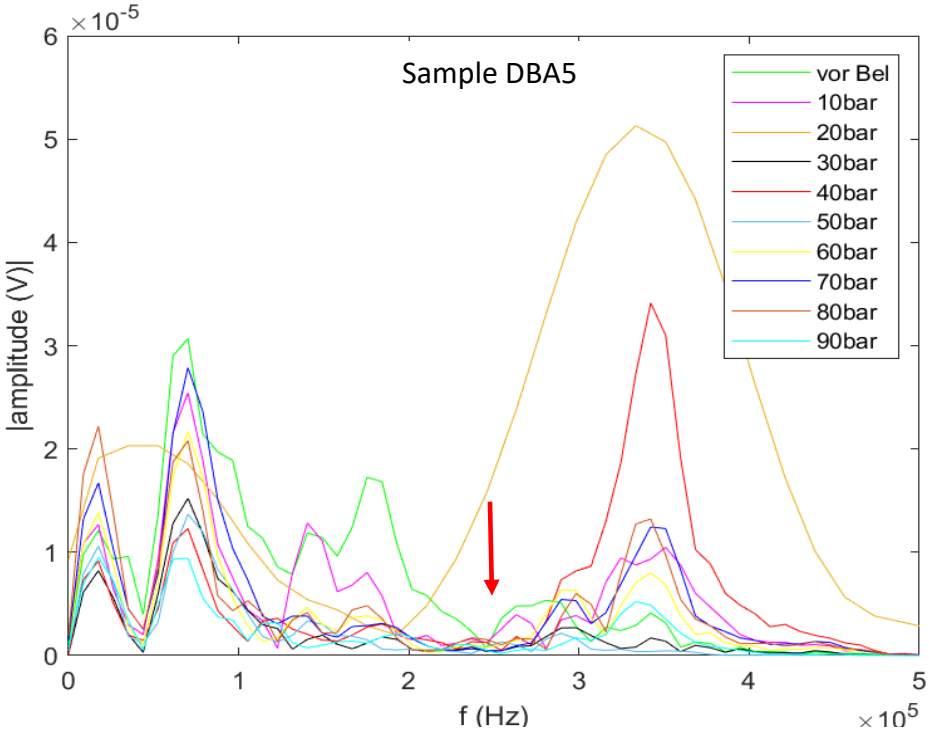

Figure 5-21: Fourier spectrum of sample DBA5 at all pore pressure stages. The green curve shows the data before applying pore pressure. The red arrow highlights some shifting.

Figure 5-22 depicts very solid frequency components where only at about 150 000 Hertz a deflection can be seen. Shown is the data of Sample DBA6.

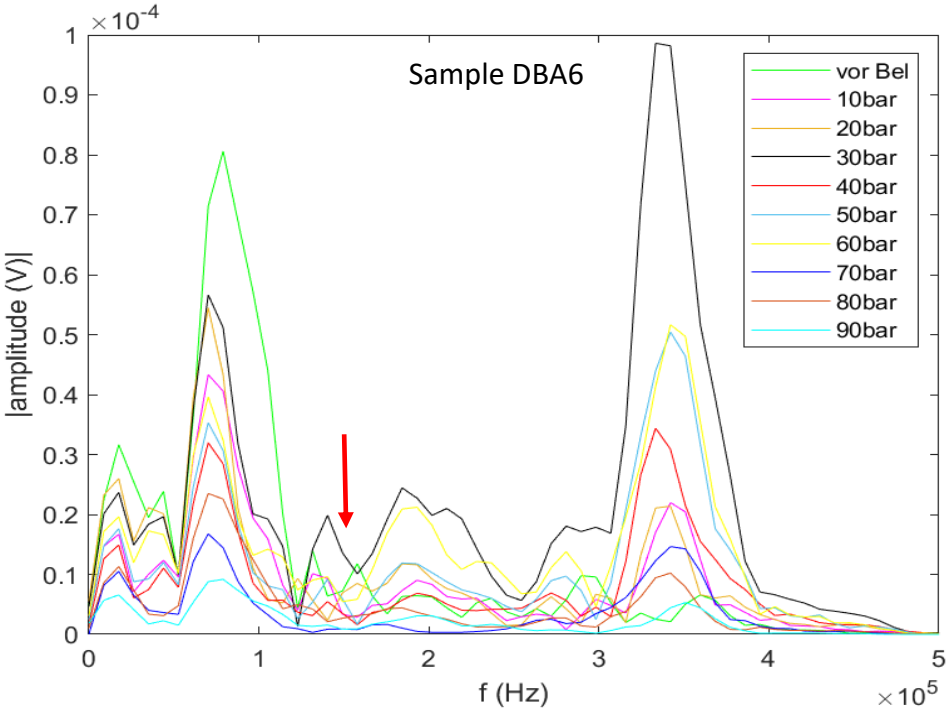

Figure 5-22: Fourier spectrum of sample DBA6 at all pore pressure stages. The green curve shows the data before applying pore pressure. The red arrow highlights some shifting.

Figure 5-23 illustrates the Fourier spectrum of the Exxon sample 4.1, where no major differences can be observed. The only exception might be at about 230 000 Hertz.

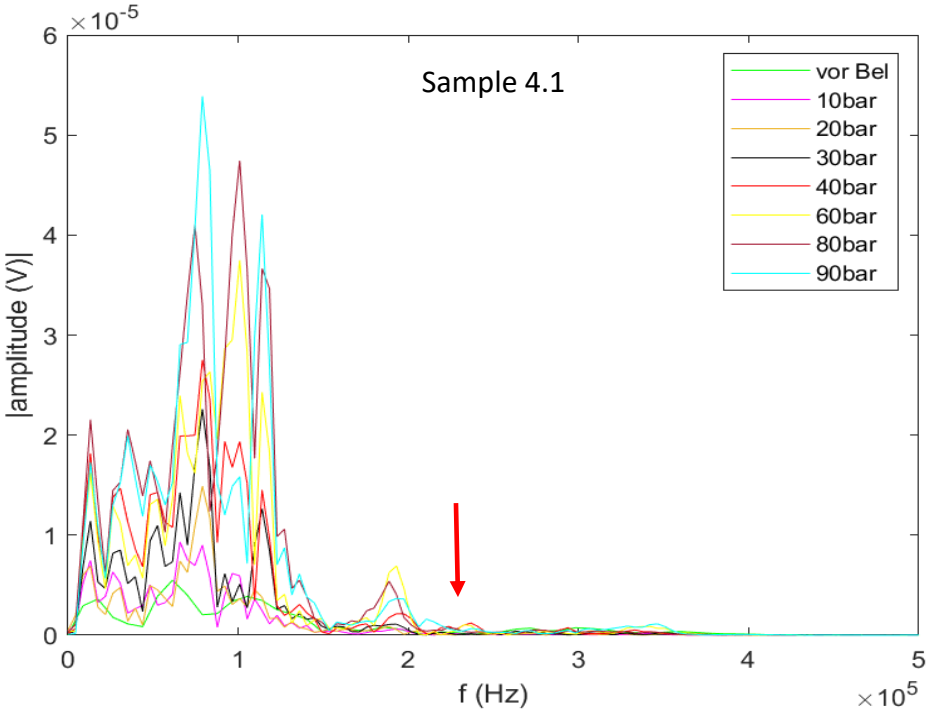

Figure 5-23: Fourier spectrum of sample 4.1 at all pore pressure stages. The green curve shows the data before applying pore pressure. The red arrow highlights some shifting.

The Fourier spectrum of specimen 4.2 is depicted in Figure 5-24. There are no major changes in frequency components visible.

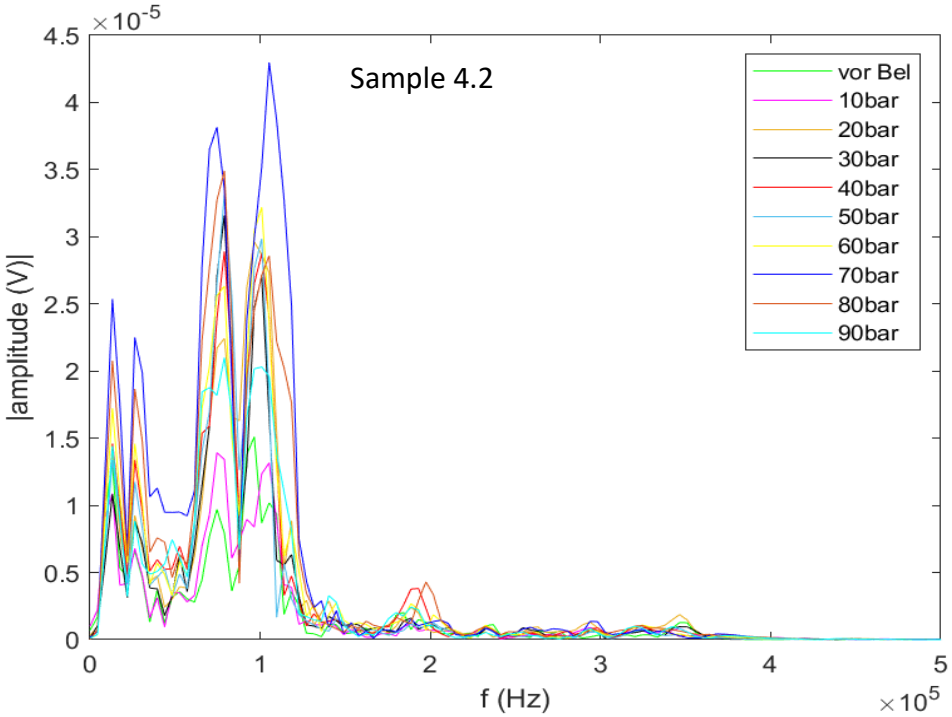

Figure 5-24: Fourier spectrum of sample 4.2 at all pore pressure stages. The green curve shows the data before applying pore pressure.

5.4.2 Experiment 2

In Figure 5-25 the Fourier spectra of the Trattnach specimens 1R and 2R are shown. In the left graph, no significant difference between the frequency spectra before and after applying pore pressure can be distinguished. In the right diagram a frequency component at about 200 000 Hertz is added after applying pore pressure compared to before.

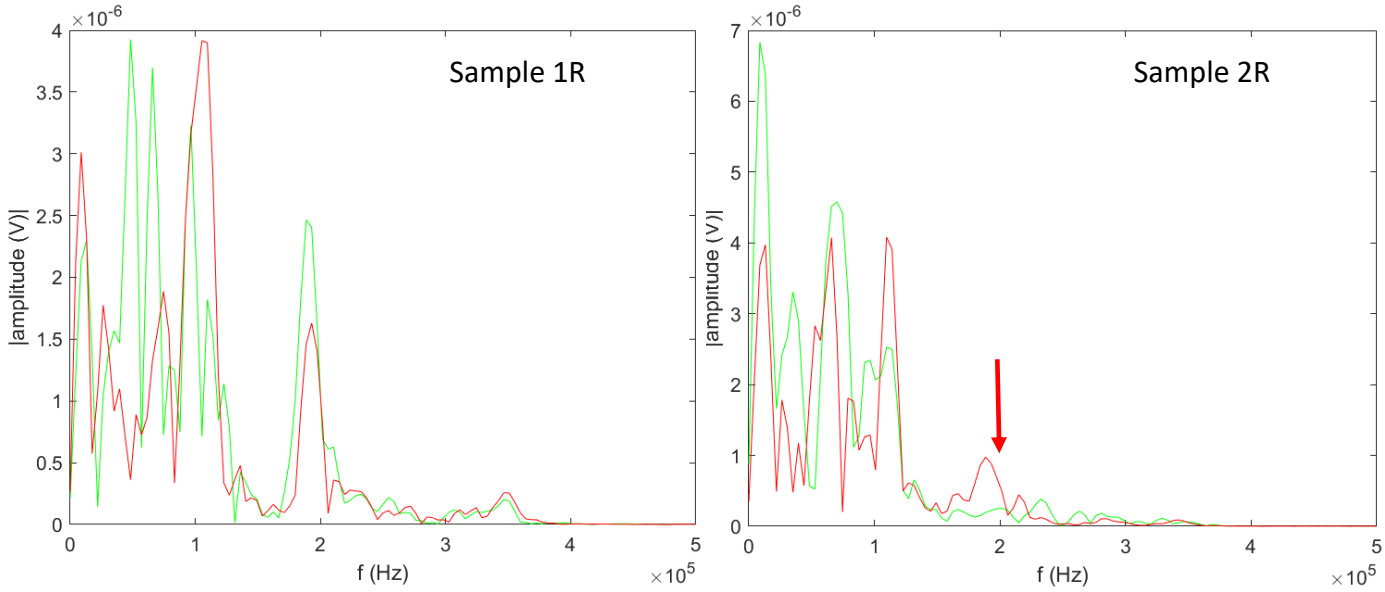

Figure 5-25: Fourier spectra of the Trattnach samples. On the left is sample 1R and on the right 2R. The green curve visualizes the measurement before applying pore pressure, while the red curve pictures the data after applying pore pressure. The red arrow highlights some shifting.

Figure 5-26 depicts the Fourier spectra of the Ruhr sandstone samples DBA1 and DBA2. The left graph shows some minimal shifts between before and after applying pore pressure. The right one shows different shaped curves, but the frequency components are not that different.

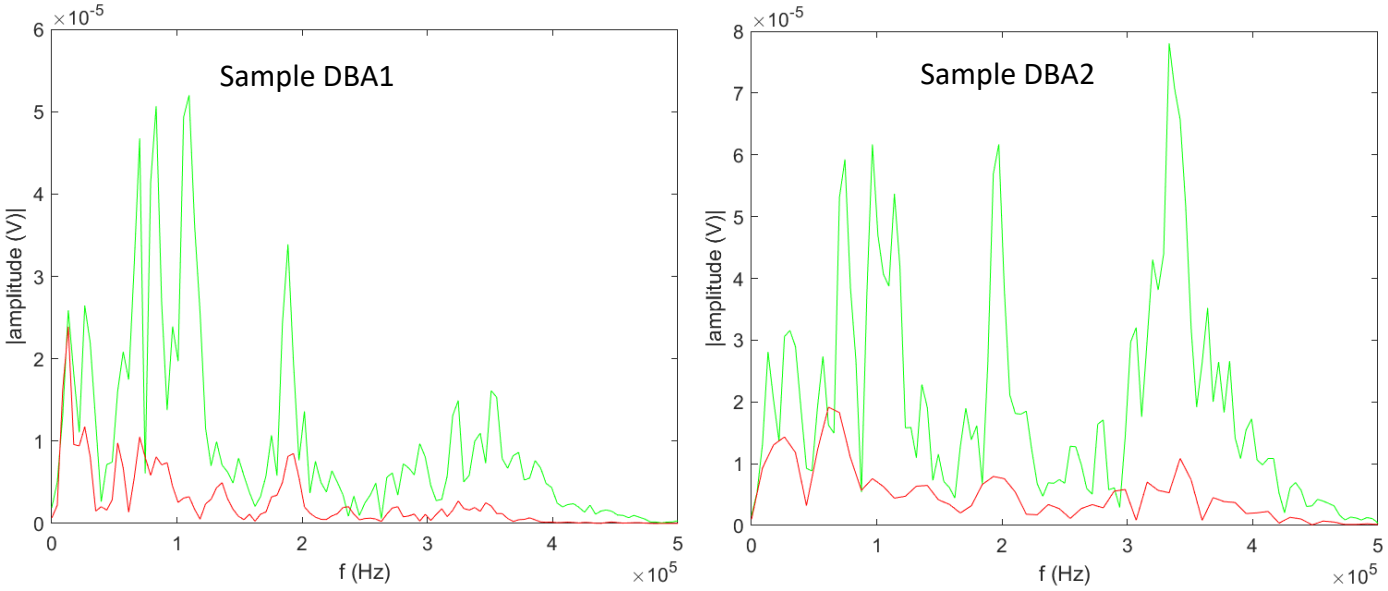

Figure 5-26: Fourier spectra of the Ruhr sandstone specimens. On the left, sample DBA1 is shown and on the right DBA2. The green curve visualizes the measurement before applying pore pressure, while the red curve pictures the data after applying pore pressure.

Figure 5-27 illustrates the Fourier spectra of DBA5 and DBA6. For specimen DBA5 there are no major shifts observed, as for DBA6, a difference at higher frequencies is noticeable.

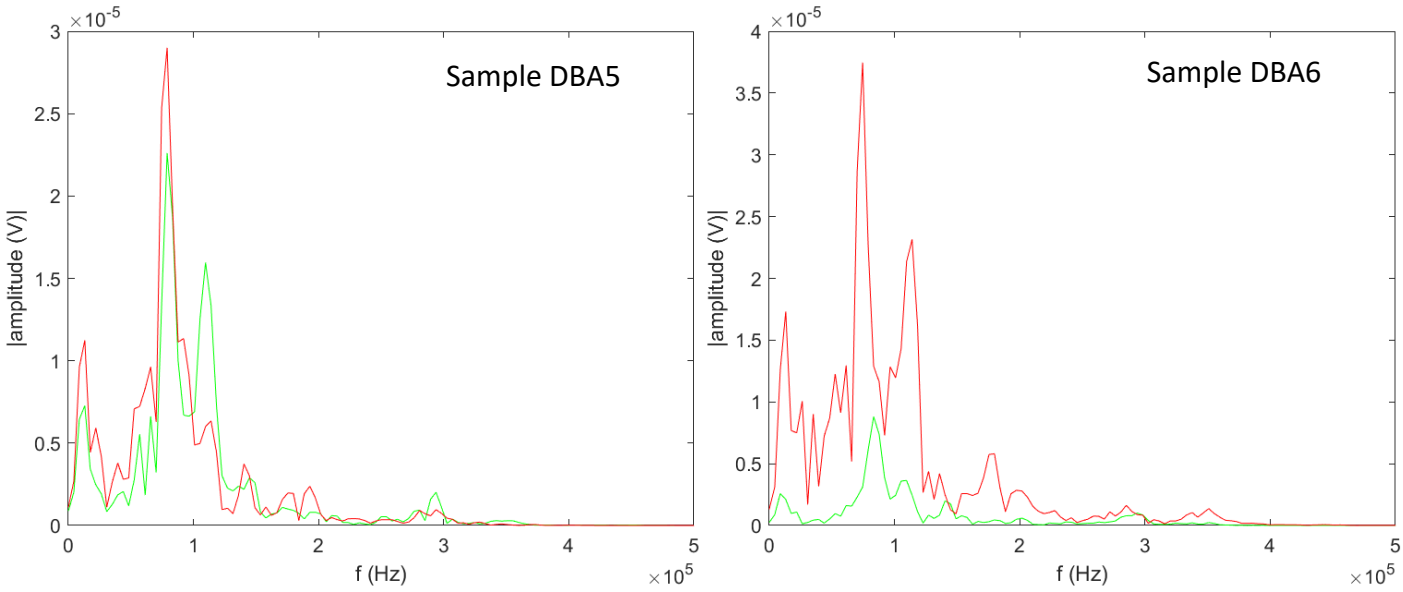

Figure 5-27: Fourier spectra of the Buntsandstein samples. On the left is sample DBA5 and on the right DBA6. The green curve visualizes the measurement before applying pore pressure, while the red curve pictures the data after applying pore pressure.

In Figure 5-28 the Fourier spectra of the Exxon samples 4.1 and 4.2 are pictured. For both samples, no major differences in frequency components are visible. Only for sample 4.2 at about 330 000 Hertz there might be a little deflection from before to after applying pore pressure.

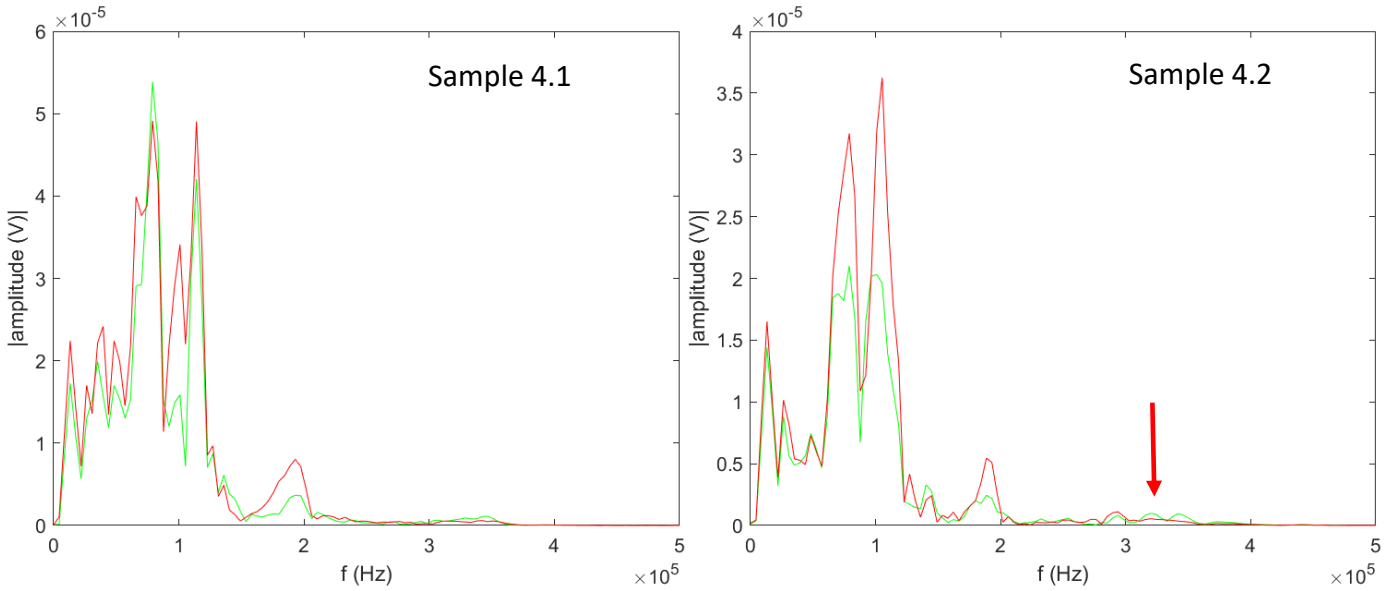

Figure 5-28: Fourier spectra of the Exxon sandstone specimens. On the left is sample 4.1 and on the right 4.2. The green curve visualizes the measurement before applying pore pressure, while the red curve pictures the data after applying pore pressure. The red arrow highlights some shifting.

6 Discussion

The calculations of the porosity (Table 5-1) of the samples all show a decrease except for the samples 1R and 2R. The increase can be explained by two observations. In Figure 6-1A, it is visible that material (most likely organic) is escaping from the specimens. The second reason is the clearly visible mechanical damage (Figure 6-1B) that the sample experiences during the experiments.

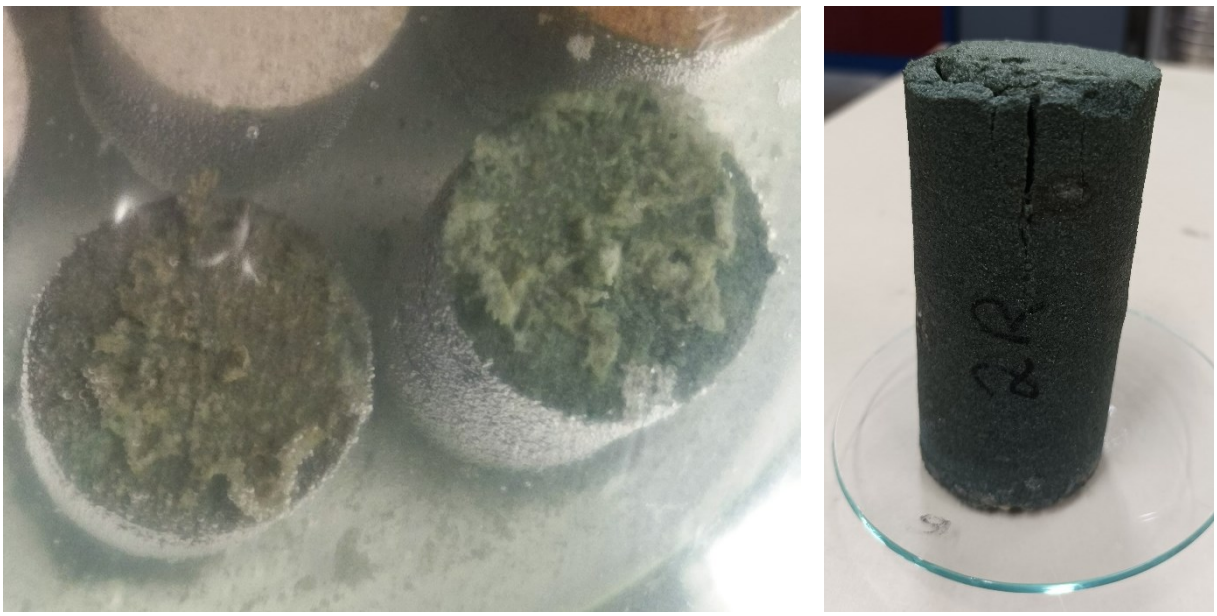

Figure 6-1: A: Organic material is extracted during the water saturation method. B: Visible mechanical damage of sample 2R after the experiments.

In relation, the porosity calculation based on the grain density provides significantly higher values (Table 5-2). This can be justified with the isolated pores. Helium moves more easily through the pore spaces due to its atomic size, whereas water is limited in this respect and only flows through the larger interconnected cavities.

Important for the calculation of the P-wave velocities is the first deviation from the straight line, meaning the arrival of the signal at the receiver. Therefore, the data sets were kept to a minimum to present the results more clearly. Figure 6-2 shows the data sets 0 bar, 10 bar, 40 bar, 70 bar and 90 bar of sample 1R. These were selected because the clearest differences can be seen.

The change in travel time from 0 bar to 10 bar can be explained by the initial loading by the Hoek cell and the rock testing press. A big difference can also be seen between 10 and 40 bar, suggesting mechanical damage to the sample. The slower velocity indicates damage to the rock matrix, as P-waves travel faster through solids than through gases or fluids. At 70 bar, damage is suspected again as the signal penetrates the rock sample faster. A rearrangement of the grains due to the applied pore pressure is probably the reason. Between 70 and 90 bar, no significant difference can be seen anymore, which allows the conclusion that no more major damage has been caused.

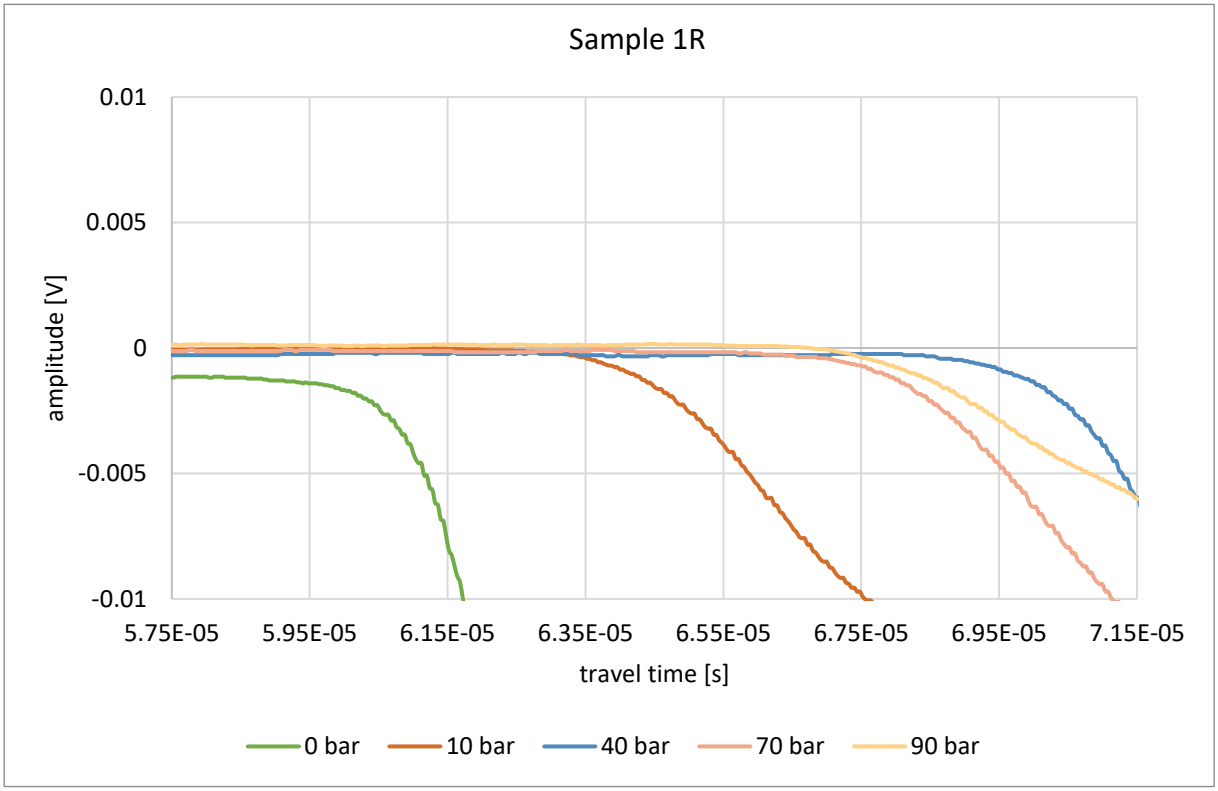

Figure 6-2: Detail of the travel time spectrum of sample 1R generated by the ultrasonic measurements. Only selected data sets are shown to illustrate the clearest differences. Significant differences are seen between 0, 10 and 40 bar.

The second Trattnach sample (2R) shows a less pronounced difference due to the Hoek cell loading (Figure 6-3). The clear difference between 10 and 40 bar can be seen as in sample 1R. The behaviour of the specimen at 70 and 90 bar respectively strongly follows the trend of the other Trattnach sample, the travel time decreases at 70 bar and slightly increases again at 90 bar. This suggests that samples from the same rock show similar trends in travel time during gas loading.

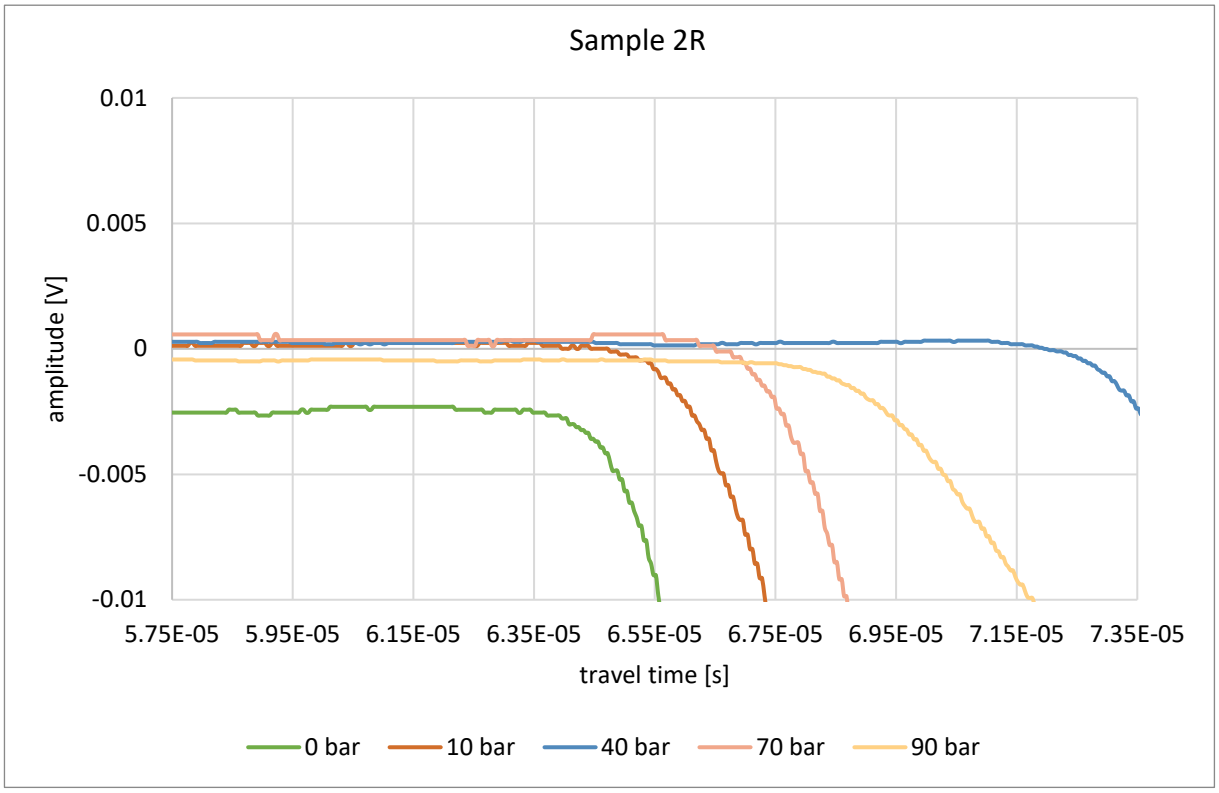

Figure 6-3: Detail of the travel time spectrum of sample 2R generated by the ultrasonic measurements. Only selected data sets are shown to illustrate the clearest differences. A significant increase can be seen from 10 to 40 bar, as well as a clear decrease from 40 to 70 bar.

Figure 6-4 compares the travel time curves of the two Trattnach samples. The left diagram shows the ultrasonic measurement before applying pore pressure, where a clearly slower travel time was measured for sample 2R. Across the individual pressure levels, such significant differences can no longer be seen, which is why only the graphs from 0 and 90 bar are shown. As can be seen in the diagram on the right, the trend of the travel time curve of the two samples is almost identical.

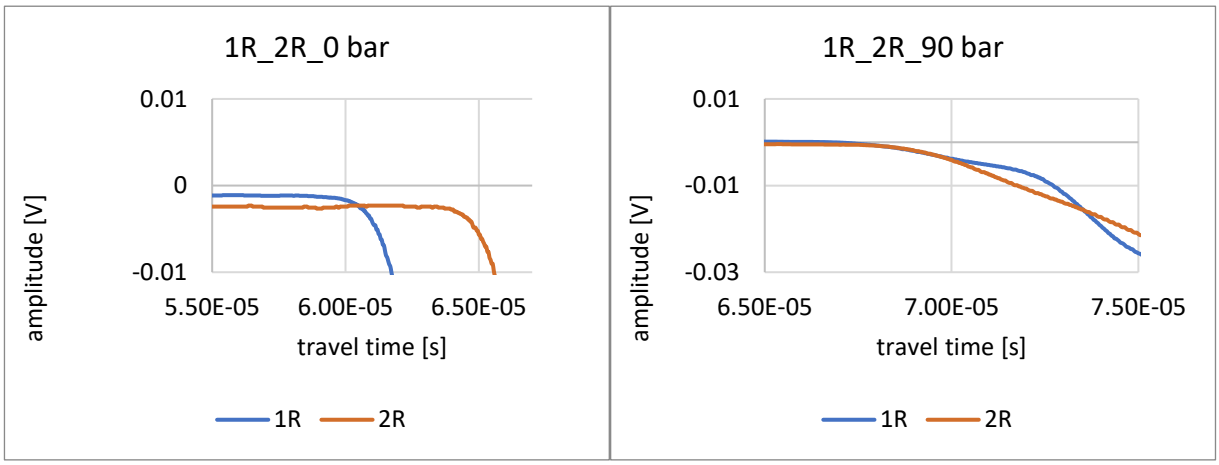

Figure 6-4: On the left side, the travel times of the Trattnach samples before applying pore pressure are shown. A significant difference can be recognized. On the right side, the travel time curves of the same specimens show an almost identical trend.

Figure 6-5 shows the travel time curves of the Ruhr sandstone for 0, 10, 40, 70 and 90 bar. As can be seen immediately, the travel times for 0, 10 and 40 bar are almost identical and a clear increase can be seen at 70 and 90 bar. This is due to the fact that during the tests the gas could only flow through the sample at a pore pressure of 70 bar or higher. Thus, a pore pressure of 70 bar creates sufficient mechanical damage that allows gas to flow through the sample. Detecting damage before 70 bar is not possible here, but it can only be a very small amount of damage, if any. Compared to the Trattnach samples before, no decrease in travel time can be seen. This can be explained by the more compact matrix of the Ruhr sandstone, which can be explained by the gas permeability from 70 bar. The data series for 50 and 60 bar have not been shown because there is no significant change compared to 40 bar, making the graph clearer.

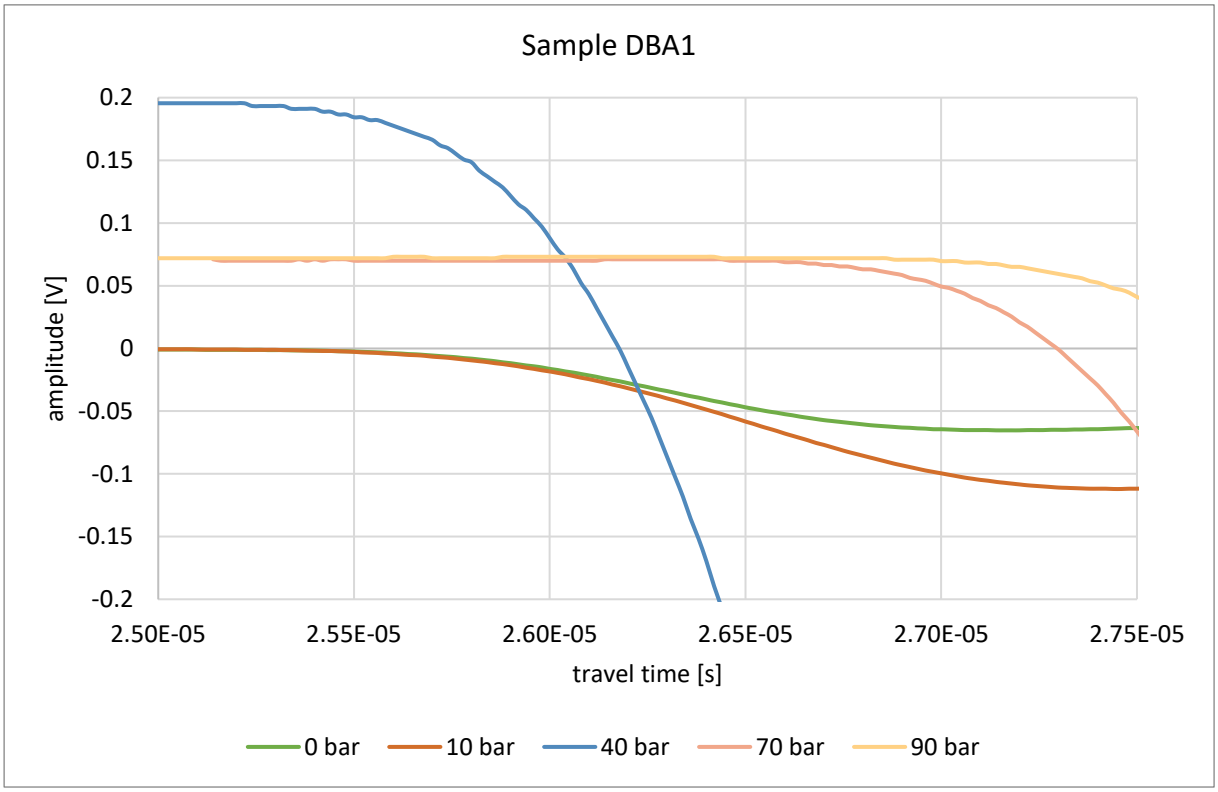

Figure 6-5: Detail of the travel time spectrum of sample DBA1 generated by the ultrasonic measurements. It is visible that the travel time jumps from 40 to 70 bar. Only 0, 10, 40, 70 and 90 bar are shown because of the clearance.

As with sample DBA1, an increase in travel time at 70 bar can be seen in Figure 6-6 for sample DBA2. For the pore pressures below this, no significant change can be observed either.

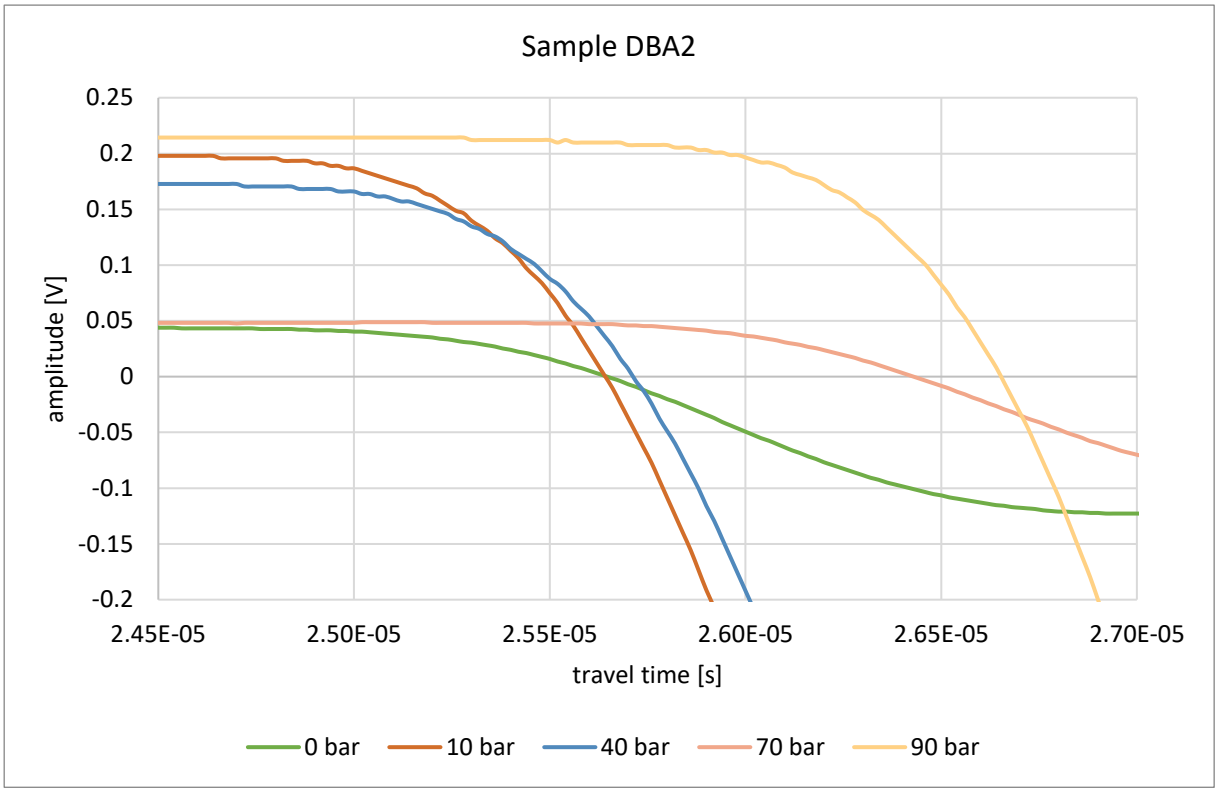

Figure 6-6: Detail of the travel time spectrum of sample DBA2 generated by the ultrasonic measurements. For a better overview of the diagram, only the following data series were shown: 0 bar, 10 bar, 40 bar, 70 bar and 90 bar. The travel times show a significant jump from 40 to 70 bar.

In Figure 6-7 the two Ruhr sandstone samples are compared. On the left side, the diagram shows the travel time at a pore pressure of 10 bar, where a slightly higher value for DBA1 is visible. The right graph pictures the data at 90 bar. These two pressures are chosen to visualize, that for all pressures stages it is nearly always the same picture. The DBA1 curve is slightly slower than the DBA2 curve.

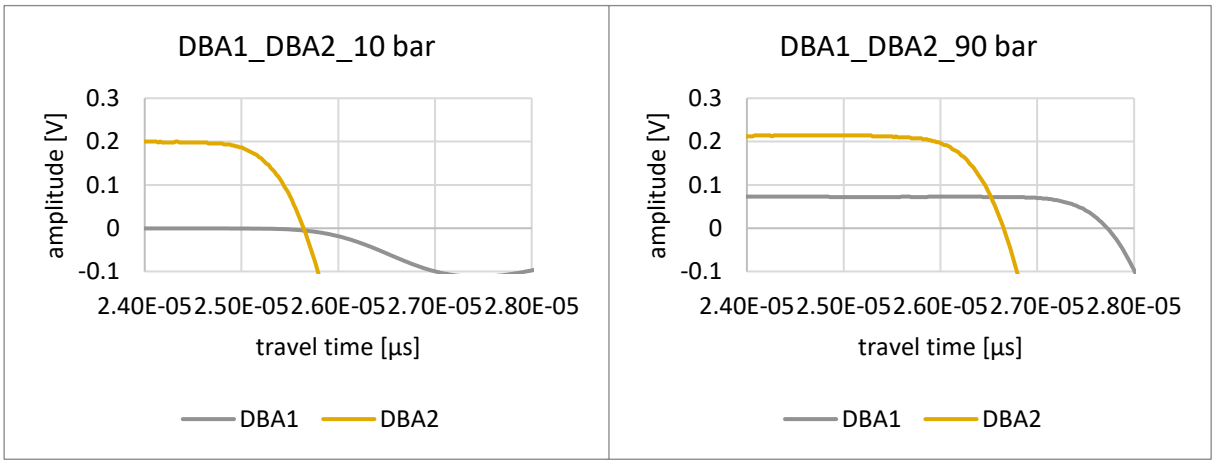

Figure 6-7: On the left side, the travel times of the Ruhr sandstone samples at 10 bar are shown. The right graph shows the travel times at 90 bar. It is visible, that DBA1 shows a slightly higher travel time than DBA2.

Figure 6-8 shows the travel time curves of sample DBA5. The influence of the Hoek cell is very small in contrast to the Trattnach samples (1R, 2R). A first meaningful increase can be seen from 40 to 70 bar, a second from 70 to 90 bar. The data series in between do not show significant differences to the respective previous pore pressures and are therefore not shown in the diagram. Thus, for this Buntsandstein sample, it can be stated that the clearest mechanical damage occurs at 70 and 90 bar pore pressure. At the lower pressures, little to no damage can be identified from the ultrasonic measurements.

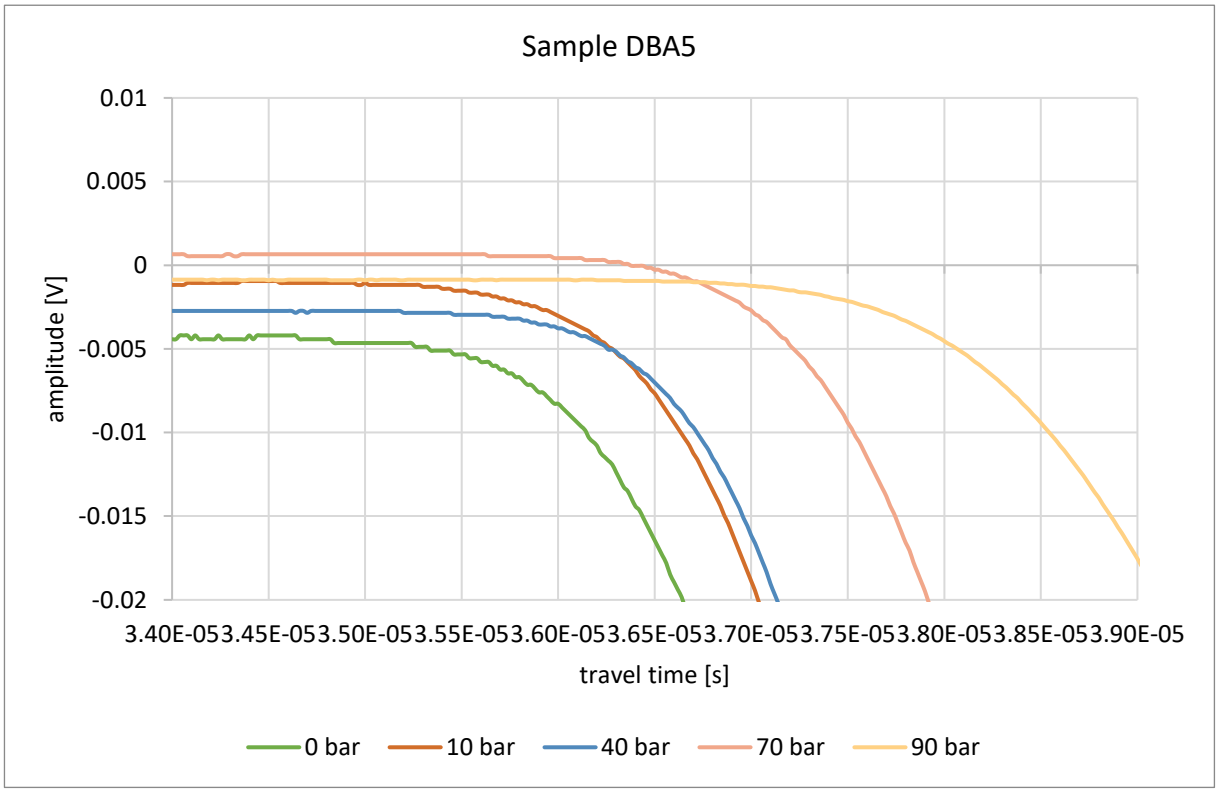

Figure 6-8: Detail of the travel time spectrum of sample DBA5 generated by the ultrasonic measurements. Only selected data series are shown, which have the most significance. A clear increase from 40 to 70 bar can be seen.

Compared to the Buntsandstein specimen before, sample DBA6 shows a greater influence of the Hoek cell. This suggests a stronger deformation or grain rearrangement due to the initial triaxial loading. The travel time continues to increase with increasing pressure as can be seen in Figure 6-9. The travel time curves of 20 and 30 bar show hardly any difference to 10 bar, those of 50 and 60 bar to 40 bar and that curve at 80 bar pore pressure is very similar to the curve of 70 bar. Due to this, only data series with the clearest differences are presented. The greatest increase in travel time is seen from 40 to 70 bar, which is why the greatest mechanical damage occurs when the pore pressure rises to 70 bar.

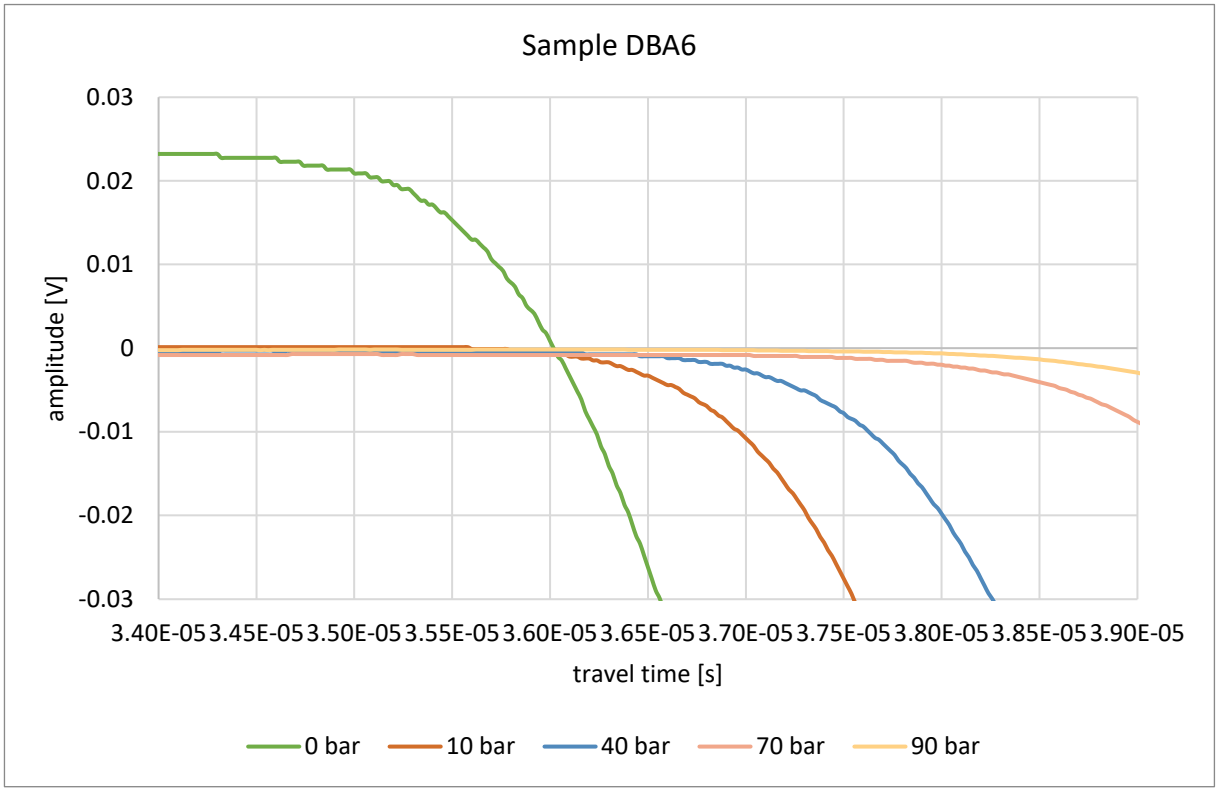

Figure 6-9: Detail of the travel time spectrum of sample DBA6 generated by the ultrasonic measurements. Travel times show a continuous increase from 0 to 90 bar. For a better overview of the diagram, only the following data series were shown: 0 bar, 10 bar, 40 bar, 70 bar and 90 bar.

Figure 6-10 compares the travel time curves of the two Buntsandsteins. Across all pressure levels, the travel time of sample DBA5 is lower than that of DBA6. For illustration purposes, the curves of 10 and 90 bar have been plotted, with the difference between the travel times of the samples increasing with increasing pore pressure. The higher travel time of DBA6 suggests that grain rearrangement in this sample creates larger or multiple pore spaces which are known to conduct P-waves less well than solid phases.

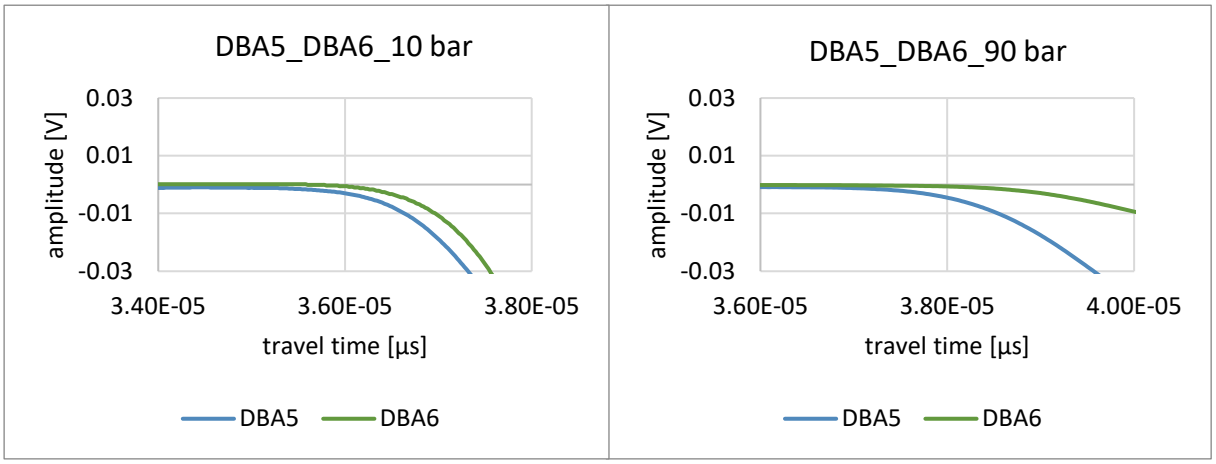

Figure 6-10: On the left side, the travel times of the Buntsandstein samples at 10 bar are shown. The right graph shows the travel times at 90 bar. It is visible, that DBA6 shows a slightly higher travel time than DBA5. This can be observed across all pressure levels.

Exxon sample 4.1, like the Trattnach samples, shows a large influence of the Hoek cell, justified by the jump in the travel time from 0 to 10 bar. Thereafter, there is no significant change with increasing pressure, as can be seen in Figure 6-11. This shows that the main damage was generated by the Hoek cell up to 70 bar. From 10 to 70 bar, slight changes in travel time can be seen due to grain rearrangements. At 90 bar, there is an increase in travel time associated with mechanical damage that is not due to the Hoek cell.

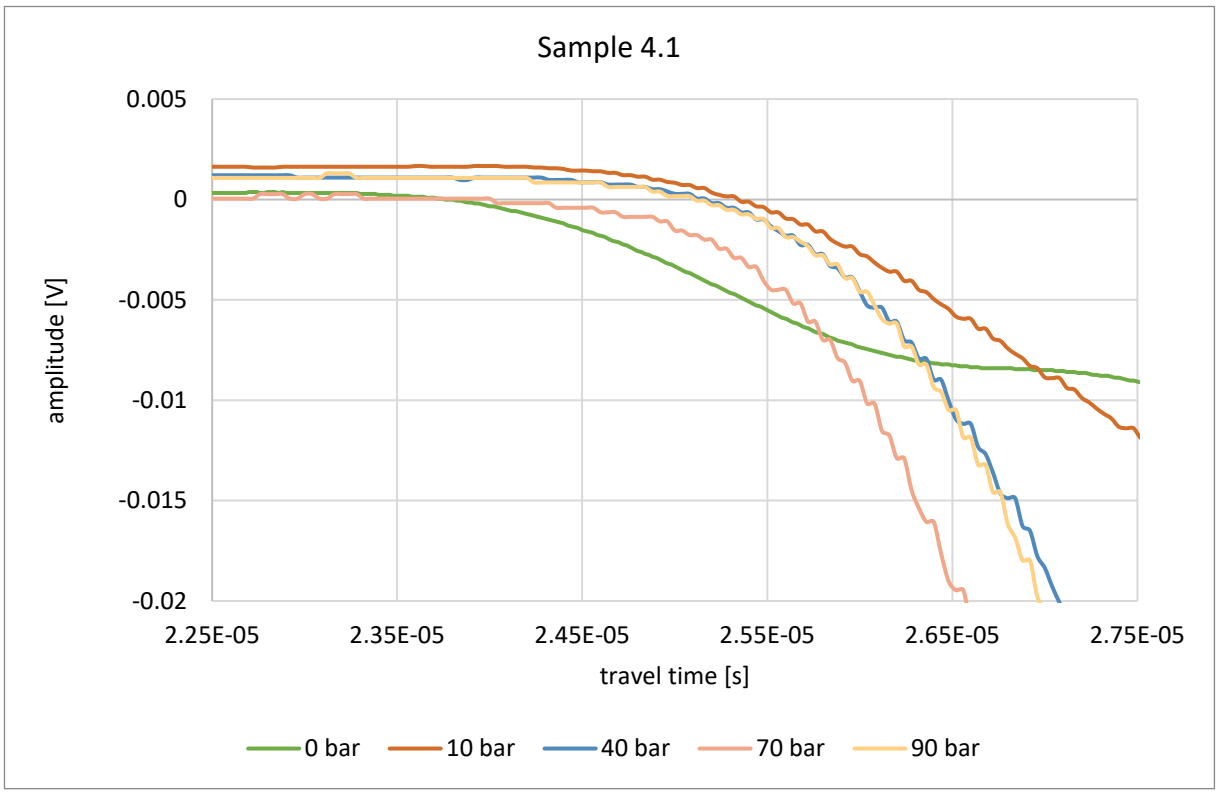

Figure 6-11: Detail of the travel time spectrum of sample 4.1 generated by the ultrasonic measurements. After a clear increase from 0 to 10 bar, the travel times show no significant changes until a drop at 70 bar, followed by an increase at 90 bar. Only selected data series are shown, which have the most significance.

For sample 4.2 there are no changes in travel time due to the Hoek cell, so the curves of 0 and 10 bar are very similar. A major difference can be seen from 10 to 40 bar, which is related to the occurrence of mechanical damage. Figure 6-12 pictures the travel time curves of the second Exxon sample. Compared to the specimen 4.1, this sample does not show a significant decrease at 70 bar, which might be explained because of the general higher porosity leading to slower P-wave velocities.

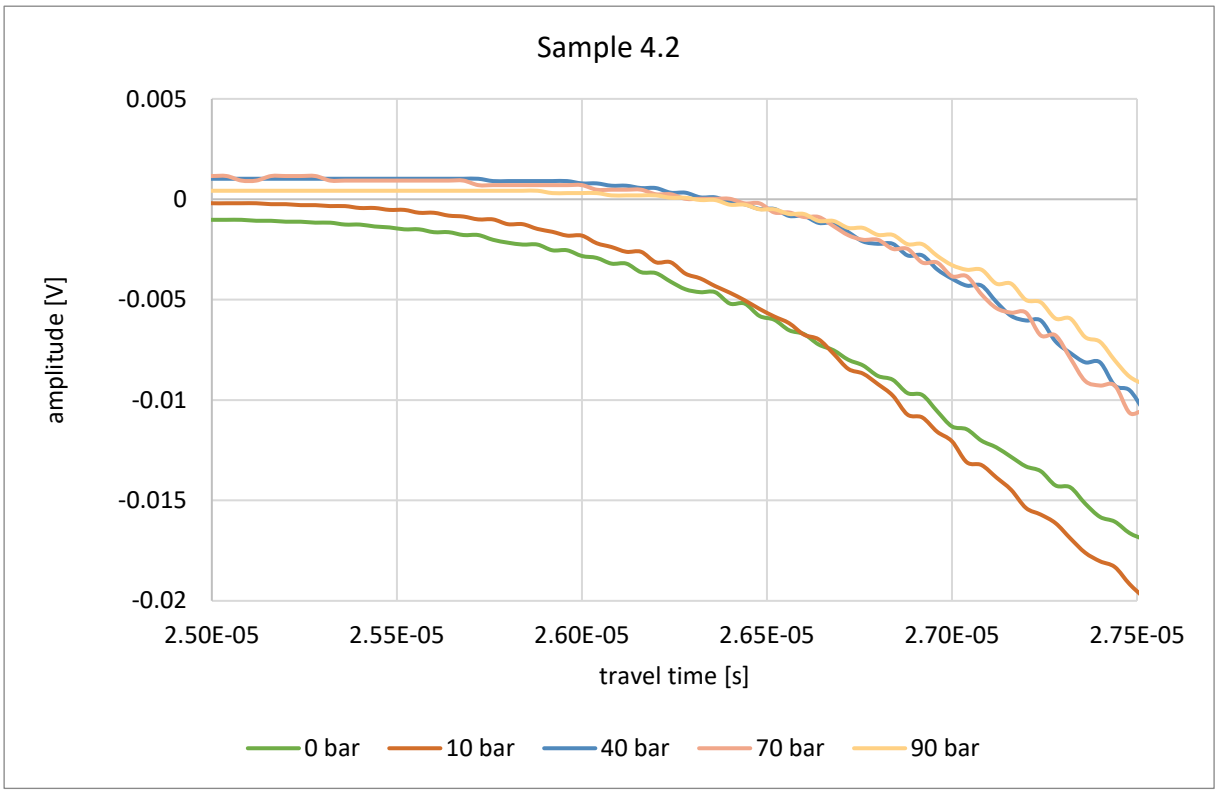

Figure 6-12: Detail of the travel time spectrum of sample 4.2 generated by the ultrasonic measurements. For a better overview, only selected data series are shown. A significant change in travel times can only be seen between 10 and 40 bar.

In Figure 6-13 the two Exxon sandstones are compared. On the left graph, the travel time curves at 10 bar are shown, where it can be seen that the sample 4.2 provides a higher value than 4.1. This trend can be followed across all pressure levels. As it is the final pressure level, on the right diagram the 90 bar curve is pictured. The higher values of the travel time for sample 4.2 correlate very well with the higher porosity calculated before (Table 5-2).

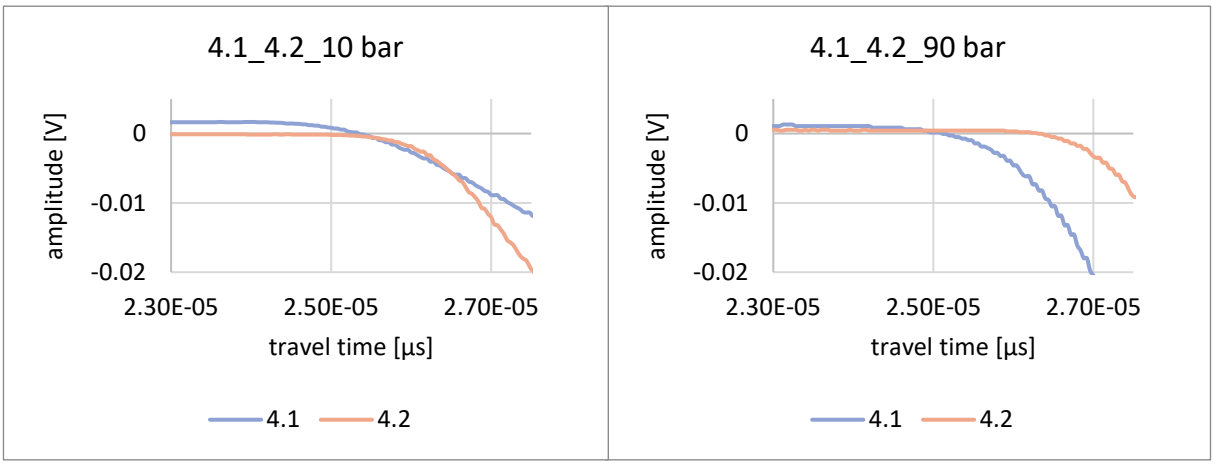

Figure 6-13: On the left diagram, the travel time curves of the Exxon samples are shown at a pore pressure of 10 bar. The right graph pictures the curves at 90 bar gas pressure. It can be observed that sample 4.2 shows higher travel times than 4.1.

In Figure 6-14 the relation between the calculated porosity and the P-wave velocity is shown. The values for the P-wave are calculated before applying any pore pressure and after the cyclic pore pressure loading. The reason why is because the water saturation was done on the one hand before applying pore pressure and on the other hand after all experiments. It is visible that samples of the same rock type follow a nearly identical trend. All of the specimens show a decrease in P-wave velocity, some bigger, some smaller. Interestingly, the Trattnach specimens show an increase of porosity after applying pore pressure, while the other samples show a decrease. The increase is due to the extraction of organic material as seen before in Figure 6-1A. The decrease of the velocities shows that there was definitely damage induced to the samples during the experiments. The reason for this is the fact that P-waves propagate faster through solid phases than through gaseous (or liquid) phases.

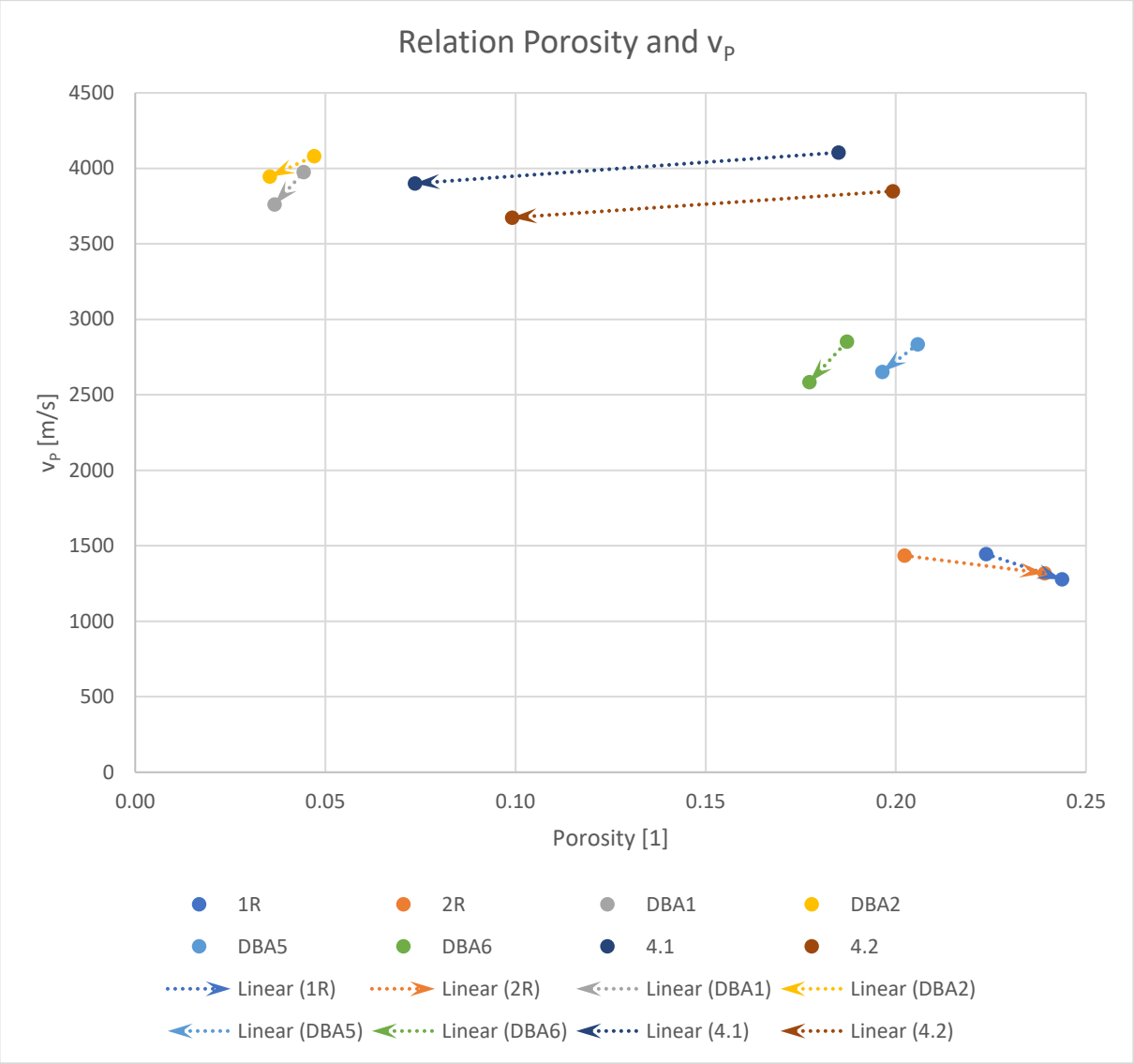

Figure 6-14: Relation between the calculated porosity (water saturation method) and the determined P-wave velocities (MatLab). The dashed lines reflect the trend direction. The arrowhead points to the value after the experiments; the other point provides the data before applying any pore pressure.

In Figure 6-15 the zoomed in results of the injection and extraction experiment are shown. In most of the diagrams there is not much change in the travel times. A reason for that may be, that pore pressure loading of the samples does some damage, but the unloading gives the grains a chance to relax, so it might be that the grains move back to their original position or at least close to that. This could be the case for the specimens 2R, DBA1, DBA2, DBA6, 4.1 and 4.2. The travel time curve of sample 1R shows a decrease, while the sample DBA5 shows an increase. Due to the fact that no significant change can be detected in most of the specimens, samples 1R and DBA5 are to be interpreted as outliers.

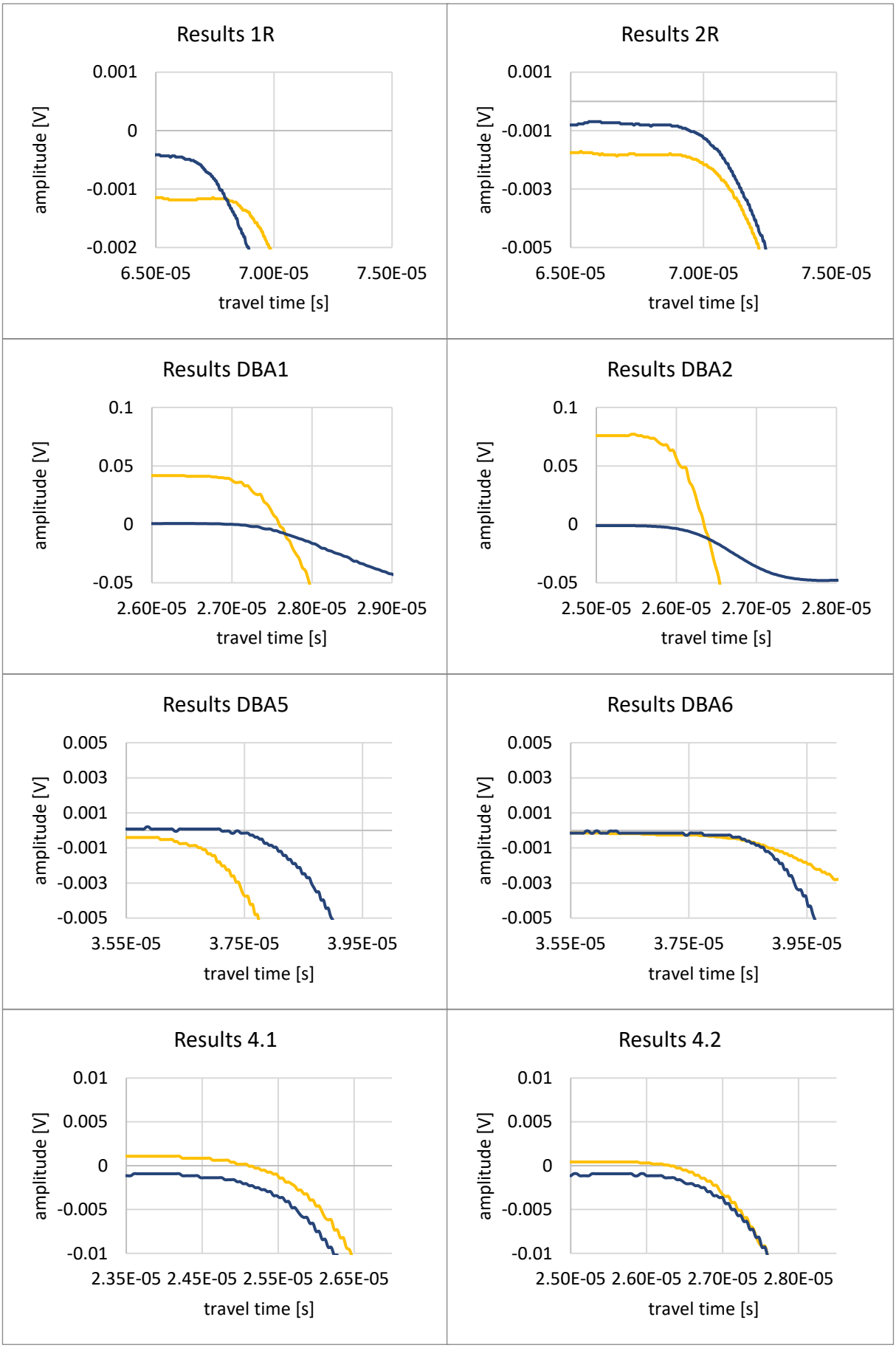

Figure 6-15: Travel time curves are shown for all samples of the injection and extraction experiment. The yellow line shows the data before applying pore pressure and the blue curve represents the data after applying pore pressure.

The interpretation of Fourier spectra is very complex. Therefore, in the present work, an evaluation of these spectra alone is not possible. Fourier analysis serves here as a supplement and confirmation to the previously interpreted data. That is why the same pore pressure curves are shown in the following diagrams as already for the travel time. The pressure levels not shown can be looked up in chapter 5.4.1 if one is interested. Nevertheless, these do not provide any new information. It should be noted that the amplitude deflections in some diagrams appear extremely prominent. However, the high number of influencing factors does not offer the possibility to include the amplitude representatively in the interpretation. This is why the main focus is on the shifts of the frequency components, as well as the appearance or disappearance of just those. From this, it can be concluded whether damage is occurring and, if so, whether it is major or minor damage. Major damage is to be assumed in the case of a change in the lower frequency range, while minor damage is visible in the higher frequency range (Melhem & Kim, 2003). The influence of the Hoek cell from before applying pore pressure to 10 bar must also always be considered. A quantitative statement about the extent of the damage is not possible here.

In the Fourier spectra of the Trattnach sample 1R, which is depicted in Figure 6-16, some small shifts between the pore pressure curve at 0 bar and all other pressure level curves. At a frequency of about 350 000 Hertz, a peak of the green line (before applying pore pressure) is visible. Some Hertz before, the red line (40 bar) shows a peak itself, indicating a shift. As this change is at a quite high frequency, small damage can be interpreted from before applying pore pressure to 40 bar. This observation correlates very well with the gathered information of the travel time curve (Figure 6-2).

At about 200 000 Hertz, there are some shifts visible, which reflect the damage through the different pressure levels. A shift to the right from 10 to 40 bar and from 40 to 70 can be detected. From 70 to 90 bar, the movement is to the left. Such shifts can also be tracked in the low-frequency range.

From the direction of the displacement, no correlation with the p-wave velocity can be interpreted. However, the change in the frequency components confirms that damage to the specimen has occurred between the respective pressure levels.

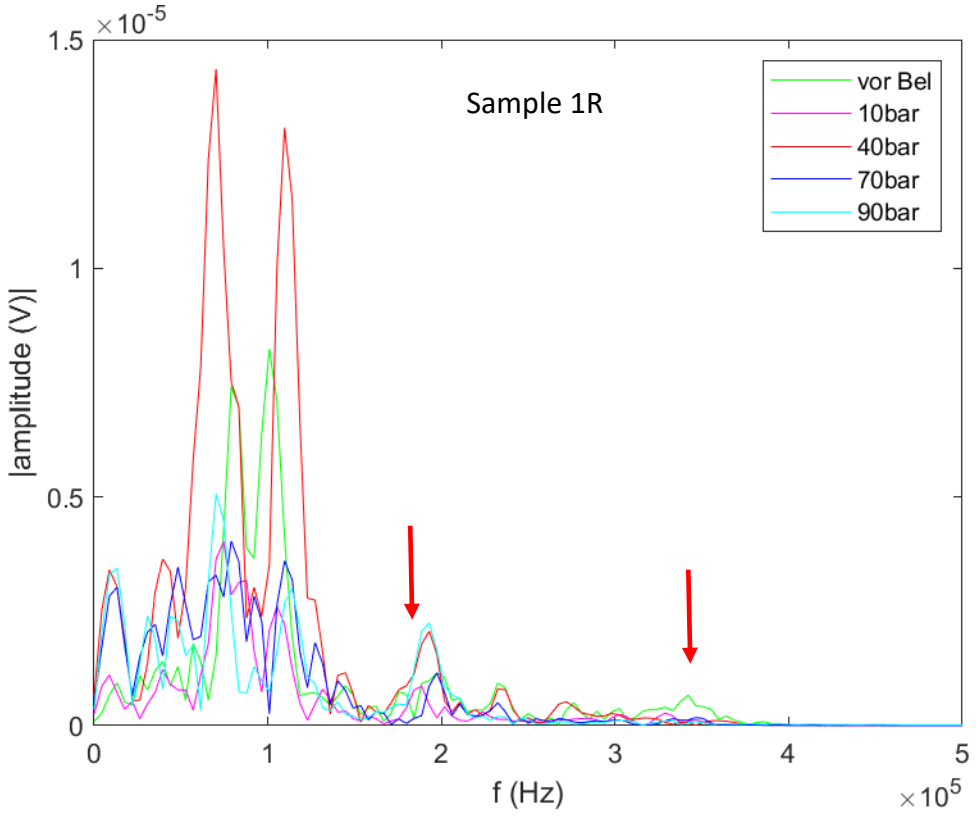

Figure 6-16: For a better overview, only the spectra of 10, 40, 70, 90 bar and before the applying pore pressure (green) are shown. Small shifts from before applying pore pressure to the higher pore pressure levels are visible. The red arrows highlight some shifting.

In Figure 6-17 the Fourier spectra of the second Trattnach sample, 2R, show a similar behaviour as 1R. At about 200 000 Hertz, a clear shift of the 70 bar curve, which indicates damage, is visible. On closer inspection, a disappearance of the frequency component in the 90 bar curve can be observed in this range. This also indicates damage. In the small frequency range at about 30 000 Hertz, a shift from 40 to 70 bar, as well as from 70 to 90 bar can be seen. So, there are, as in sample 1R, also movements in the higher and lower frequency range, which suggests some bigger and some smaller damage.

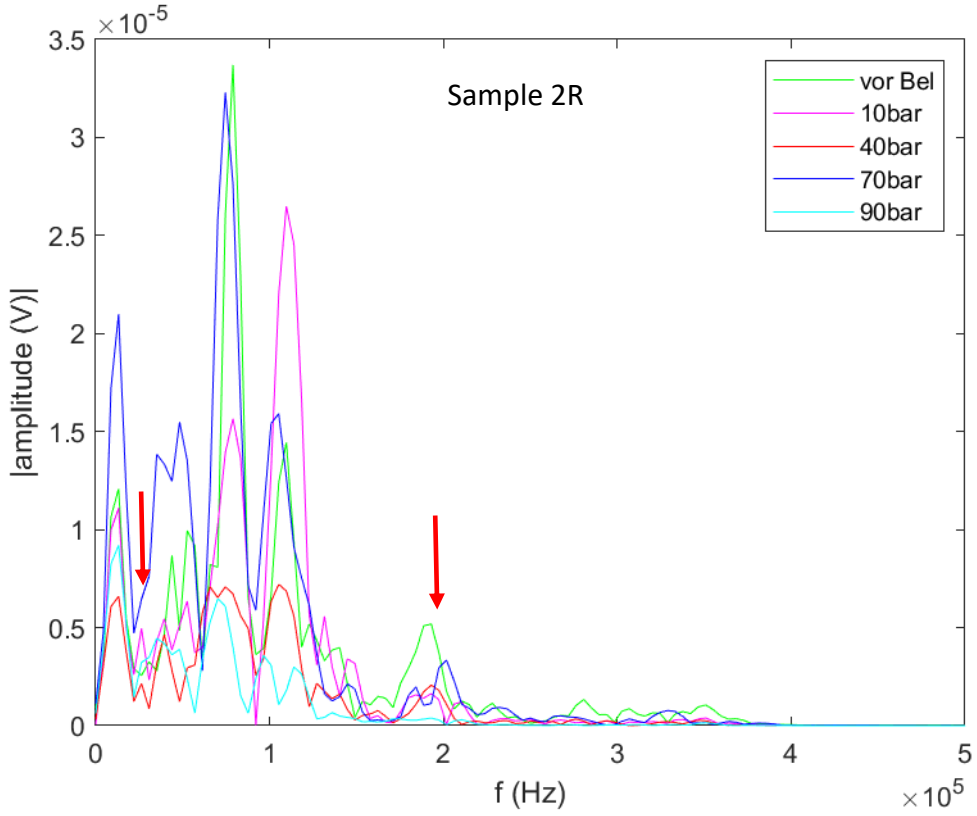

Figure 6-17: For a better overview, only the following data are shown: before applying pore pressure (green), 10, 40, 70 and 90 bar. Small shifts from before applying pore pressure to the higher pore pressure levels are visible. The red arrows highlight some shifting.

Figure 6-18 illustrates the Fourier spectra of sample DBA1. At about 180 000 Hertz, nearly all pressure levels show the same frequency component, except for the 90 bar curve. A shift is clearly visible, which indicates damage from 70 to 90 bar. Through the whole spectra, the 90 bar data is mostly a little bit shifted compared to the other curves. At about 320 000 Hertz, a shift of the 70 bar as well as the 90 bar data can be observed. This suggests that some small damage occurred at the 70 bar level.

As the gas did not flow through the sample until 70 bar, the behaviour of the frequency components confirm, that there is the main damage occurs starting at 70 bar. It would be possible that damage also occurred at lower pressures, but this can not be observed in Figure 6-5 or in the frequency spectra of sample DBA1.

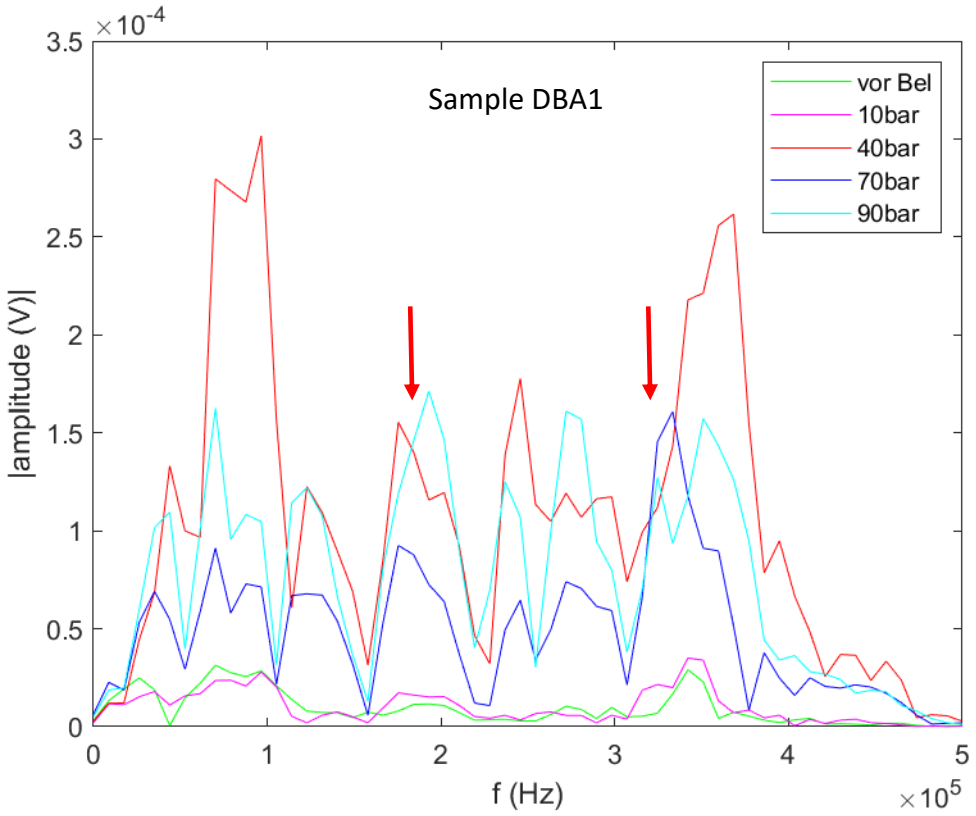

Figure 6-18: Only data of before applying pore pressure, 10, 40, 70 and 90 bar are shown for a better overview. At about 320 000 Hertz a major shift of the 70 bar curve can be recognized and at about 180 000 Hertz a shift of the 90 bar curve. The red arrows highlight some shifting.

As for the Imberg sample above, the DBA2 Fourier spectra (Figure 6-19) do not show very big shifts, especially at the lower pressure levels. At about 30 000 Hertz, the 90 bar curve is shifted from the curves before applying pore pressure, 40 and 70 bar. Interestingly, the 10 bar curve shows the same frequency component as the 90 bar. This could mean that damage was induced by the influence of the Hoek cell, as well as that when the pressure increased to 40 bar, damage was induced again, resulting in a new displacement. No change in the travel time curve (Figure 6-6) up to 70 bar and gas flow through the sample from 70 bar onwards do not indicate this.

Through the spectra it is visible, that there is a shift between 40 and 70 bar and one between 70 and 90 bar. It can be concluded that the sample was clearly damaged at 70 and 90 bar.

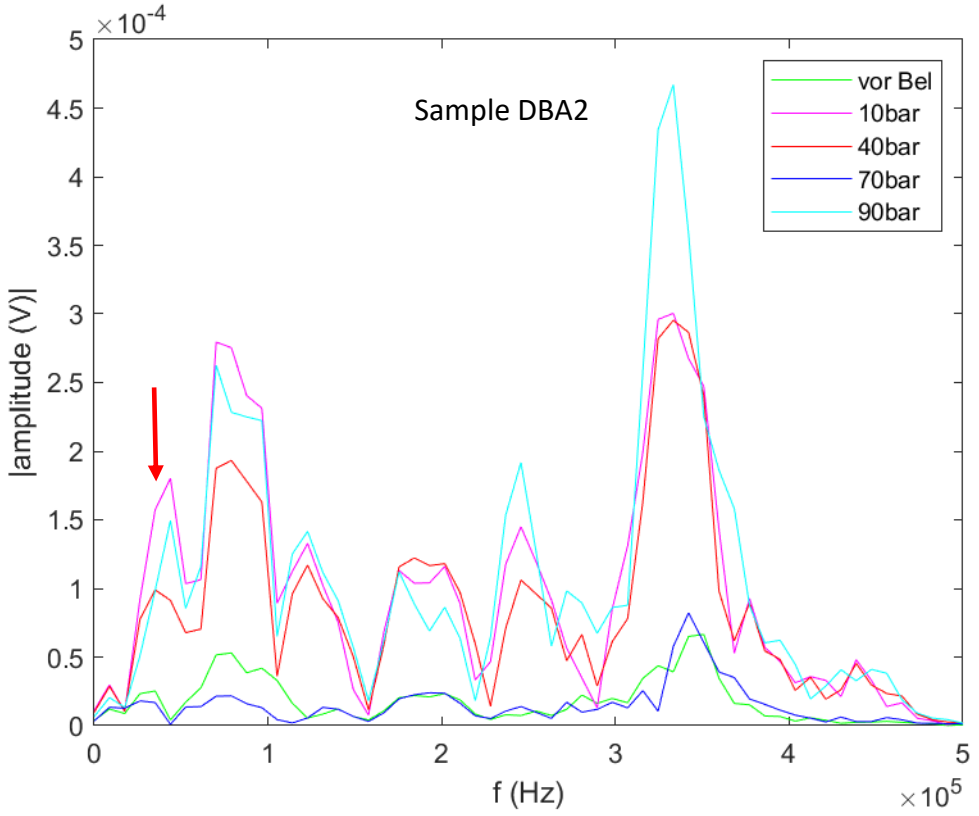

Figure 6-19: For a better overview, just the following curves are pictured: before applying pore pressure, 10, 40, 70 and 90 bar. Some small frequency component changes can be observed. The red arrow highlights some shifting.

In Figure 6-20 the Fourier spectra of the Buntsandstein sample DBA5 are shown. At about 120 000 Hertz, some shifting from 10 to 40, 40 to 70 and 70 to 90 bar can be observed. The sample is therefore damaged at each of these levels. The higher frequency components follow this behaviour. For the low frequencies, there is nearly no shifting. The only exception is the effect of the Hoek cell, which occurs in small shifts from before applying pore pressure to 10 bar. The changes seen in the Fourier spectra correlate very well with the seen changes in the travel time curves.

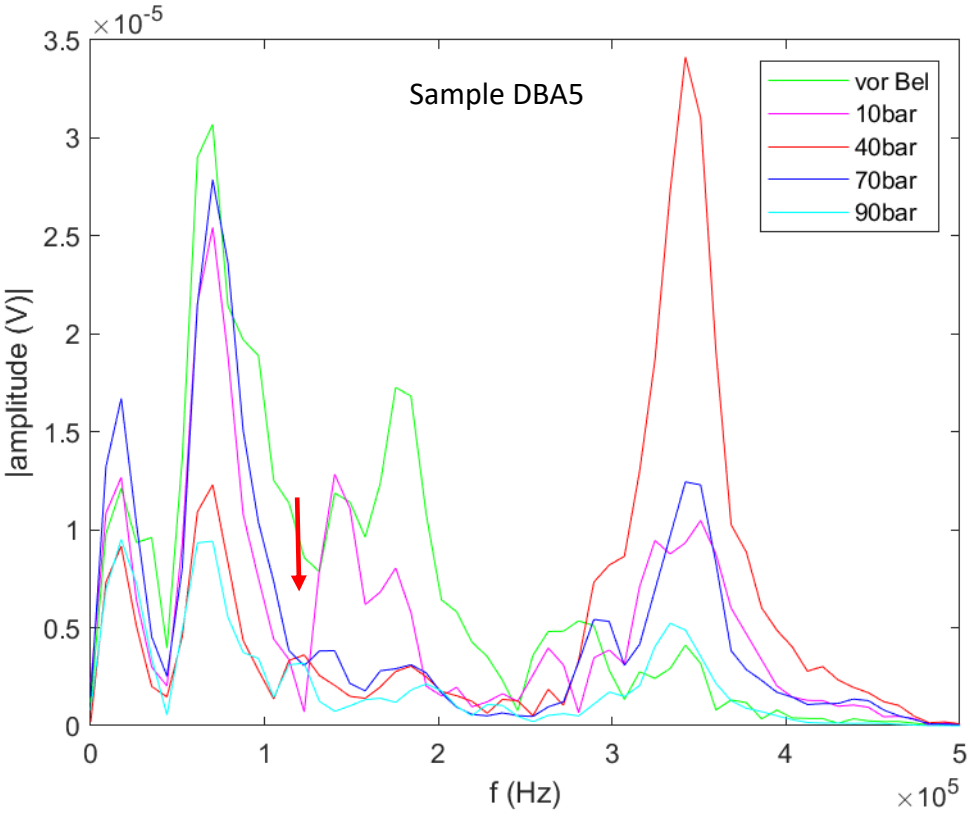

Figure 6-20: To display the diagram more clearly, only the data of before applying pore pressure, 10, 40, 70 and 90 bar are shown. Major shifts between before applying pore pressure and 10 bar can be observed. The other pressure levels don't show big changes. The red arrow highlights some shifting.

The data for the second Buntsandstein sample (DBA6), which is shown in Figure 6-21, has a very similar behaviour than the specimen DBA5. The clearest shifts are seen at 350 000 Hertz as well as at 120 000 Hertz. So, for the small frequency components there is nearly no shifting, while at about 120 000 Hertz the moving of the frequencies starts. The interpreted damage from every level to the next one correlates very well with the results of Figure 6-9.

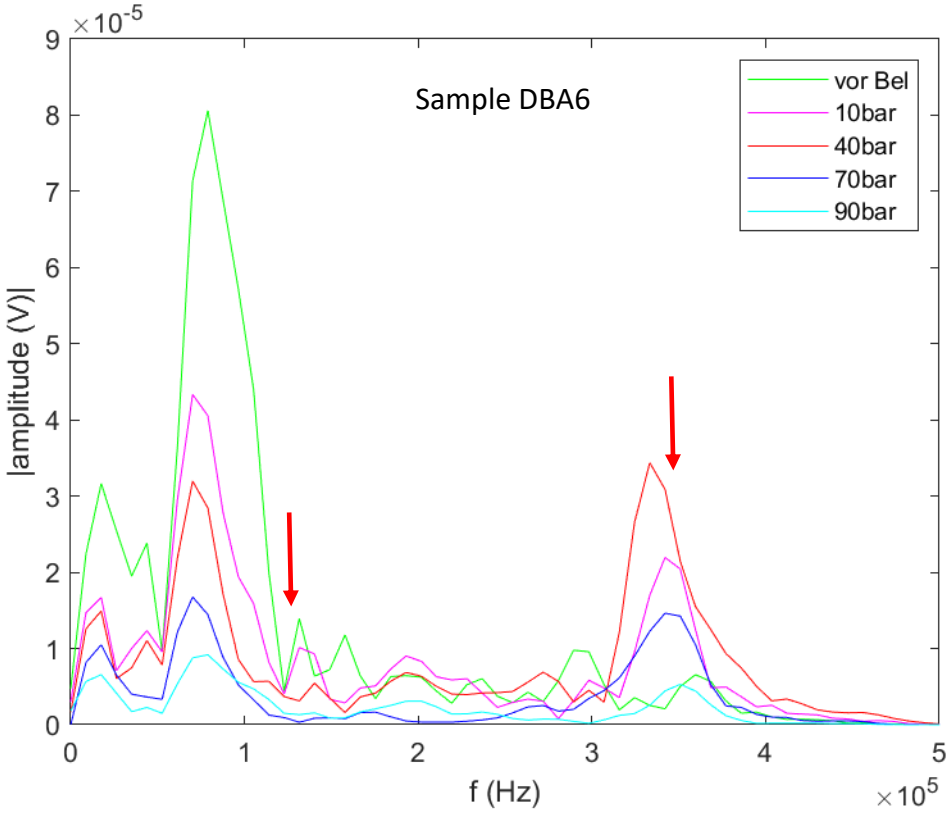

Figure 6-21: To get a better overview, only before applying pore pressure, 10, 40, 70 and 90 bar are shown. At about 350 000 Hertz, clear changes between the different pressure levels are visible. The red arrows highlight some shifting.

In Figure 6-22 the Fourier spectra of sample 4.1 are shown. As an exception, the 60 bar curve is pictured here instead of the 70 bar curve. The reason for this is an evaluation problem with the 70 bar data of this sample. In the small frequency range, it is not easy to detect clear shifts. At about 30 000 Hertz small differences between 40, 60 and 90 bar can be observed. The frequency component at about 200 000 Hertz also shows some small shifts at the same pressure levels. Thus, it can be confirmed that damage was induced, and that it also correlates very well with the results of the travel time curve (Figure 6-11).

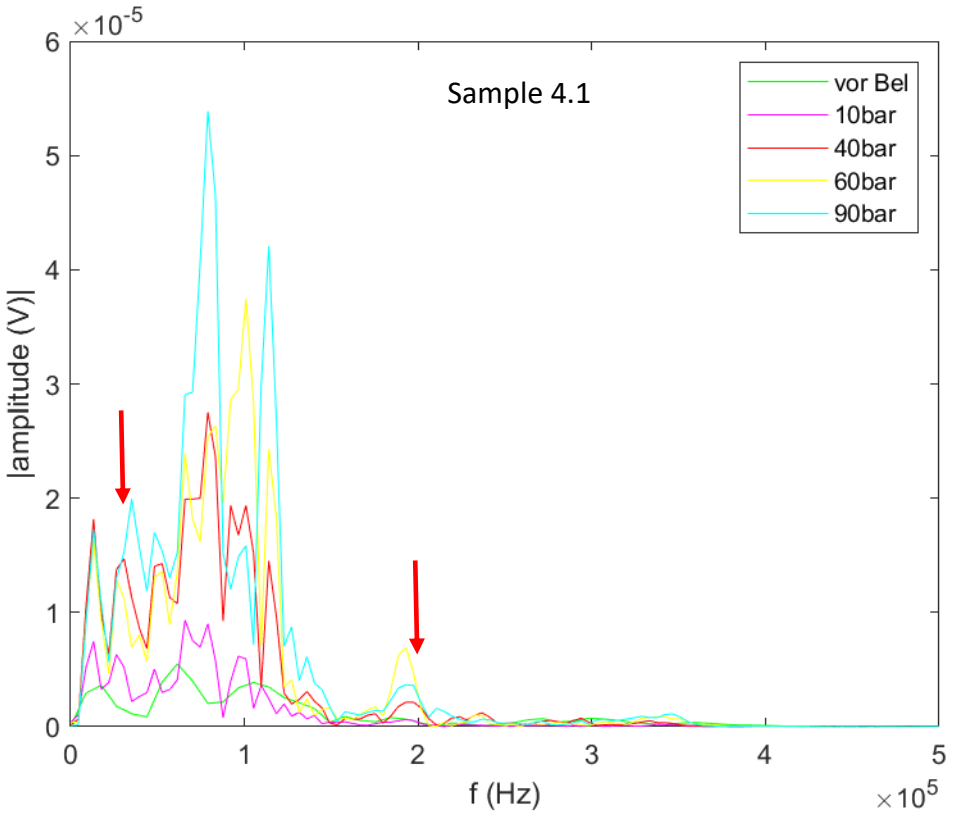

Figure 6-22: Only selected data are shown for a better overview. In the smaller frequency range, some small shifts can be detected comparing the curves before applying pore pressure (green) and at 10 bar with the ones at higher pressure levels. The red arrows highlight some shifting.

Figure 6-23 pictures the Fourier spectra of sample 4.2. At about 200 000 Hertz the most obvious shifting in this diagram is visible. A recognizable movement at about 80 000 Hertz from 40 to 70 and 70 to 90 can be seen. The rest of the diagram only shows very small to no shifts. In general, the two Exxon specimens behave very similar and also sample 4.2 correlates well with the observed results of the travel time data.

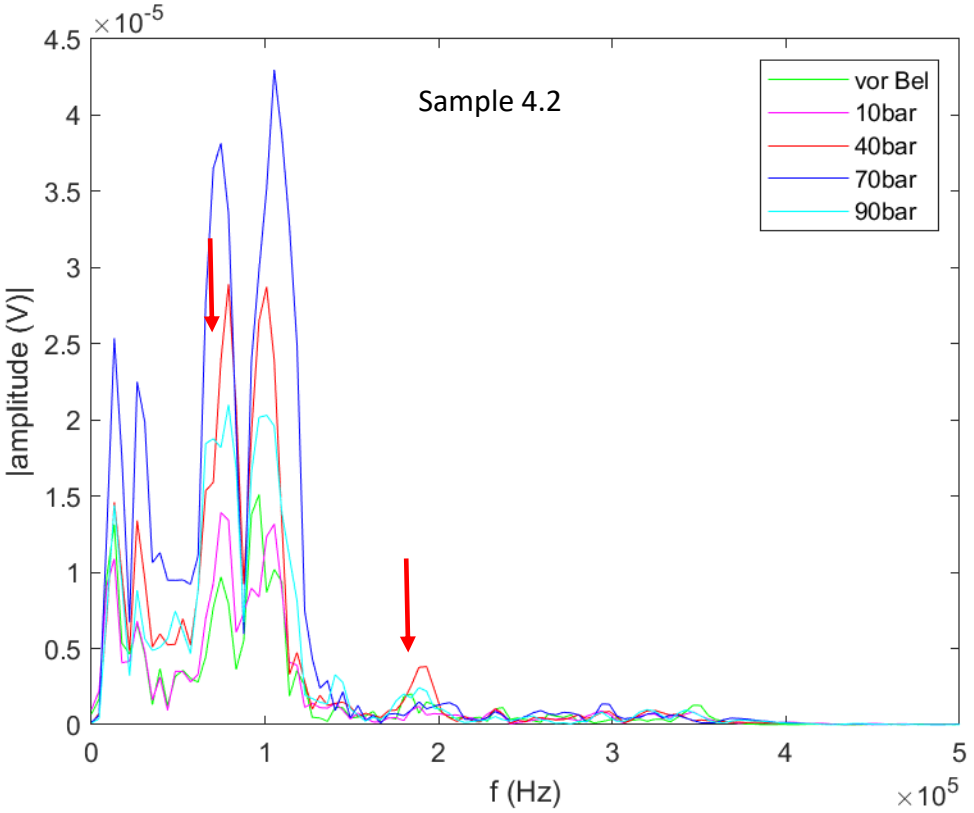

Figure 6-23: For a better overview, only before applying, 10, 40, 70 and 90 bar are pictured. Some small shifts are visible at about 200 000 Hertz. The red arrows highlight some shifting.

The trends of the calculated p-wave velocities are shown in Table 6-2. Table 6-1 gives the necessary information to the symbols used. To calculate the change in velocity, the value of the higher pressure stage is always divided by the value of the pressure stage before, and the result is subtracted from 1. For calculating the data of 60 and 80 bar on sample 4.1, the velocity two pressure levels before was used in each case.

Table 6-1:Legend for the percentage is always relative to the value of the pressure stage before.

Symbol	[%]
↑	>1.5
↗	0.2 bis 1.5
→	0.2 bis -0.2
↘	-0.2 bis -1.5
↓	<-1.5

$$velocity\ change_{0\ bar\ to\ 10\ bar} = 1 - \frac{v_{P10bar}}{v_{P0bar}}$$

Where,

V_{P10bar} = p-wave velocity at 10 bar [m/s]

V_{P0bar} = p-wave velocity at 0 bar [m/s]

A rough look at Table 6-2 reveals that in the range of 60 to 90 bar most significant velocity changes occur. The changes at 10 bar are mostly because of the impact of the Hoek cell. At 30 and 80 bar, the p-wave velocities decrease in almost all samples. In general, it can be assumed that the comparatively greatest mechanical damage occurs with the dark red arrows pointing downwards. The change in the green (light and dark green) coloured arrows is generally more indicative of grain rearrangement.

Table 6-2: Trend table of the p-wave velocity in each case relative to the previous pressure stage. The dark blue fields could not be evaluated.

Sample	1R	2R	DBA1	DBA2	DBA5	DBA6	4.1	4.2
10 bar	↓	↓	↗	↗	↘	↓	↓	↘
20 bar	↓	↓	→	↘	↗	→	↗	↘
30 bar	↓	↓	↘	↗	↓	↘	↘	↘
40 bar	↓	↓	→	↘	↗	→	↗	↘
50 bar	↑	↑	→	↘	↓	↘		↘
60 bar	↓	↑	↓	→	↑	↗	→	↗
70 bar	↗	↑	↘	↓	→	↓		→
80 bar	↓	↘	→	↘	↘	↘	↓	↓
90 bar	↑	→	↓	↘	↓	↘	↗	↗

Depending on the rock specimen, the damage is more or less severe. It is good to observe that samples of the same type behave very similarly with respect to the change of velocities. Looking at the trend of the Trattnach samples (1R and 2R), it is reasonable to assume that most of the damage to the samples is due to the influence of the Hoek cell. The arrows indicate high damage, so an increase in porosity is not surprising. The Imberg specimens (DBA1 and DBA2) show little change in velocity up to 60 respectively 70 bar, which is due to the fact that gas flow through the sample only occurred starting at 70 bar. Compared to the Trattnach samples, the arrows show significantly less difference in velocity, indicating less damage to the sample. The small porosity reduction confirms this. The Buntsandstein samples (DBA5 and DBA6) show the same tendency to change velocity at nearly all pressure levels. Interestingly, the pressure levels that probably cause the most damage are not the same. It can be seen that in comparison to the Imberg specimens, more larger velocity decreases occur, which explains a slightly higher porosity decrease. The Ruhr sandstone samples differ slightly at the low pressure levels. This may be related to the stronger influence of the Hoek cell on specimen 4.1 than on 4.2. At 80 bar, mechanical damage clearly occurs in both samples. As with the Imberg specimens, a small decrease in porosity can be explained by the few significant reductions in velocity. The dark blue fields are those with an evaluation problem in the signals.

The combination of ultrasonic measurements and the porosity determination delivers good data, which correlates very well. As expected, the samples are damaged, but mostly not to be visible macroscopically, except for the Trattnach samples. This obvious damage leads to a rise in porosity for the specimens 1R and 2R, while all the other ones show a decreasing trend. The cause of the reduction in porosity for all other specimens is most likely due to compaction by confinement and axial loading. A decrease in porosity was expected, since there is definitely a rearrangement of the grains when the pore pressure increases, which might be the reason why some pore throats are closed or reduced. These rearrangements lead to a change in travel times of the ultrasonic waves. The cause of random reduction in travel time is these rearrangements, which presumably create better paths for the signal, causing it to propagate through the sample faster. The increase in travel time despite decreasing porosity is likely caused by to micro fracturing due to axial loading and pore pressure damage, which contradicts the typical expectation of travel time decreasing with increasing porosity.

7 Conclusion & Recommendations

With the experimental setup developed here, it is possible to induce damage and also detect it by means of ultrasonic measurements. The most meaningful information here is the change in p-wave velocities and also the porosity measurements before and after the experiments. With the exception of the Trattnach samples, the porosities show a slight decrease. The increase of the Trattnach specimens can be seen macroscopically. The p-wave velocities decrease in all samples, which is due to micro fracturing. Also, velocity increase could be observed, and it was possible to detect the pore pressure levels with the most impact. With a few exceptions, the greatest damage is induced in the range from 30 to 40 bar and from 70 to 90 bar. A quantification of the damage was not possible.

With this information, a definite statement that the rock samples are damaged by different pore pressures under certain environmental conditions is possible.

To support and supplement these observations, Fourier analysis was performed. This confirms the damage to the specimen through shifts of individual frequency components in the frequency spectra of the different pressure levels. A statement about the intensity of the damage can only be made very roughly, but also cannot be quantified. No more precise information could be obtained from the mean and median frequency of the Fourier analysis. A comparison with the p-wave velocity also led to no result.

In conclusion, the question, if damage can be induced to a sandstone sample via raising the pore pressure can be answered with yes. Also, the second question, whether this damage is measurable with ultrasonic measurements can be answered with yes.

For further use of this system, an ultrasonic measurement with 0 bar gas pressure, but with vertical and horizontal loading, should be carried out, as this means that the influence of the Hoek cell itself no longer has such a large effect. I would also suggest using a Hoek cell with less big stamps, so that the ultrasonic measurement can be done directly in the system. When using the same stamps, amplifying the ultrasonic signal could possibly solve the problem. This would be a great advantage, as the installation and removal of the specimen is a source of error and possible damage every time. This could also improve the accuracy of the amplitude data by reducing the sources of error. As a result, a change in amplitude in the Fourier spectra could provide further insight into the damage to the sample. In general, the interpretation of Fourier analysis is very complex and experience in its use is an advantage.

Additionally, the installation of a flow meter would be interesting. From this, a correlation between flow rate and p-wave velocity can possibly be established, which could be of importance for injection and extraction processes, for example. Another question could be whether permeability measurements can be used for damage detection.

Furthermore, it would be interesting to link strength testing of the rocks to the pore pressure at which the first signs of damage can be seen. From this correlation, it may be possible to predict damage or fractures.

Another interesting point might be the grain arrangement before and after the testing. It should be possible to see a significant difference in the samples using thin section microscopy. The main challenge here is to get thin sections from the loaded specimen without damaging it any more than it already is.

8 References

Aftab, A., Hassanpouryouzband, A., Xie, Q., Machuca, L.L. & Sarmadivaleh, M. 2022. Toward a Fundamental Understanding of Geological Hydrogen Storage. *Industrial & Engineering Chemistry Research*, **61**, 3233–3253, http://doi.org/10.1021/acs.iecr.1c04380.

Alvarado, V. & Manrique, E. 2010. Enhanced Oil Recovery: An Update Review. *Energies*, **3**, 1529–1575, http://doi.org/10.3390/en3091529.

Birch, F. 1960. The velocity of compressional waves in rocks to 10 kilobars: 1. *Journal of Geophysical Research*, **65**, 1083–1102, http://doi.org/10.1029/JZ065i004p01083.

Bjørlykke, K. & Jahren, J. 2010. Sandstones and Sandstone Reservoirs. *In:* Bjorlykke, K. (ed) *Petroleum Geoscience*. Springer Berlin Heidelberg, Berlin, Heidelberg, 113–140.

Blake, O.O., Faulkner, D.R. & Rietbrock, A. 2013. The Effect of Varying Damage History in Crystalline Rocks on the P- and S-Wave Velocity under Hydrostatic Confining Pressure. *Pure and Applied Geophysics*, **170**, 493–505, http://doi.org/10.1007/s00024-012-0550-0.

Borm, G., Engeser, B., Hoffers, B., Kutter, H.K. & Lempp, C. 1997. Borehole instabilities in the KTB main borehole. *Journal of Geophysical Research*, **102**, 18507–18517, http://doi.org/10.1029/96JB03669.

Cooley, J.W. & Tukey, J.W. 1965. An algorithm for the machine calculation of complex Fourier series. *Mathematics of Computation*, **19**, 297–301, http://doi.org/10.1090/S0025-5718-1965-0178586-1.

Dewhurst, D.N. & Siggins, A.F. 2006. Impact of fabric, microcracks and stress field on shale anisotropy. *Geophysical Journal International*, **165**, 135–148, http://doi.org/10.1111/j.1365-246X.2006.02834.x.

Dillmann, O.O. 2008. Vorkommen und Gewinnung von Naturwerksteinen am Nordrand des Sauerlandes. *Jber. Mitt. oberrhein. Geol. Ver. N.F., 90*, 255–265.

Evans, D.J. 2007. An appraisal of Underground Gas Storage technologies and incidents, for the development of risk assessment methodology. Volume 1, Text. Volume 2, Figures and Tables.

Gebhardt, U. 1994. Origin of Rotliegend halites in the North German Basin, Upper Rotliegend II, Permian[Zur Genese der Rotliegend-Salinare in der Norddeutschen Senke (Oberrotliegend II, Perm)]. *Freiberger Forschungshefte, Reihe C*, 3–22.

Godec, M., Kuuskraa, V., van Leeuwen, T., Stephen Melzer, L. & Wildgust, N. 2011. CO2 storage in depleted oil fields: The worldwide potential for carbon dioxide enhanced oil recovery. *Energy Procedia*, **4**, 2162–2169, http://doi.org/10.1016/j.egypro.2011.02.102.

Gretener, P.E. 1969. Fluid pressure in porous media—its importance in geology: a review. *Bulletin of Canadian Petroleum Geology*, **17**, 255–295.

Gross, D., Sachsenhofer, R., Rech, A., Sageder, S., Geissler, M., Schnitzer, S. & Troiss, W. 2015. The Trattnach Oil Field in the North Alpine Foreland Basin (Austria). *Austrian Journal of Earth Sciences*, **108**, 151–171, http://doi.org/10.17738/ajes.2015.0018.

Guo, B. 2019. Petroleum reservoir properties. *In: Well Productivity Handbook*. Elsevier, 17–51.

Heap, M.J., Kushnir, A.R.L., Gilg, H.A., Wadsworth, F.B., Reuschlé, T. & Baud, P. 2017. Microstructural and petrophysical properties of the Permo-Triassic sandstones (Buntsandstein) from the Soultz-sous-Forêts geothermal site (France). *Geothermal Energy*, **5,** http://doi.org/10.1186/s40517-017-0085-9.

Heap, M.J., Villeneuve, M., Kushnir, A.R., Farquharson, J.I., Baud, P. & Reuschlé, T. 2019. Rock mass strength and elastic modulus of the Buntsandstein: An important lithostratigraphic unit for geothermal exploitation in the Upper Rhine Graben. *Geothermics*, **77**, 236–256, http://doi.org/10.1016/j.geothermics.2018.10.003.

Heunisch, C., Caspers, G., Elbracht, J., Langer, A., Röhling, H.-G., Schwarz, C. & Streif, H. 2017. Erdgeschichte von Niedersachsen. Geologie und Landschaftsentwicklung. *1864-7529*, **6**, 3–84.

Hill, S. 2019. *Mechanical rock property characterisation and assessment of sandstone reservoirs in the Southern Taranaki Basin*.

Hoffman, F. 1997. An introduction to Fourier theory. *Extraído el*, **2**.

Kern, H. 1990. Laboratory seismic measurements: an aid in the interpretation of seismic field data. *Terra Nova*, **2**, 617–628, http://doi.org/10.1111/j.1365-3121.1990.tb00127.x.

Kern, H. & Richter, A. 1979. Compressional and shear wave velocities at high temperature and confining pressure in basalts from the Faeroe Islands. *Tectonophysics*, **54**, 231–252, http://doi.org/10.1016/0040-1951(79)90370-6.

Keshavarz, A., Abid, H., Ali, M. & Iglauer, S. 2022. Hydrogen diffusion in coal: Implications for hydrogen geo-storage. *Journal of colloid and interface science*, **608**, 1457–1462, http://doi.org/10.1016/j.jcis.2021.10.050.

Kilburn, C.R.J. & Voight, B. 1998. Slow rock fracture as eruption precursor at Soufriere Hills Volcano, Montserrat. *Geophysical Research Letters*, **25**, 3665–3668, http://doi.org/10.1029/98GL01609.

Kim, S. & Hosseini, S.A. 2017. Study on the ratio of pore-pressure/stress changes during fluid injection and its implications for CO2 geologic storage. *Journal of Petroleum Science and Engineering*, **149**, 138–150, http://doi.org/10.1016/j.petrol.2016.10.037.

Lebedev, M., Pervukhina, M., Mikhaltsevitch, V., Dance, T., Bilenko, O. & Gurevich, B. 2013. An experimental study of acoustic responses on the injection of supercritical CO2 into sandstones from the Otway Basin. *GEOPHYSICS*, **78**, D293-D306, http://doi.org/10.1190/geo2012-0528.1.

Legarth, B., Huenges, E. & Zimmermann, G. 2005. Hydraulic fracturing in a sedimentary geothermal reservoir: Results and implications. *International Journal of Rock Mechanics and Mining Sciences*, **42**, 1028–1041, http://doi.org/10.1016/j.ijrmms.2005.05.014.

Lighthill, M.J. 1958. *An introduction to Fourier analysis and generalised functions*. Cambridge University Press.

Lo, T., Coyner, K.B. & Toksöz, M.N. 1986. Experimental determination of elastic anisotropy of Berea sandstone, Chicopee shale, and Chelmsford granite. *GEOPHYSICS*, **51**, 164–171, http://doi.org/10.1190/1.1442029.

Lockner, D.A., Walsh, J.B. & Byerlee, J.D. 1977. Changes in seismic velocity and attenuation during deformation of granite. *Journal of Geophysical Research*, **82**, 5374–5378, http://doi.org/10.1029/JB082i033p05374.

Luboń, K. & Tarkowski, R. 2020. Numerical simulation of hydrogen injection and withdrawal to and from a deep aquifer in NW Poland. *International Journal of Hydrogen Energy*, **45**, 2068–2083, http://doi.org/10.1016/j.ijhydene.2019.11.055.

Mcbride, E.F. 1963. A Classification of Common Sandstones. *SEPM Journal of Sedimentary Research*, **Vol. 33,** http://doi.org/10.1306/74D70EE8-2B21-11D7-8648000102C1865D.

Melhem, H. & Kim, H. 2003. Damage Detection in Concrete by Fourier and Wavelet Analyses. *Journal of Engineering Mechanics*, **129**, 571–577, http://doi.org/10.1061/(ASCE)0733-9399(2003)129:5(571).

Muhammed, N.S., Haq, M.B., Al Shehri, D.A., Al-Ahmed, A., Rahman, M.M., Zaman, E. & Iglauer, S. 2023. Hydrogen storage in depleted gas reservoirs: A comprehensive review. *Fuel*, **337**, 127032, http://doi.org/10.1016/j.fuel.2022.127032.

O'Dowd, N.P. 2002. Fracture Mechanics: Nonlinear. *In: Encyclopedia of Materials: Science and Technology*. Elsevier, 1–7.

Pettijohn, F.J., Potter, P.E. & Siever, R. 1973. *Sand and Sandstone*. Springer US, New York, NY.

Podio-Lucioni, A. 1968. *Experimental determination of the dynamic elastic properties of anisotropic rocks, ultrasonic pulse method*. The University of Texas at Austin.

R. H. Dott, JR. 1964. Wacke, Graywacke and Matrix--What Approach to Immature Sandstone Classification? *SEPM Journal of Sedimentary Research*, **Vol. 34,** http://doi.org/10.1306/74D71109-2B21-11D7-8648000102C1865D.

Reitenbach, V., Ganzer, L., Albrecht, D. & Hagemann, B. 2015. Influence of added hydrogen on underground gas storage: a review of key issues. *Environmental Earth Sciences*, **73**, 6927–6937, http://doi.org/10.1007/s12665-015-4176-2.

Schmid, K. 2018. *A geomechanical property model of the trattnach oil field in the upper austrian molasse basin,* Montanuniversität Leoben.

Simper, M.A. 1991. *Die Naturwerksteine Nordrhein-Westfalens und Verwitterungserscheinungen historischer Bausteine am Beispiel dortiger Grabdenkmäler*. Institut für Allgemeine und Angewandte Geologie der Ludwig-Maximilians-Universität.

Singh, G., Dhiman, R., Singh, M. & Singh, J. 2017. Detection of crack initiation in the ball bearing using FFT analysis. *International Journal of Mechanical Engineering and Technology*, **8**, 1376–1382.

Speight, J.G. 2019. Recovery, storage, and transportation. *In: Natural Gas*. Elsevier, 149–186.

Tsang, C.-F., Birkholzer, J. & Rutqvist, J. 2008. A comparative review of hydrologic issues involved in geologic storage of CO2 and injection disposal of liquid waste. *Environmental Geology*, **54**, 1723–1737, http://doi.org/10.1007/s00254-007-0949-6.

Ugarte, E.R. & Salehi, S. 2022. A Review on Well Integrity Issues for Underground Hydrogen Storage. *Journal of Energy Resources Technology*, **144,** http://doi.org/10.1115/1.4052626.

Ulusay. 2015. *The ISRM suggested methods for rock characterization, testing and monitoring: 2007-2014*. Springer, Cham.

Wong, R.C.K., Schmitt, D.R., Collis, D. & Gautam, R. 2008. Inherent transversely isotropic elastic parameters of over-consolidated shale measured by ultrasonic waves and their

comparison with static and acoustic in situ log measurements. *Journal of Geophysics and Engineering*, **5**, 103–117, http://doi.org/10.1088/1742-2132/5/1/011.

Yurikov, A., Nourifard, N., Pervukhina, M. & Lebedev, M. 2019. Laboratory ultrasonic measurements: Shear transducers for compressional waves. *The Leading Edge*, **38**, 392–399, http://doi.org/10.1190/tle38050392.1.

Zivar, D., Kumar, S. & Foroozesh, J. 2021. Underground hydrogen storage: A comprehensive review. *International Journal of Hydrogen Energy*, **46**, 23436–23462, http://doi.org/10.1016/j.ijhydene.2020.08.138.

9 List of Figures

10 List of Tables

11 Appendices

Table 11-1: Dimensions of the individual samples.

Sample	1R	2R	DBA1	DBA2	DBA5	DBA6	4.1	4.2
Length [mm]	85.64	91.85	100.83	101.32	99.74	99.2	97.06	96.85
Length [mm]	85.63	91.94	100.76	101.29	99.74	99.19	97.09	96.85
Length [mm]	85.66	91.77	100.8	101.3	99.63	99.22	96.97	96.83
average Length [mm]	85.643	91.853	100.797	101.303	99.703	99.203	97.040	96.843
Diameter [mm]	45.12	45.28	49.85	49.89	50	49.28	45.41	45.4
Diameter [mm]	45.1	45.37	49.88	49.79	50.09	49.39	45.42	45.43
Diameter [mm]	45.13	45.31	49.85	49.87	50.14	49.35	45.39	45.48
average Diameter [mm]	45.117	45.320	49.860	49.850	50.077	49.340	45.407	45.437
V_{bulk} [cm³]	136.92	148.17	196.81	197.72	196.37	189.68	157.14	157.03

Table 11-2: P-wave velocities of every individual sample at the different pore pressures and before and after the cyclical pore pressure loading. For sample 4.1, the values of the 50 and 70 bar measurement could not be calculated due to MatLab problems.

Sample	1R	2R	DBA1	DBA2	DBA5	DBA6	4.1	4.2
0 bar [m/s]	1445.7	1435.2	3974.6	4081.5	2834.1	2852.3	4104.9	3849.1
10 bar [m/s]	1356.8	1409.7	4009.4	4094.7	2811.7	2766.4	3931.9	3812.7
20 bar [m/s]	1331.5	1362	4009.4	4071.7	2838.1	2767.9	3951.1	3794.8
30 bar [m/s]	1301.6	1334.3	3984	4084.8	2777.2	2728.4	3938.3	3759.4
40 bar [m/s]	1242.6	1274.3	3977.7	4071.7	2789.7	2726.9	3951.1	3713.3
50 bar [m/s]	1293.7	1328.1	3971.5	4045.6	2703.4	2695.7		3701.9
60 bar [m/s]	1268.4	1350	3844.2	4039.2	2749.7	2701.6	3944.7	3724.7
70 bar [m/s]	1277.5	1372.6	3789.3	3969.6	2749.7	2641.2		3730.5
80 bar [m/s]	1240.5	1360.4	3795	3960.2	2742.1	2635.6	3875.4	3668.3
90 bar [m/s]	1276	1359.6	3727.7	3951	2700.5	2621.6	3894.1	3690.7
before cycl. loading [m/s]	1248.4	1316.7	3744.3	3938.7	2733.1	2588.8	3894.1	3690.7
after cycl. loading [m/s]	1277.5	1318.2	3761	3944.8	2651.7	2583.4	3900.3	3673.9

Table 11-3: Median frequencies of every individual sample at the different pore pressures and before and after the cyclical pore pressure loading. For sample 4.1, the values of the 50 and 70 bar measurement could not be calculated due to MatLab problems.

Median frequency [Hz]								
Sample	1R	2R	4.1	4.2	DBA1	DBA2	DBA5	DBA6
0 bar	66454.00	54631.86	47268.54	61889.96	63073.47	137568.18	56557.20	55624.02
10 bar	55278.55	73830.01	47856.94	54635.16	129490.97	163789.84	54164.95	54927.43
20 bar	66314.93	52533.53	53382.05	64965.85	54709.84	183962.08	228406.08	50247.34
30 bar	54325.63	52651.83	52543.82	56784.64	154448.70	224715.72	48529.36	230963.23
40 bar	53589.54	52844.92	52781.65	58143.50	135415.26	220086.82	236493.23	219304.93
50 bar	55712.31	51284.86	-	57261.58	167597.98	223841.52	48787.51	230887.95
60 bar	55039.57	51842.52	64004.11	59662.23	165418.35	233908.78	49823.60	223846.20
70 bar	51312.58	50880.53	-	59591.00	192716.84	236074.69	51597.18	63590.57
80 bar	35065.76	49869.21	64300.64	55636.84	168233.42	228871.41	45448.96	54512.96
90 bar	48801.08	26164.49	55501.97	57016.40	144584.95	224698.58	44582.27	56390.94
before cycl. Loading	45920.08	25690.72	55501.97	57016.40	68712.63	197100.29	58139.15	59017.71
after cycl. Loading	69083.28	44744.15	55949.26	58766.64	18669.87	47920.07	53980.27	53014.54

Table 11-4: Mean frequencies of every individual sample at the different pore pressures and before and after the cyclical pore pressure loading. For sample 4.1, the values of the 50 and 70 bar measurement could not be calculated due to MatLab problems.

Mean frequency [Hz]								
Sample	1R	2R	4.1	4.2	DBA1	DBA2	DBA5	DBA6
0 bar	66952.59	55823.15	55010.99	51281.16	99795.00	151548.35	71976.27	57083.13
10 bar	58901.08	65361.77	43476.12	52714.39	140472.04	146823.25	91529.62	88165.33
20 bar	83502.52	51922.99	48578.87	60928.49	100564.31	165025.35	209679.46	74098.24
30 bar	59580.75	53730.14	49502.70	57511.28	155566.07	171542.31	52814.87	188119.80
40 bar	59776.63	52267.73	49423.06	56908.83	146503.99	169090.06	213198.93	149952.49
50 bar	59240.16	46519.42	-	56378.18	159512.38	182153.78	46701.84	177661.63
60 bar	62594.28	47572.42	59728.37	56480.09	146224.06	207468.55	73891.07	164407.77
70 bar	50815.71	46059.42	-	57351.43	165701.33	204164.57	80167.30	133362.42
80 bar	38605.74	43174.23	58972.47	55379.09	161025.85	210544.99	79204.60	78273.07
90 bar	51844.68	30967.50	56453.77	56090.47	151646.08	177306.71	70907.37	84904.41
before cycl. Loading	58006.00	31812.48	56453.77	56090.47	81589.06	154837.04	61579.03	62259.35
after cycl. Loading	61304.13	47069.58	57317.73	59920.98	43960.20	83606.75	52151.93	55876.72